

Scientific Publications (Total impact factor: ~ 153)

1. **Sopan Nangare**, Pravin Patil. Platinum-alginate-chitosan nanobioconjugate decorated carbon backbone layered biosensor for highly sensitive and selective detection of BACE-1 International Journal of Biological Macromolecules, 250 (2023); 126224. (**Impact Factor: 8.2; Status:** Published, UGC Approved).
2. **Sopan Nangare**, Pravin Patil. Poly(allylamine) coated layer-by-layer assembly decorated 2D carbon backbone for highly sensitive and selective detection of Tau-441 using surface plasmon resonance biosensor. Analytica Chimica Acta, 1271(2023)341474. (**Impact Factor: 6.2; Status:** Published, UGC Approved).
3. **Sopan Nangare**, Mahendra Mahajan, Pravin Patil. Nanosize design of carbon dots, graphene quantum dots, and metal–organic frameworks based sensors for detection of chlorpyrifos in food and water: A review. Microchemical Journal. 193(2023) 109056 (**Impact Factor: 4.8; Status:** Published, UGC Approved).
4. **Sopan Nangare**, Pravin Patil, et al. Nanostructured metal-organic frameworks based luminescent sensor for chemical sensing: Current Challenges and future prospects. Journal Nanostructure in Chemistry, 13(2023) 197-242. (**Impact Factor: 10.1; Status:** Published, UGC Approved).
5. **Sopan Nangare**, Pratiksha Devkar, L R Zawar, et al., Design of polyacrylamide grafted sesbania gum-mediated pH-responsive IPN-based microbeads for delivery of diclofenac sodium: In-vitro-in-vivo characterizations. International Journal of Biological Macromolecules, 230 (2023) 123360. (**Impact Factor: 8.2; Status:** Published, UGC Approved).
6. **Nangare, Sopan**, Patil, Sairendhri, Patil, Ashwini, Deshmukh, Prashant and Patil, Pravin O., Bovine serum albumin-derived poly-l-glutamic acid-functionalized graphene quantum dots embedded UiO-66-NH₂ MOFs as a fluorescence ‘On-Off-On’ magic gate for para-aminohippuric acid sensing. Journal of Photochemistry and Photobiology A: Chemistry, 438(2023) 114532 (**Impact Factor: 4.2; Status:** Published, UGC Approved).
7. **Sopan Nangare**, Dinesh Borhade, Ganesh B. Patil, et al., Preparation of pirfenidone loaded chitosan-polyvinyl alcohol-graphene oxide-based scaffold: Spectroscopical characterizations and antibacterial activity. Journal of Drug Delivery Science and Technology, 82(2023) 104325. (**Impact Factor: 5; Status:** Published, UGC Approved).
8. Jidnyasa Pantwalawalkar, **Sopan Nangare**, Namdeo Jadhav, et al., Stimuli responsive design of metal-organic frameworks for cancer theranostics: Current challenges and future perspective. ACS Biomaterials Science & Engineering, 9(2023) 4497-4526. (**Impact Factor: 5.8; Status:** Published, UGC Approved).
9. **Sopan Nangare**, Pravin Patil, et al., Graphene quantum dots incorporated UiO-66-NH₂ based fluorescent nanocomposite for highly sensitive detection of quercetin Nano Biomedicine and Engineering, 15 (2023) 1-13 (**Status:** Published, UGC Approved).
10. **Sopan Nangare**, Bhupesh Patil, Laxmikant Zawar. Preparation of crystallinity tailored silk fibroin-sodium alginate based floating microbeads for nevirapine delivery. Cellulose Chemistry and Technology, 57(2023) 527-539. (**Impact Factor: 1.3; Status:** Published, UGC Approved).
11. **Sopan Nangare**, Kirti Rajput, L R Zawar, et al., Formulation, optimization, and in-vitro-ex-vivo evaluation of dual-crosslinked zinc pectinate-neem gum-interpenetrating polymer network mediated lansoprazole loaded floating microbeads.

- International Journal of Biological Macromolecules, 222 (2022) 915-926. (**Impact Factor: 8.2; Status:** Published, UGC Approved).
12. Vipul Chaudhari, **Sopan Nangare**, Laxmikant Zawar, et al., Chitosan–sesbania gum mediated pH-responsive polyelectrolyte complexes for targeted delivery of diclofenac sodium: preparation and spectroscopical evaluation. Indian Journal of Pharmaceutical Education and Research, 57(2023) s564-s572. (**Impact Factor: 0.8; Status:** Published, UGC Approved).
 13. **Sopan Nangare**, Vivekanand Chatap, et al., Custard apple peels containing saponin: Isolation and formulation of herbal shampoo. Indian Drugs, 2023 (**Status:** Accepted, UGC Approved).
 14. **Sopan N. Nangare**, Pravin O. Patil. Black phosphorus nanostructure-based highly sensitive and selective surface plasmon resonance sensor for biological and chemical sensing: A review. Critical Reviews in Analytical Chemistry, 53(2023) 1-26. (**Impact Factor: 5; Status:** Published, UGC Approved)
 15. Monika L.Girasea,Vrashabh V.Sugandhi, **Sopan N. Nangare**. Design of surface tailored carboxymethyl dextran-protein based nanoconjugates for paclitaxel: Spectroscopical characterizations and cytotoxicity assay. International Journal of Biological Macromolecules. International Journal of Biological Macromolecules, 222 (2022) 1818-1829 (**Impact Factor: 8.2; Status:** Published, UGC Approved).
 16. **Sopan Nangare**, Pravin O. Patil. Chitosan mediated layer-by-layer assembly based graphene oxide decorated surface plasmon resonance biosensor for highly sensitive detection of β -amyloid. International Journal of Biological Macromolecules, 2022.214; 568-582. (**Impact Factor: 8.2; Status:** Published, UGC Approved).
 17. **Sopan Nangare**, Sagar Patil, Sairendhri Patil, Pravin Patil. Design of graphene quantum dots decorated MnO₂ nanosheet-based fluorescence turn “On-Off-On” nanoprobe for highly sensitive detection of lactoferrin. Inorganic Chemistry Communications. 2022;143:109751. (**Impact Factor: 3.8; Status:** Published, UGC Approved).
 18. Sandip M Honmane, Praffula B Choudhari, **Sopan N Nangare**, et al., Polydopamine surface-modified nanocarriers for improved anticancer activity: Current progress and future prospects. OpenNano, 7(2022) 100059. (**Status:** Published, UGC Approved).
 19. **Sopan Nangare**, Pravin O. Patil. Design of monoelemental based two dimensional nanoarchitectures for therapeutic, chemical sensing and in vitro diagnosis applications: A case of borophene. Journal of Molecular Structure, 1265(2022) 133387. (**Impact Factor: 3.8; Status:** Published, UGC Approved).
 20. Dhiarysheel Ghadge, **Sopan Nangare**, Namdeo Jadhav. Formulation, optimization, and in vitro evaluation of anastrozole-loaded nanostructured lipid carriers for improved anticancer activity. Journal of Drug Delivery Science and Technology, 72(2022)103354. (**Impact Factor: 5; Status:** Published, UGC Approved).
 21. **Sopan Nangare**, Pravin Patil, Ashwini Patil. Fabrication of nitrogen-doped graphene quantum dots as a fluorescent probe for highly sensitive detection of uric acid. Acta Chimica Slovenica., 69(2022) 437–447, (**Impact Factor: 1.44; Status:** Published, UGC Approved).
 22. Dilip Patil, **Sopan Nangare**, Gaurav Patil, Ganesh Patil, et al., Development of thiolated polyethylene glycol-poly (lactic-co-glycolic acid) co-polymeric nanoparticles for intranasal delivery of quetiapine: *In vitro- ex vivo* characterization. International Journal of Polymeric Material and Polymeric Biomaterial, 72 (2023) 714-724. (**Impact Factor: 3.2; Status:** Published, UGC Approved).
 23. Zamir Khan, **Sopan Nangare**, Pravin Patil, et al., Surface nanoarchitected metal-organic frameworks based sensor for reduced glutathione sensing: A review. Journal

- Nanostructure in Chemistry, 12(2022) 1053-1074. (**Impact Factor: 10.1; Status:** Published, UGC Approved).
24. Shailesh S. Dugam, **Sopan N. Nangare**, et al., Crystallinity modulated silk fibroin electrospun nanofibers based floating scaffold as a candidate for controlled release of felodipine. International Journal of Polymeric Materials and Polymeric Biomaterials, 71(2022)1393-1406. (**Impact Factor: 3.2; Status:** Published, UGC Approved).
 25. **Sopan Nangare**, Namdeo Jadhav, et al., Development of amino acid salt-based curcumin@lysine acetate co-amorphous system using liquid-assisted grinding for improved solubility and dissolution. Thai Journal of Pharmaceutical Sciences, 46(2023) 711-719. (**Status:** Published, UGC Approved).
 26. Sopan Nangare, Jidnyasa Pantwalawalkar, et al., Formulation of silk fibroin-based single polymeric floating microspheres for sustained release of lafutidine. Indian Journal of Pharmaceutical Education and Research, 56(2022) 396-404. (**Impact Factor: 0.8; Status:** Published, UGC Approved).
 27. Rault Tade, **Sopan Nangare**, Pravin Patil, et al., Graphene quantum dots (GQDs) nanoarchitectonics for theranostic application in lung cancer. Journal of Targeting, 30(2022) 269-286. (**Impact Factor: 4.5; Status:** Published, UGC Approved).
 28. Trupti A. Powar, **Sopan N. Nangare**, et al., Development and evaluation of lyophilized methotrexate nanosuspension using quality by design approach. Acta Chemica Solvonica, 68(2021) 861-881 (**Impact Factor: 1.5; Status:** Published, UGC Approved).
 29. **Sopan N. Nangare**, Namdeo R. Jadhav, et al., Silk industry waste protein: Isolation, purification and fabrication of electrospun silk protein nanofibers as a possible nanocarrier for floating drug delivery. IOP Nanotechnology, 32(2020) 035101 (**Impact Factor: 3.87; Status:** Published, UGC Approved).
 30. **Sopan N. Nangare**, Sayali R. Patil, Pravin O. Patil, et al., Structural design of metal-organic framework based sensors for ultrasensitive detection of organophosphorus pesticides in food and water samples: Current challenges and future prospects. Journal Nanostructure in Chemistry, 12(2021) 729-764. (**Impact Factor: 8.0; Status:** Published, UGC Approved).
 31. **Sopan N. Nangare**, Pravin O. Patil, et al., Surface architected metal-organic framework-based biosensor for ultrasensitive detection of uric acid: Recent advancement and future perspectives. Microchemical Journal, 169(2021) 106567. (**Impact Factor: 5.304; Status:** Published, UGC Approved).
 32. **Sopan N. Nangare**, Pravin O. Patil. Nanoarchitected bioconjugates and bioreceptors mediated surface plasmon resonance biosensor for in vitro diagnosis of Alzheimer's disease: Development and future prospects. Critical Reviews in Analytical Chemistry. 52(2023):1139-1169. (**Impact Factor: 5, Status:** Published, UGC Approved).
 33. **Sopan N. Nangare**, Pravin Patil. Affinity-based nanoarchitected biotransducer for sensitivity enhancement of surface plasmon resonance sensors for in vitro diagnosis: A review. ACS Biomaterial Science and Engineering7 (2021) 2-30. (**Impact Factor: 5.39; Status:** Published, UGC Approved).
 34. Rahul S. Tade, **Sopan N. Nangare**, Pravin O. Patil, et al., Recent advancement in bio-precursor derived graphene quantum dots: synthesis, characterization and toxicological perspective. IOP Nanotechnology, 31(2020): 292001. (**Impact Factor: 3.87; Status:** Published, UGC Approved).
 35. Pravin Patil, Gaurav R. Pandey, **Sopan N. Nangare**, et al., Graphene-based nanocomposites for sensitivity enhancement of surface Plasmon resonance sensor for

- biological and chemical sensing: A review. *Biosensors and Bioelectronics*, 135(2019) 111324. (**Impact Factor: 9.51**; **Status:** Published, UGC Approved)
36. **Sopan N. Nangare**, Pravin O. Patil, et al., Green synthesis of Fe-doped Ag-loaded reduced graphene oxide ternary nanocomposite for efficient photocatalytic degradation of toxic dyes. *Advances in Natural Sciences: Nanoscience and Nanotechnology*, 12(2021) 035004 (**Status:** Published, UGC Approved)
 37. Pravin O. Patil **Sopan N. Nangare**, et al., Fabrication of N-doped graphene@TiO₂ nanocomposites for its adsorption and absorbing performance with facile recycling. *Nano Biomedicine and Engineering*, 13(2021) 179-190. (**Status:** Published, UGC Approved)
 38. **Sopan N. Nangare**, Mayuri M. Shitole, et al., Development of novel freeze-dried mulberry leaves extract-based transfersomal gel. *Turkish Journal of Pharmaceutical Sciences*, 18(2021) 44-55. (**Status:** Published, UGC Approved)
 39. **Sopan N. Nangare**, Rahul D. Rathod, et al., Zero-order derivative and area under curve UV-spectrophotometric methods for determination of calcium levofolinate in bulk and pharmaceutical dosage form. *Asian Journal of Pharmaceutical Analysis*, 10(2020)129-133. (**Status:** Published)
 40. Rahul S. Tade, **Sopan N. Nangare**, Pravin O. Patil. Agro-industrial waste-mediated green synthesis of silver nanoparticles and evaluation of its antibacterial activity. *Nano Biomedicine and Engineering*, 12(2020) 57-66. (**Status:** Published, UGC Approved)
 41. Sopan Nangare, Jidnyasa Pantwalawalkar, et al., Graphene quantum dots based ultrasensitive probe for biosensing of prostate cancer biomarkers: Current updates and future challenges. *Advances in Natural Sciences: Nanoscience and Nanotechnology*, 13 (2022) 013001 (**Status:** Published, UGC Approved).
 42. **Sopan N. Nangare**, Pravin O. Patil. Prevalence, distribution, treatment, and modern methods for in vitro diagnosis of Alzheimer's disease in India: Challenges and future perspectives. *Thai Journal of Pharmaceutical Sciences*. 2022; 46(2):149-160. (**Status:** Published, UGC Approved).
 43. **Sopan N. Nangare**, Mayuri M. Shitole, Namdeo R. Jadhav. Review on drug delivery applications of ethosomes: Current developments and prospects. *Thai Journal of Pharmaceutical Sciences*. 45(2022) 251-265. (**Status:** Published, UGC Approved).
 44. Rahul S. Tade, **Sopan N. Nangare**, Pravin O. Patil. Historical dilemmas of corona virus disease (COVID-19): Public health emergency, management perspectives, and global impacts. *Asian Journal of Nursing Education and Research*, 9(2021): 345-356. (**Status:** Published)
 45. **Sopan N. Nangare**, Nikita Kumawat, et al., An overview on phytochemistry, pharmacology, pharmaceuticals, traditional and economical aspects of Agele marmelos. *Asian Journal of Pharmacy and Technology*, 11(2021) 166-174. (**Status:** Published)
 46. **Sopan N. Nangare**, Pravin O. Patil, et al., Pharmaceutical applications of citric acid. *Future Journal of Pharmaceutical Sciences*, 7(2021)1-23. (**Status:** Published, UGC Approved)
 47. Rahul Tade, **Sopan N. Nangare**, Pravin Patil. Fundamental aspects of graphene and its biosensing applications. *Functional Composites and Structures*, 3(2021) 012001. (**Status:** Published, UGC Approved)
 48. **Sopan N. Nangare**, Shailesh Dugam, et al., Emerging era of microneedle array for pharmaceutical and biomedical applications: recent advances and toxicological perspectives. *Future Journal of Pharmaceutical Sciences*, 7(2021):1-26. (**Status:** Published, UGC Approved)

49. **Sopan N. Nangare**, Namdeo R. Jadhav, et al., Carbon dots: A novel trend in pharmaceutical applications. *Annales Pharmaceutiques Françaises*, 79(2021) 335-345. (**Status:** Published, UGC Approved)
50. **Sopan Nangare**, Shailesh Dugam. Smart invasome synthesis, characterizations, pharmaceutical applications, and pharmacokinetic perspective: A review. *Future Journal of Pharmaceutical Sciences*, 6(2020) 123. (**Status:** Published, UGC Approved)
51. Rahul S. Tade **Sopan N. Nangare**, Pravin O. Patil. Graphene conquering pharmaceutical horizons. *Inventi Rapid: Pharm Tech*, 2020 (2) 1-5. (**Status:** Published)
52. **Sopan N. Nangare**, Pravin O. Patil. Green synthesis of silver nanoparticles: An eco-friendly approach. *Nano Biomedicine and Engineering*, 12(2020) 281-296. (**Status:** Published, UGC Approved)
53. **Sopan N. Nangare**, Mayuri M. Shitole, et al., Pharmaceutical applications of silk sericin. *Annales Pharmaceutiques Françaises*, 78(2020) 469-486. (**Status:** Published, UGC Approved)
54. **Sopan N. Nangare**, Mayuri M. Shitole, et al., Progress in erectile dysfunction therapy through drug delivery system. *Thai Journal of Pharmaceutical Sciences*, 44(2020) 73-81. (**Status:** Published, UGC Approved)
55. **Sopan N. Nangare**, Mayuri M. Shitole, et al., Pharmaceutical applications of electrospun nanofibers: A state-of-the-art review. *Asian Journal of Pharmacy and Technology*, 10(2020) 187-201. (**Status:** Published)
56. **Sopan N. Nangare**, Namdeo R. Jadhav, Pravin Ghagare, et al., pharmaceutical applications of electrospinning. *Annales Pharmaceutiques Françaises*. 78(2020) 1-11. (**Status:** Published, UGC Approved)
57. Gaurav Patil, **Sopan Nangare**, Ganesh Patil., Survey on analysis of knowledge, attitude, and belief regarding COVID-19 vaccination in the selected region of North Maharashtra: A cross-sectional study. *Indian Journal of Respiratory Care*, 11(2022)363-368. (**Status:** Published, UGC Approved).

Book Chapters

1. **Sopan Nangare**, Pravin Patil, Pharmacokinetics of drug-in-polymer matrix-based nanoparticulate drug delivery system. 2022; 159-186. **Publisher:** Springer (Published).
2. **Sopan N. Nangare**, Pravin O. Patil, *et al.* Architected Polymeric Nanoplatfroms Targeted Treatment of prostate cancer. 2022, 427-471. **Publisher:** Springer (Published).
3. Mahesh More, **Sopan N. Nangare**, Pravin O. Patil, *et al.* Passive and active targeting approaches for solid tumors: Progress till date and associated challenges. 2022, 127-166. **Publisher:** Springer (Published)
4. Rahul Tade, **Sopan N. Nangare**, Pravin O. Patil, *et al.* Polymer-based nanoplatfrom for breast cancer targeting. 2022,373-400. **Publisher:** Springer(Published).
5. **Sopan Nangare**, Pravin Patil, Sanjaykumar Bari, et al., Advanced hydrogel-based platform for ocular drug delivery. 2023, 305-320 **Publisher:** Elsevier (Published).
6. Mahesh More, **Sopan Nangare**, Pravin Patil, Prashant Deshmukh. Nanostructures used in cancer imaging. 2023, 169-191 (**Publisher:** Elsevier (Published).
7. **Sopan Nangare**, Meghanath Shete, Madhav Shelke, Matin Shaikh, Kiran Patil. Immunomodulation property of antioxidants. **Publisher:** Apple Academic Press (**Status:** In production).

8. **Sopan Nangare**, Mahendra Mahajan, Pravin Patil. Surface plasmon-based diagnostic technology. **Publisher:** Wiley-Scrivener publishers (**Status:** Accepted for publication, **Publisher:** Wiley-Scrivener)
9. **Sopan Nangare**, Pravin Patil, et al., Nano-therapeutics for a diabetic foot ulcer and wound healing with metal nanocomposites. (**Status:** Accepted for publication, **Publisher:** CRC Press & Taylor and Francis.)
10. **Sopan Nangare**, Pravin Patil, Namdeo Jadhav, et al., Electro spun nanofibers based on silk sericin. (**Status:** Submitted, **Publisher:** Elsevier)
11. Ganesh Patil, **Sopan Nangare**, et al., Predicting biodegradation. (**Status:** Submitted, **Publisher:** CRC Press, Taylor and Francis)

Patent Published

- ✦ **Patent application no:** 202121003034 (**Status:** Published)
Applicant: Sopan N. Nangare, Pravin O. Patil, Rahul Tade, Sanjay B. Bari
- ✦ **Patent application no:** 202121003033(**Status:** Published)
Applicant: Rahul S. Tade, Sopan N. Nangare, Pravin O. Patil, Sanjay B. Bari
- ✦ **Patent application no:** 202321040442 (**Status:** Submitted)
Applicant: Zamir Khan, Sopan N. Nangare, Pravin O. Patil, et al.,
- ✦ **Patent application no:** 202321040441 (**Status:** Submitted)
Applicant: Zamir Khan, Sopan N. Nangare, Pravin O. Patil, et al.,

Date: 19/8/2023

Place: Shirpur



Sopan Namdev Nangare



Chitosan mediated layer-by-layer assembly based graphene oxide decorated surface plasmon resonance biosensor for highly sensitive detection of β -amyloid

Sopan Nangare, Pravin Patil *

Department of Pharmaceutical Chemistry, H. R. Patel Institute of Pharmaceutical Education and Research, Shirpur-425405, Dist: Dhule, MS, India

ARTICLE INFO

Keywords:

Alzheimer's disease
Beta-amyloid
Chitosan
Layer-by-layer assembly
Surface plasmon resonance
Graphene oxide, silver nanoparticles

ABSTRACT

Alzheimer's disease (AD), and its consequent effect primarily clinical dementia, Parkinson's disease dementia, etc. currently bring potential avenues for diagnosis centered on identification of beta-amyloid₁₋₄₂ ($A\beta_{1-42}$). Unfortunately, techniques engaged in AD core biomarker ($A\beta_{1-42}$) detection are majorly suffering from poor sensitivity and selectivity. Thus, we fabricated graphene oxide (GO) surface decorated chitosan (CS) mediated layer-by-layer (LbL) assembly based surface plasmon resonance (SPR) biosensor for highly sensitive and selective recognition of $A\beta_{1-42}$. Briefly, silver nanoparticles (AgNPs) and GO synthesis were achieved through a greener approach. LbL assembly was designed using CS and polystyrene sulphonate (PSS) on surface of AgNPs (AgNPs-CS-PSS-CS) and then antibodies of $A\beta$ (anti- $A\beta$) were fixed on LbL assembly (AgNPs-CS-PSS-CS@anti- $A\beta$). Herein, amine functionality of CS offers a plethora of sites for anti- $A\beta$ antibody immobilization that gives specific direction, high selectivity, and an adequate amount of antibody immobilization. For fabrication, synthesized GO was immobilized on an amine-modified gold-coated sensor chip via carbodiimide chemistry followed by AgNPs-CS-PSS-CS@anti- $A\beta$ immobilization on an activated GO surface. Inimitable features of LbL assembly showed improved selectivity towards $A\beta$ peptide whereas utilization of affinity biotransducer with a combination of plasmonic and non-plasmonic nanomaterial improved sensitivity and selectivity. Consequently, linearity range and limit of detection (LOD) of $A\beta_{1-42}$ antigens were found to be 2 fg/mL to 400 ng/mL and 1.21 fg/mL, respectively. Moreover, analysis of $A\beta_{1-42}$ in AD-induced rats confirmed the real-time-applicability of the designed SPR biosensor. Hence, GO surface decorated AgNPs-CS-PSS-CS@anti- $A\beta$ mediated SPR biosensor would provide a novel approach for exceptionally sensitive and selective $A\beta$ detection.

1. Introduction

Alzheimer's disease (AD) is a progressive, and irreversible neurodegenerative disease [1]. Subsequently, continuous progress in AD results in clinical dementia [2]. Importantly, AD is defined biologically by the presence of β -amyloid ($A\beta$) plaques and tau-containing neurofibrillary tangles in the brain [3]. It causes amnesic cognitive impairment in the prototypical form and non-amnesic cognitive impairment in the less common variants [3,4]. Literature divulged that AD is perhaps the leading prevalent form of dementia among individuals over the age of 65. It affects approximately 5 million individuals in the United States (US). As the population ages, the number of AD cases in the US is expected to climb to 16 million by 2050 [5]. Conventional diagnostic methods including imaging, laboratory analysis, examination, and

initial history of the patient have been preferred to diagnose AD [5,6]. Such methods are suffering from plenteous demerits including less detection accuracy, extremely expensive, time-consuming, etc. Moreover, there is no promising treatment existed for the management of AD whereas symptomatic treatment can endow with a short period of relief. As a result, there is necessary to establish a newish solution to diagnose AD and clinical dementia at an early stage, which can contribute to the improvement of individual life [6,7].

Merely on AD phenotype, it is complicated to determine the fundamental disease process concerned in AD. Herein, assorted biomarkers might be of considerable assistance in expediting the early recognition of AD [8]. As per literature, biomarkers are quantitative signals that are expressed within a certain stage of the ailment. It renders them essential for both diagnosis and tracking therapy response [9]. In the case of AD,

* Corresponding author.

E-mail address: rxpatilpravin@yahoo.co.in (P. Patil).

<https://doi.org/10.1016/j.ijbiomac.2022.06.129>

Received 3 February 2022; Received in revised form 24 May 2022; Accepted 18 June 2022

Available online 23 June 2022

0141-8130/© 2022 Published by Elsevier B.V.

numerous kinds of biomarkers have been investigated for AD diagnosis. Importantly, extracellular A β peptide is a well-known pathological biomarker of AD [6]. The diagnosis of AD and its consequential influence such as clinical dementia has made great strides since it was discovered to be accompanied by a fall in A β peptide levels in cerebrospinal fluid (CSF) [10]. Recently, the diagnosis of Parkinson's disease dementia based on the concentration of A β _{1–42} is also been widely reported [11]. As per published data, A β _{1–42} is accumulated in the brain before (10 to 15 years) onset of AD symptoms mainly pathological alterations and cognitive impairment [12]. A literature survey revealed that the classical immunoassays mainly Western blot and dot-blot are suffering from several demerits. It is a time-consuming process and needs washing continuously. In addition, it necessitates indirect read-outs as well as long incubation steps [13]. Presently, A β peptide is quantified using a sandwich enzyme-linked immunosorbent assay (ELISA) to differentiate between AD patients and healthy persons [6]. Herein, clinical diagnostic has a reasonably good reliability rate near about 80% to 90%. Despite this, a definitive AD diagnosis can only be finished after post-mortem [1,14]. As a result, ante-mortem identification of biomolecular indicators represents a fascinating approach to the advancement of AD diagnostic technology [1]. Therefore, there is the urge to produce a new option for ante-mortem recognition of AD biomarkers in the body fluids of an individual.

A time over the past two decades, there has been a lot of interest in constructing biosensors to precisely determine the extent of disease biomarkers [15]. Mainly, a biosensor is an analytical mechanism that is widely employed in the diagnosis of several life-threatening diseases. It recognizes biomarkers in specimens and/or solutions in a limited period of timeframe while maintaining excellent selectivity and responsiveness [6,16]. Emerging monitoring approaches are currently greatly benefiting from the introduction of nanomaterial-based biosensors, which have solved the existing shortcomings of traditional biosensors. Mainly, it covers sensitivity and selectivity by upgrading biorecognition layers [17]. Surface plasmon resonance (SPR) mediated sensing tool has become popular for examining biomolecular interactions mainly protein to protein, antibody to antigen, receptor to ligand, etc., [18]. Interestingly, SPR biosensors can bring unprecedented insights into linkages implicated in ailment diagnoses on a cellular scale. Furthermore, it provides the aptitude to distinguish biomolecules in varied environments. In addition, it furnishes speedy, real-time, label-free, as well as direct identification of interest analyte [15,18]. Several research publications on the SPR-mediated biomolecular interactions relevant to AD have previously been reported. Among these methods, SPR biosensor mediated on an antibody to antigen binding is a novel technique for AD diagnosis [6]. Detection of A β peptide has been reported using SPR-based biosensor [19] that provides the lowest detection limit due to the direct adsorption of biotransducer on the surface of sensor chip [6]. In 2016, Kim and co-authors developed a gold and silver mediated bimetallic chip-based SPR biosensor that offers 54.569 pg/mL of the detection limit for A β _{1–42} [12]. Moreover, the identification of small molecules (≤ 800 kDa) limits their applications. Notwithstanding this progress, the expenditure and period of the approach, as well as responsiveness and selectivity, will remain to be addressed in forthcoming experiments [6]. Presently, the utilization of the green approach for the synthesis of nanomaterials has widely preferred that resolve the issue of toxicity to biomolecules [20,21]. The utilization of plasmonic materials in SPR-based biosensor release a fresh avenue for sensitivity improvement. The tunable optical attributes of silver nanoparticles (AgNPs) help to improve the SPR signal [22]. In this connection, AgNPs are indeed becoming included in SPR biosensor diagnostic techniques to fabricate extremely precise and reliable nanosize biosensor frameworks. Moreover, such monitoring devices have been strengthened with the emergence of numerous nanomaterials and associated unique features [17,23]. The utilization of 2D graphene oxide (GO, non-plasmonic nanomaterial) provides numerous merits including improved sensitivity of SPR towards the ultra-small molecules, and immobilization of a

high number of receptors (example: antibody), etc. Interestingly, the conjugation of GO with plasmonic materials offers an enhanced SPR signal as compared to the bare plasmonic materials [18]. For this reason, we prepared the combined approach of GO and AgNPs to offer a synergistic presentation of SPR biosensor in terms of sensitivity and selectivity towards analyte.

The use of Layer-by-Layer (LbL) assembly is the utmost, unique approach in SPR mediated biosensors using cationic and anionic polymers. It provides stability to nanomaterials as well as offers specific orientation for the immobilization of bioreceptors such as antibody. Therefore, it resulted in sensitivity and selectivity improvement of biosensors [24]. Furthermore, LbL assembly is a simplified and adaptable console for biomolecule immobilization, which significantly reduces the necessity for bioreceptors [25]. Chitosan (CS, cationic polymer) has been extensively documented for the construction of LbL assembly owing to its propensity to encase nanoparticles through surface positive charge [26,27]. Furthermore, CS is a biocompatible and biodegradable polymer [28], and therefore it demonstrates biocompatibility with A β antibodies. Furthermore, the surface functionality of CS can offer an abundant position for the immobilization of preferred antibodies with a specific orientation. Altogether, the LbL assembly can influence the effectiveness of the SPR biosensor in terms of sensitivity, selectivity, etc.

The current endeavor intends to fabricate surface decorated CS-based LbL assemblies and their implementation in GO-based SPR biosensors for the exceptionally sensitive and selective recognition of A β antigen. In this study, AgNPs were produced using green precursor extract and employed as a plasmonic nanomaterial in an SPR biosensor. Furthermore, non-plasmonic GO nanosheets were produced using a modified Hummers method and mounted on the surface of the amine customized Au coated SPR sensor device employing carbodiimide chemistry. Moreover, LbL assembly using polymeric cations (CS) and anions (polystyrene sulphonate, PSS) was reported. At this juncture, the utilization of CS as cationic polymers on the surface of LbL assembly for immobilization of anti-A β antibodies exhibited high sensitivity and selectivity towards the A β peptide. To the best of our knowledge, this is the first documented biosensor that relied on a combined approach of LbL assembly and GO nanosheet for exceedingly responsive and selective identification of A β antigen. Hence, it potentially paved the direction for the advancement of a novel SPR biosensor that could be utilized in the sensing of AD, clinical dementia, and Parkinson's disease dementia.

2. Materials and methods

2.1. Materials

Amyloid β protein Fragment 1–42 (>95% HPLC, A β _{1–42}) and monoclonal anti- β -Amyloid (A β) antibody (Produced in mouse, purified from hybridoma cell culture) were purchased from Sigma Aldrich, St. Louis, USA. Amine modified sensor chip (sensor kit) was purchased from Nicoya Life sciences, Canada. Graphite flakes (> 99%) were obtained as a gift sample from Asbury Carbons, New Jersey (NJ), USA. Silver nitrate (99%) was purchased from Titan Biotech Ltd. Rajasthan, India. Chitosan (CS) was obtained from HiMedia Laboratories Pvt. Ltd. Poly (sodium 4 styrene sulphonate) [PSS, MW: ~70,000], bovine serum albumin (>98%, BSA), N-hydroxysuccinimide (NHS), and 1-[3-(di-methylamino)-propyl]-3-ethyl carbodiimide hydrochloride (EDC) were purchased from Sigma Aldrich, St. Louis, USA. *Terminalia catappa* L. ripe fruit was collected from the local area of Shirpur (Maharashtra). Potassium permanganate (99%, KMnO₄) was purchased from Research Lab Fine Chem Industries, Mumbai, India. Hydrogen peroxide solution (30% w/v, H₂O₂) was purchased from Loba Chemie Pvt. Ltd. Streptozocin was purchased from EMD Millipore Corp., Billerica MA, USA. Nuclease-free water was obtained by Invitrogen Bioservices India Pvt. Ltd. Double distilled water (HPLC grade) was purchased from Avantor Performance Materials India Limited, Thane, India. All of the reagents used in this

investigation were of analytical quality and were utilized as they were received, with no additional purification.

2.2. Methods

2.2.1. Synthesis of GO via modified hummers method

In this stage, GO was produced employing a modified Hummers method, which was slightly improved [29]. In brief, 54 mL of sulfuric acid (H_2SO_4) and 6 mL of phosphoric acid (H_3PO_4) were merged appropriately before agitating for 15 min using a laboratory magnetic stirrer at 200 rpm. Following that, 0.45 g of graphite flakes were poured into the previously formed solution with constantly mixing. Then, 2.64 g of KMnO_4 was gradually poured, and the combination was agitated for up to 6 h until the color of the slurry turned dark green. Then, the KMnO_4 was removed from the reaction mixture by progressively dropping H_2O_2 (1.35 mL) and mixing for 10 min. Following that the synthesis was accomplished, and the resulting slurry was chilled to room temperature. Subsequently, this slurry was purified three times with hydrochloric acid (HCl) and double distilled water (DDW, 1:3 ratio) and cold centrifuged at 12,000 rpm for 30 min at 25 °C employing a laboratory cold centrifuge. Lastly, the resulting GO was subjected to drying at 55 °C for 24 h before being submitted to diverse spectroscopical characterizations.

2.2.2. One-pot green synthesis of silver nanoparticles (AgNPs)

Initially, 100 g of *Terminalia catappa* L. ripe fruit was collected from the local area of Shirpur. Then, the fruit was cleaned using DDW and checked for stuck dirty materials. The outer soft epicarp was decanted and the shell was used for extract preparation. Afterward, the shell was dried at 60 °C, in a hot air oven for 8 h, and then the dried part was then boiled at 60 °C in distilled water for up to 1 h. After that, the extract was cooled at room temperature, centrifuged at 7000 rpm for 30 min, and the supernatant was collected and filtered using a 0.22 μm membrane filter. This purified extract was stored at 24 °C and used for further process. The AgNPs were synthesized using a constant volume of extracts (5 mL) under optimized experimental conditions such as temperature (50 °C), with a 10 mL constant volume of AgNO_3 solution (7 mM). Finally, the formation of deep reddish-brown colour was observed after 24 h, which revealed the development of AgNPs [30]. The reaction was monitored by checking the absorbance of the reaction mixture for up to 24 h using UV visible spectroscopy. The obtained green synthesized AgNPs were freeze-dried using a laboratory freeze dryer (Freezone12, Labconco, MO, USA) wherein AgNPs were prefrozen at –30 °C for 12 h. After that, the primary drying of AgNPs was accomplished at –53 °C and 0.016 mbar for 24 h. Then, the secondary drying of AgNPs was finished at 10 °C for 8 h followed by drying at 25 °C for 4 h with a continuing boost in temperature at 1 °C/min. To finish, the temperature of the cold trap was maintained at –53 °C until the finishing point of the drying process. The AgNPs powder that formed was then employed in further assessment.

2.2.3. Characterization of synthesized GO and AgNPs

To validate successful synthesis, the green synthesized GO and AgNPs were examined using multiple spectroscopic techniques. The UV–visible spectra of GO and green synthesized AgNPs have been recorded between 800 nm to 400 nm using UV 1800 spectrophotometer (Shimadzu, Japan). The Fourier-transform infrared spectroscopy (FT-IR, Thermo Nicolet, Avatar 370) was preferred to characterize the functional group present in the GO and AgNPs. The particle size analysis, PDI, and zeta potential of synthesized GO and AgNPs were measured using Nanoplus 3 Particulate System (Micromeritics, USA). After that, elemental analysis of GO and AgNPs was done using energy dispersive spectroscopy using FESEM/EDAX (OXFORD XMX NO). The morphology, size, and electron diffraction pattern (SAED) of the GO and AgNPs were imaged using High-resolution transmission electron microscopy (HR-TEM, Jeol/JEM 2100, and Source: LaB6). Afterward, X-ray

photoelectron spectroscopy (XPS) was acquired with a high-performance 0–5 keV Ar + ion gun (physical electronics, IIT Roorkee, India). In Bruker D8 development, Powder X-ray diffraction (PXRD) of synthesized GO and AgNPs was recorded using Bruker D8 Advance (STIC Cochlin, India). Raman analysis of GO was done using Horiba (HR800-UV) confocal micro-Raman spectrometer at 532 nm laser.

2.2.4. Development of layer-by-layer (LbL) assembly

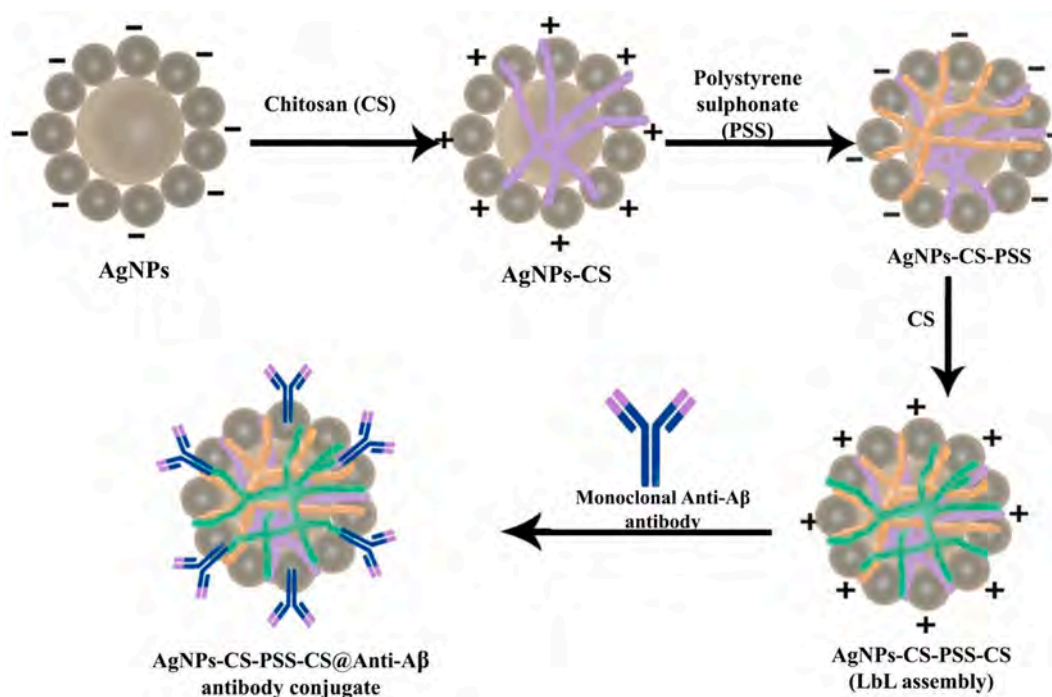
To design LbL assembly, accurately weighed 10 mg/mL of AgNPs solution was prepared using deionized (DI) water and then 50 mL of this solution was added into CS solution (4 mg/mL, cationic polymer). The obtained AgNPs@CS suspension was subjected to sonication for 45 min followed by centrifugation at 20,000 rpm for 30 min for separation of LbL assembled AgNPs (AgNPs-CS) from the remaining positive polyelectrolyte. At last, the supernatant was then discarded and washed timely using DI water to remove any unbound polyelectrolyte. Afterward, AgNPs-CS was dried using freeze-drying and subjected to the zeta potential analysis to confirm the successful layering of cationic polymer (AgNPs-CS). After the confirmation of surface charge, the dried powder of AgNPs-CS was suspended in the anionic polymer 1% PSS for 10 min to form a second LbL assembly (AgNPs-CS-PSS). In this step, cold centrifugation and washing were repeated as per the abovementioned process to eliminate the unbound anionic polyelectrolyte, and then it was dried using a freeze-drying process. The same process was repeated for the third layer (AgNPs-CS-PSS-CS) by using a CS solution. Simultaneously, zeta potential analysis was employed to monitor the surface charge of the LbL assembly at each stage. Freeze-drying was used for drying AgNPs-CS-PSS-CS. In freeze-drying, the LbL assemblies were prefrozen at –30 °C for 24 h. After that, the primary drying of LbL was performed at –53 °C and 0.016 mbar for 24 h. This resulted in LbL powder being used for subsequent evaluation studies including particle size analysis, zeta potential, PDI, HR-TEM, and FTIR.

2.2.5. Fabrication of AgNPs-CS-PSS-CS@anti-A β antibody (AgNPs@anti-A β) conjugates

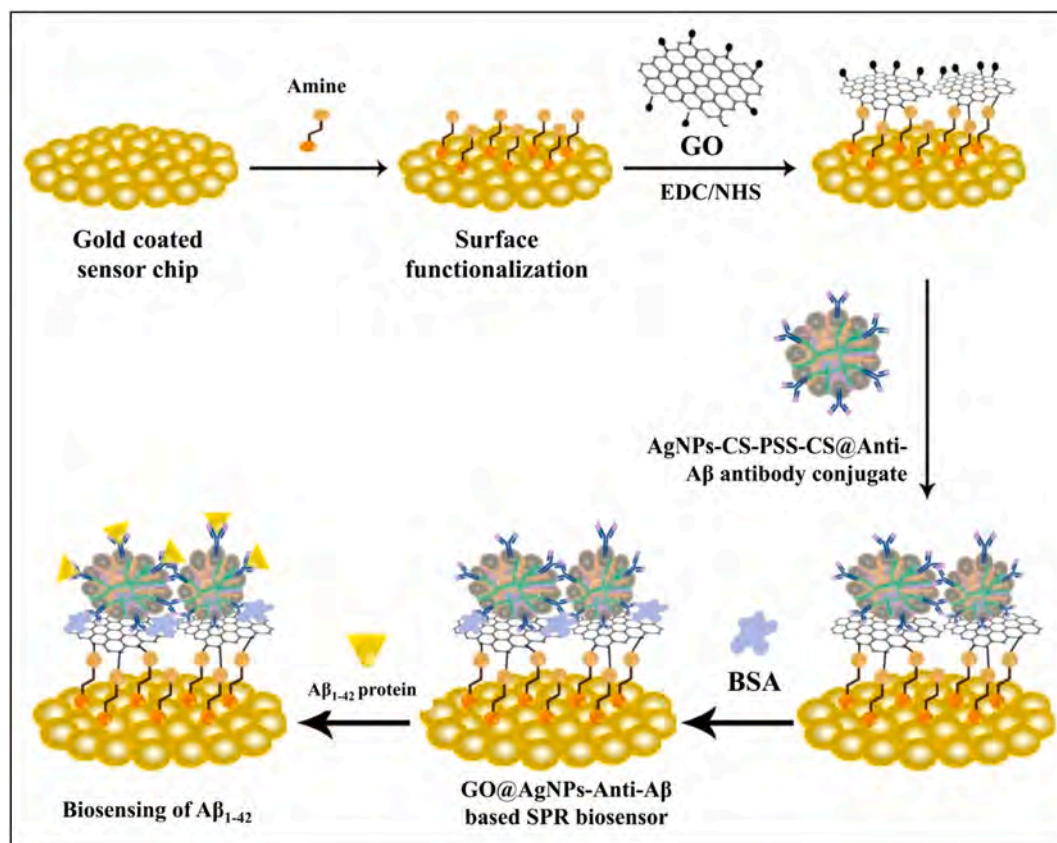
In this part, monoclonal anti-A β antibody (form: buffered aqueous solution concentration: 1.5 mg/mL) was preferred for fabrication of AgNPs-CS-PSS-CS@Anti-A β antibody conjugate. Firstly, 1 mg/mL of 5 mL solution was prepared using AgNPs-CS-PSS-CS in nuclease-free water at 20 °C. Then, this prepared solution was degassed using sonication for 5 min. After that, the EDC/NHS (1:1, 50 μL) solution was prepared to activate the C-terminal carboxylic functional group. Finally, the C-terminal carboxylic functions of the monoclonal anti-A β antibody were activated by the EDC /NHS mediated carbodiimide chemistry and then condensed on the amine moiety of the external cationic layer (CS) of the AgNPs-CS-PSS-CS assembly. The conjugate was subjected to aside for 5 min to accomplish complete immobilization of antibody at 8 °C. The immobilized AgNPs-CS-PSS-CS@Anti-A β antibody was characterized using a particle size analyzer to confirm the surface potential and particle size of the AgNPs-CS-PSS-CS@Anti-A β antibody conjugate. Scheme 1 depicts the fabrication of AgNPs-CS-PSS-CS LbL assembly followed by immobilization of monoclonal anti-A β antibody by carbodiimide chemistry.

2.2.6. Fabrication of GO@AgNPs-anti-A β based SPR biosensor

Scheme 2 depicts the final assembly of the GO@AgNPs-Anti-A β based SPR biosensor. Initially, the amine-modified gold (Au) coated (thickness: 50 nm) glass chip was fixed in an openSPR (excitation wavelength: 632.8 nm, 5 mW), containing a sensor cavity. The surface of the amine-modified SPR sensor chip was washed using phosphate buffer saline (PBS, 150 μL) whereas the air bubbles were removed via injecting isopropyl alcohol (150 μL , 80%v/v) into the channel using a sample injection port. Then, a prepared 1 $\mu\text{g/mL}$ (100 μL) of GO nanosheet solution was injected (flow rate: 10 $\mu\text{L/min}$) to assemble it on amine-modified Au film by electrostatic interaction. The stability of the immobilized GO nanosheet on the surface of the sensor chip was



Scheme 1. Fabrication of LbL assembly (AgNPs-CS-PSS-CS) on the surface of green synthesized AgNPs using cationic polymer (CS) and anionic polymer (PSS) followed by immobilization of monoclonal anti-A β antibody on the surface of AgNPs-CS-PSS-CS (AgNPs-CS-PSS-CS@Anti-A β antibody)



Scheme 2. Schematic presentation of fabrication of GO@AgNPs-Anti-A β based SPR biosensor using GO nanosheet, AgNPs-CS-PSS-CS@Anti-A β antibody conjugate, and amine-modified Au-coated glass chip.

measured through repeated washing using PBS. After that, the carboxyl groups of GO nanosheets were activated with 50 μL of a mixture of 0.4 M EDC (70 μL) and 0.1 M NHS (70 μL) for 5 min offering many possible sites available at the GO surface for antibody binding. After that, 200 μL PBS was injected to wash excessive EDC/NHS from the surface of the biosensor. Different concentrations of AgNPs-Anti-A β were evaluated to optimize the saturation concentration for the SPR biosensor. The optimized concentration of AgNPs-Anti-A β solution (25 $\mu\text{g}/\text{mL}$) was prepared using PBS (pH 7.4) and immobilized on a surface of GO nanosheets with a flow rate of 10 $\mu\text{L}/\text{min}$. It facilitates the covalent bonding with amino groups of the Anti-A β antibody which was immobilized on the surface of conjugates of AgNPs-CS-PSS-CS@Anti-A β antibody. Finally, 200 $\mu\text{g}/\text{mL}$ of BSA solution was prepared in nuclease-free water at 20 $^{\circ}\text{C}$ and then injected via an SPR sample channel with a flow rate of 10 $\mu\text{L}/\text{min}$. Interestingly, it assists to block the non-bonded carboxy functional group of GO nanosheet that helps to restrict the untargeted proteins.

2.2.7. Detection of A β_{1-42} using GO@AgNPs-anti-A β SPR

The key principle of the SPR biosensor for A β_{1-42} identification was based on the capture of the A β_{1-42} peptide with a monoclonal Anti-A β antibody. Initially, 0.5 mg of A β_{1-42} antigen was diluted using 2 mL PBS (pH 7.4) at 20 $^{\circ}\text{C}$. After that, different concentrations of A β_{1-42} antigen were prepared from a range of 2 fg/mL to 1000 ng/mL (final volume: 1000 μL) using pH 7.4 PBS. For the estimation of A β_{1-42} , the prepared lower concentration of A β_{1-42} antigens was injected via a sampling port with a flow rate of 10 $\mu\text{L}/\text{min}$ at programmed temperature 25 $^{\circ}\text{C}$. After equilibrium, glycine hydrochloride (pH 1.2) was used as a washing buffer to regenerate the GO@AgNPs-Anti-A β SPR biosensor by detaching the A β_{1-42} antigens from the sensor surface.

2.2.8. Detection of A β_{1-42} in AD induced animals CSF and blood plasma

Initially, a real-time analysis of A β_{1-42} in adult male Wistar rats (300–350 g) animal blood and saliva was performed (Animal ethical committee reference letter no: IAEC/RCPIPER/2016–17/37). In this study, the A β_{1-42} antigen was individually spiked (40 ng/mL) in saliva and blood samples collected from healthy animals. Then, the prepared spiked samples of A β_{1-42} were injected into fresh GO@AgNPs-Anti-A β SPR biosensor via a sampling port with a 10 $\mu\text{L}/\text{min}$ flow rate. The change in the response unit was measured to evaluate the real-time applicability of the GO@AgNPs-Anti-A β SPR biosensor. Detection of A β antigen in AD-induced animals was completed through the following process. At first, adult male Wistar rats (300–350 g) were used for induction of AD. Initially, rats were injected with intracerebroventricular (icv) streptozocin (STZ, 3 mg/kg) twice on day 1 and day 3 under anesthesia using chloral hydrate (240 mg/kg, intraperitoneal route, in 4% solution). Then, it was analyzed the learning and memory behavior. Simultaneously, blood and saliva samples were collected from AD-induced animals and analyzed for the occurrence of A β antigen. For the 21 days, AD-induced wistar rats were sacrificed under anesthesia and the collected CSF brains of AD-induced rats were stored at -40°C . Finally, samples were analyzed for identification of A β antigen using GO@AgNPs-Anti-A β SPR biosensor at 25 $^{\circ}\text{C}$.

2.2.9. Anti-interference study and other features of the biosensor

Selectivity testing is a key aspect of evaluating the built biosensor [31]. In this shade, the anti-interference potential of GO@AgNPs-Anti-A β SPR biosensor was performed by utilizing a variety of molecules including hemoglobin, BSA, cholesterol, glucose, albumin, lactoferrin, protease, citric acid, etc. to ensure that the constructed biosensor could test precisely. In brief, selected interfering agents and A β antigen was individually spiked (40 ng/mL) pH 7.4 PBS buffer (0.1 mol/L) at 20 $^{\circ}\text{C}$. Then, the prepared concentrations were injected into fresh GO@AgNPs-Anti-A β SPR biosensor via a sampling port with a 10 $\mu\text{L}/\text{min}$ flow rate. The change in response unit was measured to evaluate the high selectivity potential of GO@AgNPs-Anti-A β SPR biosensor towards A β_{1-42} in

the existence of numerous interfering substances. Furthermore, other important parameters including reproducibility and stability of fabricated SPR biosensors were also executed [32]. As per literature, repeatability is also important for determining the biosensor's usefulness. In this, six GO@AgNPs-Anti-A SPR biosensors were created. Then, biosensors were characterized under identical sensing circumstances with 4 ng/mL of A β_{1-42} peptide in triplicates. Another significant element of a biosensor is its stability [33]. In present work, stability of the fabricated GO@AgNPs-Anti-A β SPR biosensor was performed using the same concentration of A β_{1-42} peptide for continuously 48 h. A similar experimental condition, 400 fg/mL of A β_{1-42} peptide was evaluated in triplicate for different time intervals.

3. Results and discussion

In the present study, GO was synthesized using modified Hummers methods that offer a larger surface area for immobilization of bio-conjugates. The green synthesis of AgNPs was achieved using a green precursor and subjected to the development of LbL assembly. Bio-conjugate of LbL assembly and antibody of A β_{1-42} was developed wherein anti-A β antibodies were immobilized on the surface of LbL assembly. Finally, biosensing of the A β_{1-42} peptide was accomplished using a designed bioconjugate. The different parameters such as selectivity, real-time analysis, stability, and reproducibility of GO@AgNPs-Anti-A SPR biosensor were performed.

3.1. Characterization of GO by green approach

Fig. 1A demonstrates the UV spectra of GO. In brief, the GO has exhibited a characteristic absorption peak at 234 nm and a slightly low intense shoulder peak at 300 nm (Fig. 1A), which corresponds to $\pi-\pi^*$ transitions of aromatic C=C bonds and n- π transitions of C=O bonds, respectively [34]. Hence, it confirms the synthesis of GO from graphite flakes. Fig. 1B shows the FTIR spectra for the GO nanosheet. Briefly, the occurrence of diverse types of oxygen functionalities in FTIR has confirmed the complete oxidation of graphite flakes. The existence of a broad and wide peak at 3438.12 cm^{-1} can be attributed to the O—H stretching vibrations. The carbonyl (C=O) group stretching was observed at 1631.86 cm^{-1} , whereas OH bending (deformation) vibration and C—O stretching were obtained at 1383.78 cm^{-1} , and 1216.54 cm^{-1} , respectively. In a nutshell, it confirmed the occurrence of oxygen-containing functionality such as hydroxyl, carboxyl, and epoxy groups [35]. The presence of oxygen functionality can provide the binding site for the immobilization of biomolecules. Fig. 1C and D demonstrate the particle size and zeta potential of GO. Herein, particle size and zeta potential analysis was performed to confirm the distribution (or average diameters) and stability of GO nanocomposite, respectively. The particle size of the synthesized GO nanosheet was found to be 88.7 nm (Fig. 1C) whereas, the PDI of GO nanosheet dispersion was found to be 0.285. It confirmed the prepared GO available in nanosize with uniform distribution in water. In the case of the zeta potential of GO, it was found to be -21.48 mV (Fig. 1D). In conclusion, zeta potential analyses of prepared GO nanosheets confirmed the stability of GO dispersion at working conditions.

Figs. 2A and B depict the surface morphology of the GO nanosheet. The conversion of graphite flakes to GO nanosheets was exhibited randomly aggregated and crumpled thin sheets. Moreover, it showed wrinkles and folds on the surface of GO nanosheets. It has been mentioned that the insertion of oxygen in flakes of graphite resulted in the separation of flakes into a thin nanosize sheet. Therefore, it confirmed the successful exfoliation of nanosheets and the formation of GO [35]. The EDAX investigation of the synthesized GO showed 48.89 wt% of carbon content and 40.32 wt% of oxygen assured the presence of carbon and oxygen only (Fig. 2C). In a nutshell, the elemental composition was confirmed by the purified form of the GO nanosheet [36]. HR-TEM analysis as shown in Figs. 2D and E investigated the surface

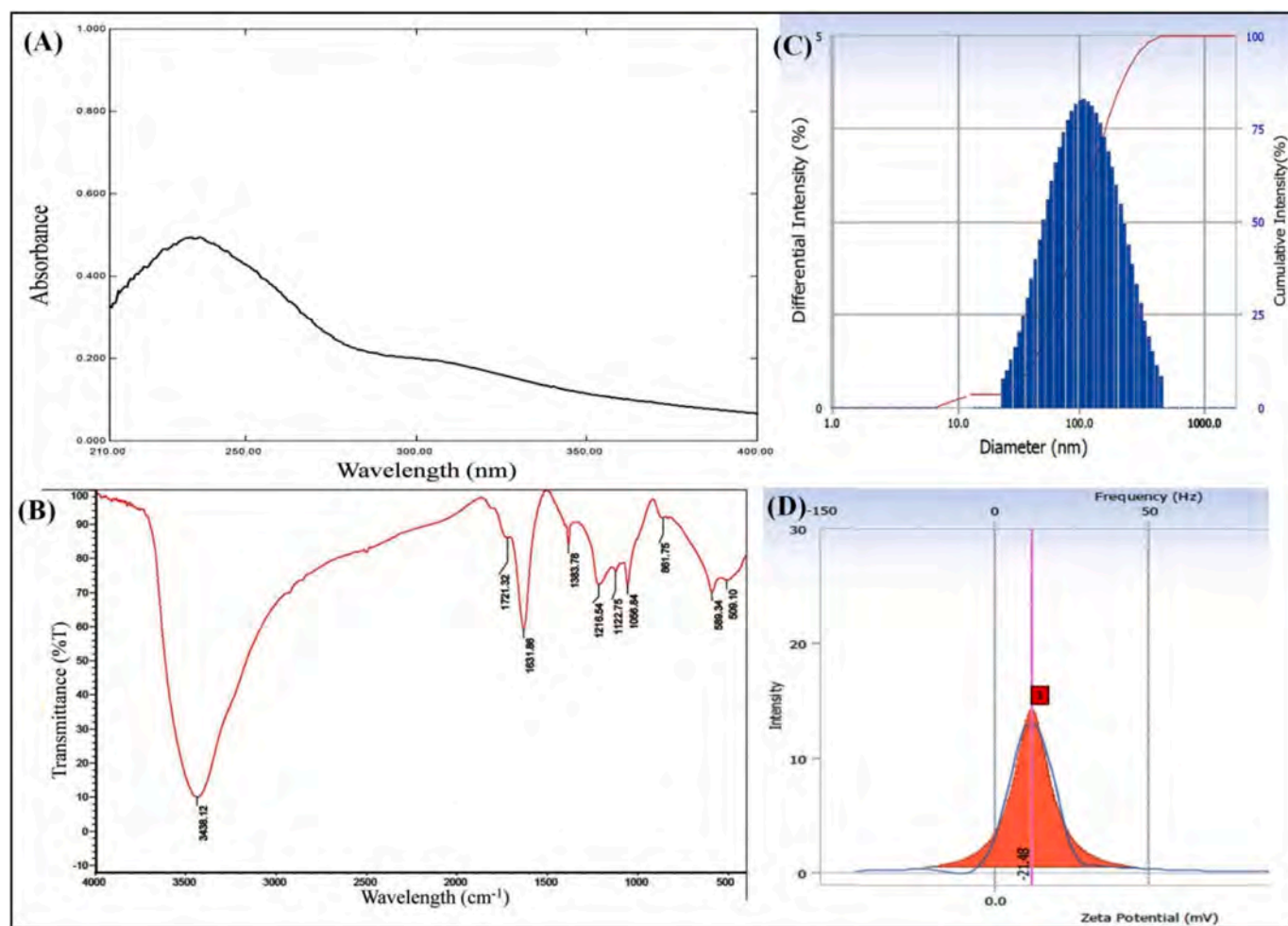


Fig. 1. (A) UV absorption spectra of GO; (B) FTIR spectra for the GO; (C) particle size of and (D) zeta potential of GO.

morphology and structure of the synthesized GO. It revealed the graphite flakes successfully oxidized into the GO nanosheet. The morphology of multilayer GOs was found to be rough surface, flake-like shape, not crumpled, and corrugated together with non-uniform particle size [36]. Moreover, the apparent spherical rings in the SAED pattern also reveal the crystalline property of GO (Fig. 2F).

Raman spectra of GO exhibited two bands mainly the D band and G band. In brief, the breathing mode of j-points of A_{1g} symmetry was obtained at 1360 cm⁻¹ (D band) whereas first-order scattering of E_{2g} photos by SP² carbon was found at 1590 cm⁻¹ (G band). Herein, the *I* (D)/*I* (G) of GO was found to be 0.85 indicating the hydrophilic nature of GO. Mainly, the ratio of the *I* (D)/*I* (G) provides the graphitic composite containing defect levels. A literature survey revealed that the intensity ratio is <1 confirmed the formation of GO whereas >1 confirmed the formation of the reduced form of GO (hydrophobic) nanomaterial [37]. Diffractograms of dry powder of separated graphite flakes (Fig. 2H-i), and GO nanosheets (Fig. 2H-ii) were investigated to study the material structure. In the case of graphene, a high intense diffraction peak was observed at $2\theta = 26.34^\circ$, which reveals the high crystallinity nature of graphene. In the case of GO, a prominent peak was observed at a lower angle ($2\theta = 10.10^\circ$, interlayer spacing: 0.29 nm) signifies the complete synthesis of nanosize GO from graphite flakes. The diffraction peak was found at $2\theta = 26.0^\circ$ (interlayer spacing: 0.85 nm), which may be because of the intercalation of oxygen functionalities as well as water molecules into carbon nanolayers [37,38]. Fig. 2I demonstrates the XPS wide scan spectrum of GO. Herein, the survey spectrum shows the two intense peaks for carbon and oxygen at 283.6 eV (sp² carbon) and 531.3 eV (C-

OH, -C=O) binding energy, respectively. In this spectrum, no addition peak was obtained that assured the purity of GO. In conclusion, it confirmed the existence of oxygen functionalities mainly carboxy, and epoxy on the surface of the GO nanosheet [39].

3.2. Characterization of green synthesized AgNPs

Fig. 3(A) UV absorption spectra of silver nitrate (i), *Terminalia catappa* L. ripe fruit shell extract (ii), green synthesized AgNPs (iii). In this study, after the addition of the prepared extract of *Terminalia catappa* L. ripe fruit shell, the colour of silver nitrate solution converted into an amber colour that confirmed the reduction of Ag⁺ to Ag⁰ (Fig. 5 A-iv), and finally a green synthesis of AgNPs [40]. In addition, the UV visible spectra of synthesized AgNPs displayed the surface plasmon absorption band at 416.5 nm (Fig. 3A-iii) confirming the existence of smaller size AgNPs. Herein, the generation of AgNPs at different time intervals showed a boost in absorption band intensity when the reaction time improved. After 24 h, there were no changes in peak intensity that assured the completion of the reaction. Taken as a whole, *Terminalia catappa* L. ripe fruit shell extract acted as a reducing and stabilizing agent for silver ions that provides the smaller size AgNPs [30,40]. Fig. 3B shows the FTIR spectra of ripe fruit shell extract of *Terminalia Catappa* (i) and green synthesized AgNPs (ii). Briefly, FTIR spectra of shell extract showed bands at 3328 cm⁻¹ which were assigned to OH stretching, C=O stretching at 1619 cm⁻¹, and C—O stretching at 1038.06 cm⁻¹ (Fig. 3B-i). Hence, it confirmed the presence of poly-phenolic compounds in the extract [36]. On the other hand, FTIR spectra

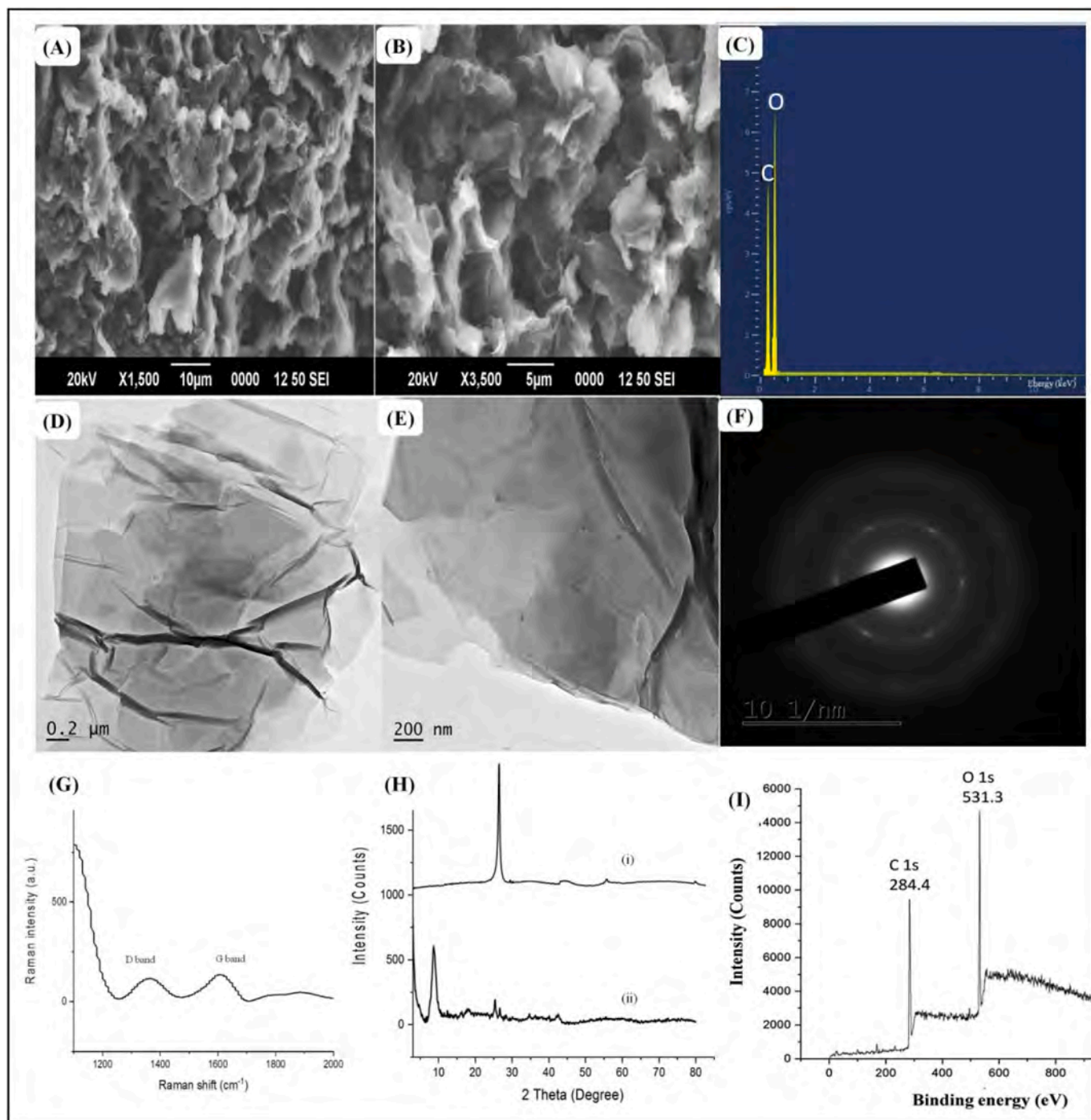


Fig. 2. A and B SEM image of GO nanosheet; (C) EDAX spectra of GO; (D, E) HRTEM images of GO and (F) selected area electron diffraction (SAED) pattern of GO; (G) Raman spectra of GO (H) PXRD spectra of graphite flakes (i), and GO (ii); (I) XPS survey scan spectrum of GO.

of green synthesized AgNPs showed bands at 3346 cm^{-1} which were assigned to OH stretching, $\text{C}=\text{O}$ stretching at 1627 cm^{-1} , and $\text{C}-\text{O}$ stretching at 1028.06 cm^{-1} (Fig. 3B-ii). To summarize, the shifting of band wavelength in FTIR of AgNPs confirmed the capping of AgNPs by different functional groups present in the extract. The particle size of green manufactured AgNPs was investigated using Nanoplus3 (DLS research), which affords details on particle size diversity and PDI of the AgNPs solution. Fig. 3C depicts the particle size distribution of green synthesized AgNPs in solution. Notably, the size of green synthesized AgNPs was monitored upto the completion of the reaction. As a result, it showed 55.60 nm of average hydrodynamic particle size whereas the PDI of AgNPs was found to be 0.279 assuring the monodispersity of

nanoparticles. On the whole, it confirmed the green synthesis of monodispersed AgNPs within the range of nanometer. As per literature, zeta potential provides information about the stability of green synthesized metal nanoparticles in provided dispersion. Herein, the zeta potential of AgNPs has been reported to illustrate the surface charge, which appeared to be negative for green synthesized AgNPs (-27.01 mV , Fig. 3D). The high negative values indicate particle repulsion, which results in higher stability of AgNPs and avoidance of agglomeration [41]. In conclusion, it assured the synthesis of stable and nanosized AgNPs by the green synthesis method.

The elemental composition of AgNPs was measured using EDAX analysis which provides the absolute composition and purity of the

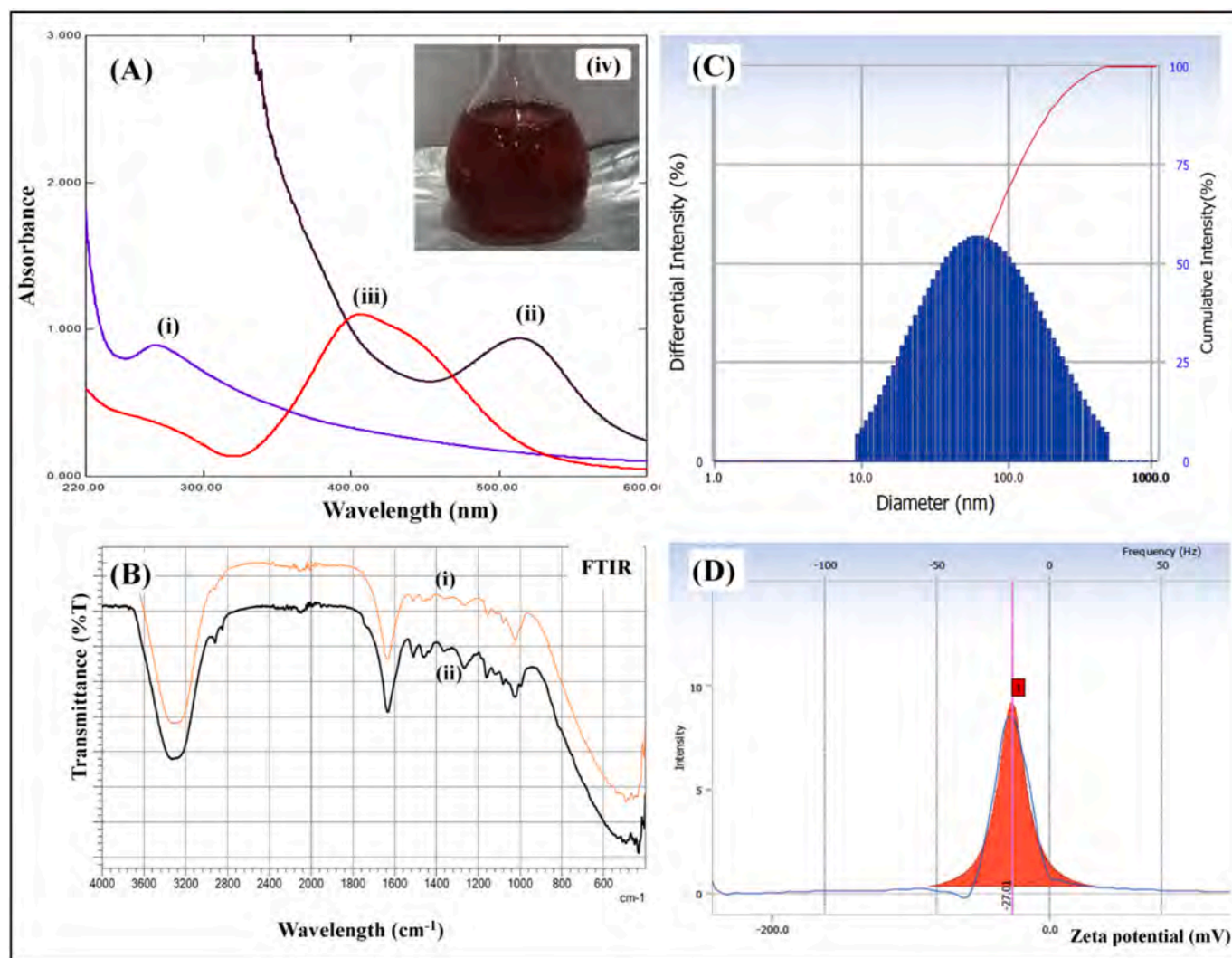


Fig. 3. (A) UV absorption spectra of silver nitrate (i), *Terminalia catappa* L. ripe fruit shell extract (ii), green synthesized AgNPs (iii), and image of AgNPs (iv). (B) FTIR spectra of *Terminalia catappa* L. ripe fruit shell extract (i), green synthesized AgNPs (ii). (C) Particle size analysis and (D) Zeta potential of green synthesized AgNPs. (For interpretation of the references to colour in this figure legend, the reader is referred to the web version of this article.)

prepared AgNPs. Fig. 4A demonstrates 35.68 wt% compositions of silver 'Ag' along with that 35.67 wt% oxygen (O) and 19.94 wt% of carbon (C) were observed. The strong signal in the 'Ag' region gives the authentication of 'Ag' without other contaminants. The Diffractogram of green synthesized AgNPs is depicted in Fig. 4B. Principally, the diffractogram of AgNPs revealed the exact nature of AgNPs. Herein, Bragg's model diffraction peak at 2θ at 38.09° and 64.45° confirmed the crystalline nature of AgNPs [36]. The obtained PXRD pattern of AgNPs confirmed the complete reduction of Ag^+ ions due to the ripe fruit shell extract of *Terminalia Catappa*. The HRTEM images of prepared AgNPs divulged the surface morphology, shape, and size of nanoparticles. The HRTEM images of AgNPs (Fig. 4 C and D) and the SAED pattern of AgNPs (Fig. 4 E). The obtained HRTEM images indicated that the morphology of the synthesized AgNPs is spherical with polydispersed in solution [42]. The AgNPs size range was found to be 14.36 nm to 21.80 nm whereas the apparent spherical rings in the SAED pattern reveal its polycrystalline property.

In this work, XPS analysis was used to investigate the composition and oxidation state of the AgNPs. In brief, the typical survey spectrum of the green synthesized AgNPs revealed the presence of Ag, C, N, and O (Fig. 5A). Principally, the existence of silver (Ag) metal was confirmed due to the occurrence of the strong signal of Ag 3d (~ 496.8 eV). Moreover, the presence of carbon (C) was confirmed due to the C 1s peak

obtained at ~ 284.3 eV of binding energy. It assured that the capping and stabilizing of the AgNPs by phytoconstituents present fruit shell extract. The XPS spectrum of oxygen (O) was found at ~ 531.2 eV of binding energy. Fig. 5B shows the Ag 3d high-resolution XPS spectrum. The Ag 3d_{3/2} and Ag 3d_{5/2} peaks are separated into two sets at 368.21 eV/368.89 eV and 366.93 eV/367.47 eV, respectively (Fig. 5B). Metallic 'Ag' is responsible for the peaks at 367.47 eV and 368.89 eV. In these spectra, loss characteristics are detected on the stronger binding energy edge of each 'Ag' metal spin-orbit component. Moreover, the spectrum peak in the C 1s is related to various identical peaks with binding energies of 284.29 eV, 285.57 eV, and 288.14 eV. Possibly, these peaks are ascribed to the C 1s (Fig. 5C) such as carboxyl carbon ($-\text{O}-\text{C}=\text{O}$), and carbon ($-\text{C}-\text{O}$). The peak of O 1s has also been deconvoluted into two bands as shown in Fig. 5D. Herein, the peak at the lower energy side (530.54 eV) can be ascribed to the O 1s core peak of O^{2-} bound to metal (Ag^+). Notably, the other peak located at 532.35 eV should possibly be attributed to the oxygen (O) in the carboxyl functional group ($-\text{C}=\text{O}-$) that bounds to the AgNPs surface. The peak at 534.74 eV existed which maybe because of the $-\text{CH}_2-\text{O}-\text{CH}_2$ backbone.

3.3. Characterization of LbL (AgNPs-CS-PSS-CS) assembly

In this part, the deposition of CS and PSS layers of AgNPs was

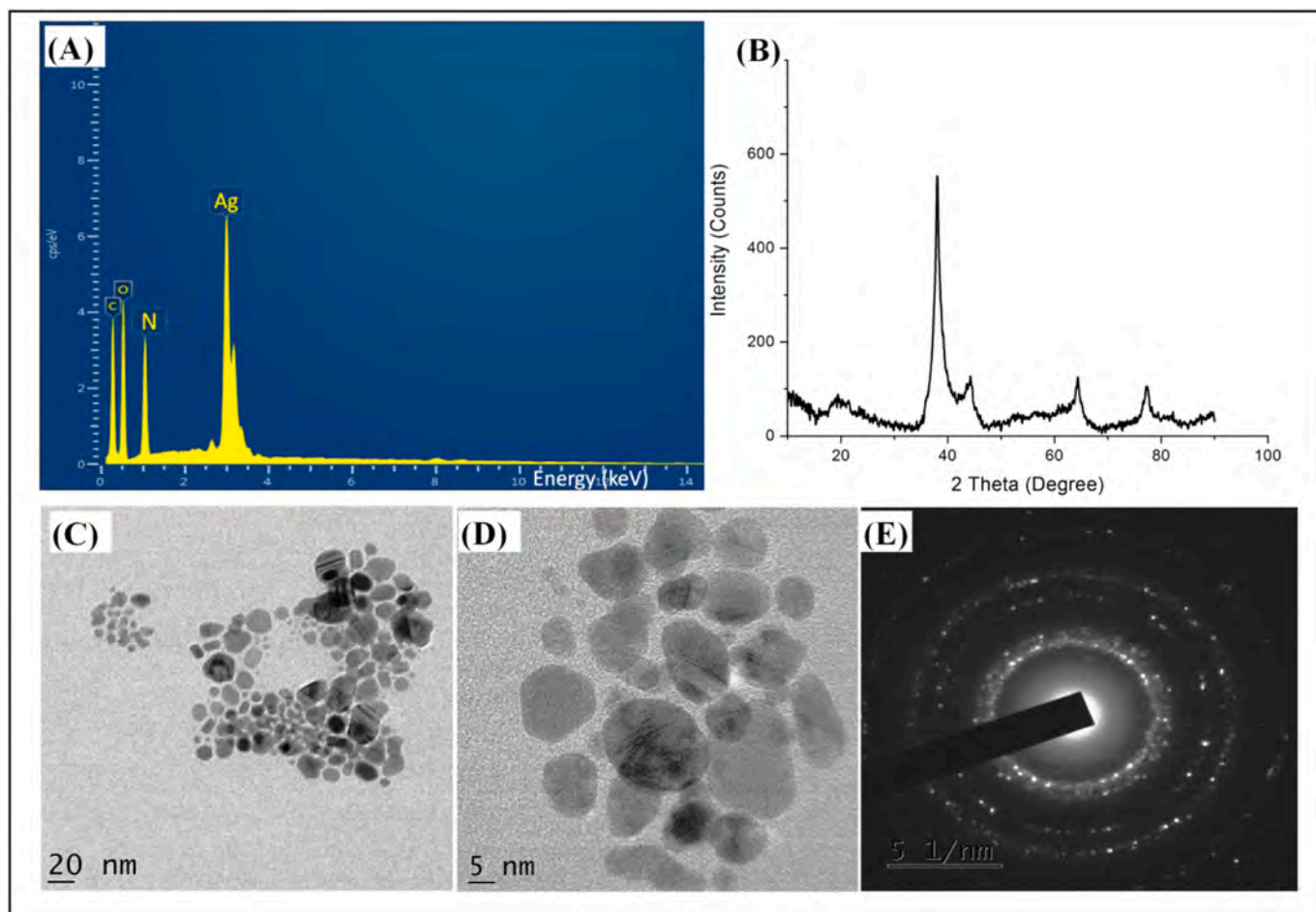


Fig. 4. (A) EDAX spectra of green synthesized AgNPs; (B) diffractogram of green synthesized AgNPs; (C and D) HR-TEM images of AgNPs; (E) SAED pattern of AgNPs. (For interpretation of the references to colour in this figure legend, the reader is referred to the web version of this article.)

checked using an increased average diameter of coated AgNPs. In brief, the size of green synthesized AgNPs and prepared LbL assembly was measured using Nanoplus 3 (Fig. 6A). Initially, the coating of CS on the surface of AgNPs (AgNPs-CS, Fig. 6A) shows the 89.4 nm average diameter (PDI: 0.267) that somewhat increased as compared to uncoated AgNPs (55.6 nm, PDI: 0.279). After that, the AgNPs-CS-PSS and AgNPs-CS-PSS-CS assembly showed a rise in diameter of LbL assembly with respective PSS and CS layer deposition. Particularly, the average particle size of AgNPs-CS-PSS and AgNPs-CS-PSS-CS was found to be 111.1 nm (PDI: 0.222) and 129.7 nm (PDI: 0.424). In this, coating of CS and PSS on the surface of AgNPs resulted in a rise in the actual diameter of assembly. In addition, the successful deposition of cationic polymer (CS) and anionic polymer (PSS) on the surface of green synthesized AgNPs was confirmed through zeta potential analysis (Fig. 6B). Initially, the zeta potential of prepared AgNPs solution was found to be -28.34 mV. The zeta potential of CS and PSS was found to be $+36.39$ mV and -31.58 mV, respectively confirming their cationic and anionic nature. Interestingly, the initial coating of AgNPs using CS (AgNPs-CS) was shown a positive surface zeta potential of $+29.01$ mV that confirming the deposition of the cationic CS layer. Then, deposition of an anionic layer of PSS on the surface of AgNPs-CS developed the AgNPs-CS-PSS assembly that showed the negative zeta potential of about -21.74 mV, which confirmed the successful deposition of PSS on the cationic layer. Finally, the deposition of the third layer of polymer (CS) on the surface of AgNPs-CS-PSS has demonstrated the zeta potential of about $+33.47$ mV that assures the formation of CS coating on the surface of AgNPs-CS-PSS assembly. Herein, the zeta potential of CS and PSS within the acceptable range helps to stabilize the AgNPs. Mainly, the final

assembly containing cationic amino surface functional groups on the surface of CS offers the immobilization of Anti-A β antibodies via activation of carboxyl functional groups. Herein, the adsorptions of the CS offer plenty of amine group (NH_2) that get interact with PSS electrostatically. Overall, particle size analyses and zeta potential measurements revealed the depositing of CS and PSS on the surface of green synthesized AgNPs, as well as the successful production of LbL assemblies. After that, FTIR analysis was performed to confirm the synthesis of LbL assembly. Firstly, the FTIR spectra of green synthesized AgNPs showed strong intense peaks at 3340 cm^{-1} and 3430 cm^{-1} that confirmed the presence of hydroxyl ($\text{O}-\text{H}$) and amine ($\text{N}-\text{H}$) functional groups (Fig. 6C). Concisely, it confirmed the presence of poly-phenolic compounds, proteins, and amino acids in the extract. Moreover, the intense peak at 1682 cm^{-1} confirmed the occurrence of the amide I band whereas the peak at 1350 cm^{-1} assured the existence of the amide I band and $-\text{C}-\text{N}-$ stretching. Possibly, the band of amide I was linked to the carbonyl group stretch mode ($\text{C}=\text{O}$) connected to the amide bond [43]. The characteristic peaks of 4% CS were found at 2960 cm^{-1} and 2880 cm^{-1} confirming the presence of $-\text{CH}_3$, and $-\text{CH}_2$ stretching whereas $\text{O}-\text{H}$ and $\text{N}-\text{H}$ stretching overlapped at 3420 cm^{-1} . Moreover, stretching vibration at 1658 cm^{-1} confirmed the presence of $\text{C}=\text{O}$ whereas $\text{N}-\text{H}$ bending was observed at 1539 cm^{-1} . The $\text{C}-\text{O}$ stretching for the primary and secondary hydroxyl group was obtained at 1030 cm^{-1} and 1085 cm^{-1} , respectively [44]. Fig. 6C demonstrates the FTIR spectra of PSS wherein $\text{C}-\text{H}$ stretching was obtained at 2921 cm^{-1} . In addition, benzene ring in-plane bending and skeleton vibration were obtained at 1010 cm^{-1} and 1140 cm^{-1} . The intense peak at 1065 cm^{-1} confirmed the presence of sulphonate (SO_3) functionality. In the

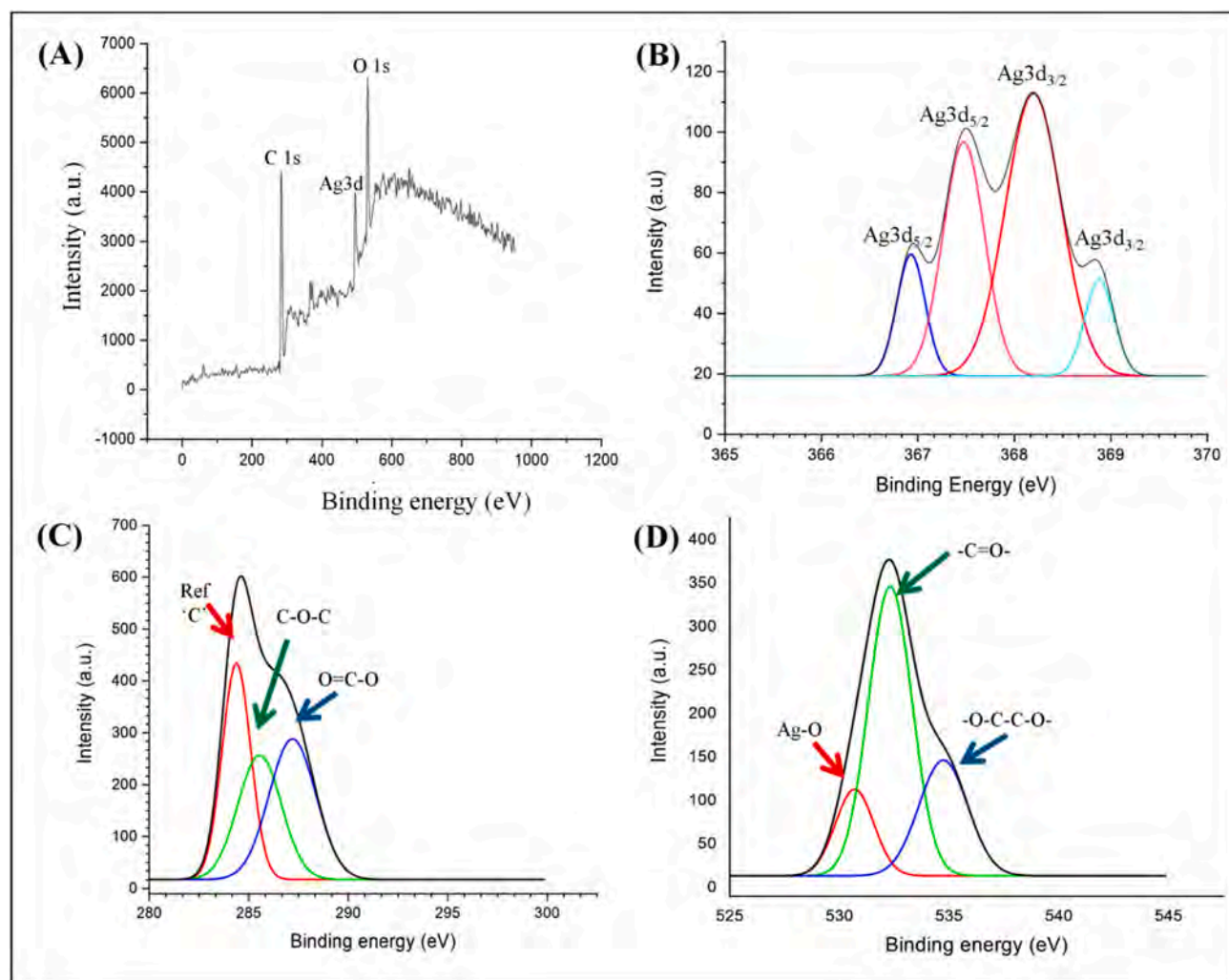


Fig. 5. XPS spectra of AgNPs (A) survey spectrum; (B) Ag 3d; (C) C 1s and (D) O 1s.

case of the LbL approach, these abovementioned functional groups were retained in LbL assembly. The formation of the CH layer on the AgNPs surface alters the wavelength whereas it masks the functional groups. Therefore, it resulted in a change in peak intensity. The existence of C—O stretching for the primary O—H and secondary O—H was obtained at 1032 cm^{-1} and 1078 cm^{-1} , respectively. Similarly, deposition of PSS on AgNPs-CH resulted in changes in peak intensity wherein an intense peak at 1068 cm^{-1} confirmed the presence of SO_3 functionality. The FTIR spectra of the final assembly of AgNPs-CH-PSS-CH illustrate the broad peak for -OH, -NH whereas the intense peak for C=O, C—O, and - SO_3 assured the successful development of LbL assembly on the surface of green synthesized AgNPs using CS and PSS.

For further confirmation, HRTEM was employed to observe the surface morphology of AgNPs and LbL assembly including AgNPs-CS, AgNPs-CS-PSS, and AgNPs-CS-PSS-CS. Fig. 7 (A, i, ii, and iii) HRTEM images of green synthesized AgNPs showed the smooth and spherical surface morphology with particle sizes ranging from 14.2 nm to 25.15 nm (Average diameter: 18.22 nm). Fig. 7B (i, ii, and iii) demonstrates the coating of CH on the surface of AgNPs which resulted in the noticeable changes in the surface morphology of AgNPs. Herein, the rough and coarse surface morphology was found after the initial coating of CH. In addition, the average diameter of AgNPs-CH was found to be 29.02 nm. Fig. 7C (i, ii, and iii) depicts the morphology of AgNPs-CH-PSS. In this case, deposition of the second layer of PSS on the surface of AgNPs-CH resulted in noticeable changes as compared to the previous layer of CH. The non-uniform and rough texture has existed after the coating of

PSS offers proof of the formation of the anionic polymeric layer. Herein, the AgNPs-CH-PSS particle size range was found to be 24.12 nm to 40.01 nm (Average diameter: 33.85 nm). The final layer of CH on the surface of AgNPs-CH-PSS-CH has exhibited the formation of an analogous surface morphology with AgNPs-CH that provides the evidence for the formation of the third layer of CH on the surface of AgNPs-CH-PSS (Fig. 7D (i, ii, and iii)). In this assembly, the particle size range was found to be 35.08 nm to 69.12 nm whereas the average diameter was found to be 48.84 nm. Overall, HRTEM images confirmed the development of polyelectrolyte (cationic and anionic polymers) layers on the surface of green synthesized AgNPs.

3.4. Detection of $\text{A}\beta_{1-42}$ using $\text{GO@AgNPs-anti-A}\beta$ SPR

In this step, the design of high sensitive $\text{GO@AgNPs-Anti-A}\beta$ SPR biosensor was reported using GO, and LbL assembly of AgNPs-CS-PSS-CS. The immobilization of anti-A β antibodies on the surface of LbL assembly (AgNPs-CS-PSS-CS) was achieved by mixing AgNPs-CS-PSS-CS and monoclonal anti-A β antibodies via physical adsorption. It develops the bonding among amino groups of AgNPs-CS-PSS-CS containing CS and carboxyl group of anti-A β antibody that resulted in AgNPs-CS-PSS-CS@ anti-A β conjugates. The zeta potential of AgNPs-CS-PSS-CS@ anti-A β conjugate was found to be +29.01 mV confirming the immobilization of antibody on the surface of AgNPs-CS-PSS-CS. After that, the immobilization of GO nanosheet on the surface of amine-modified 'Au' coated SPR sensor chip was achieved by EDC/NHS

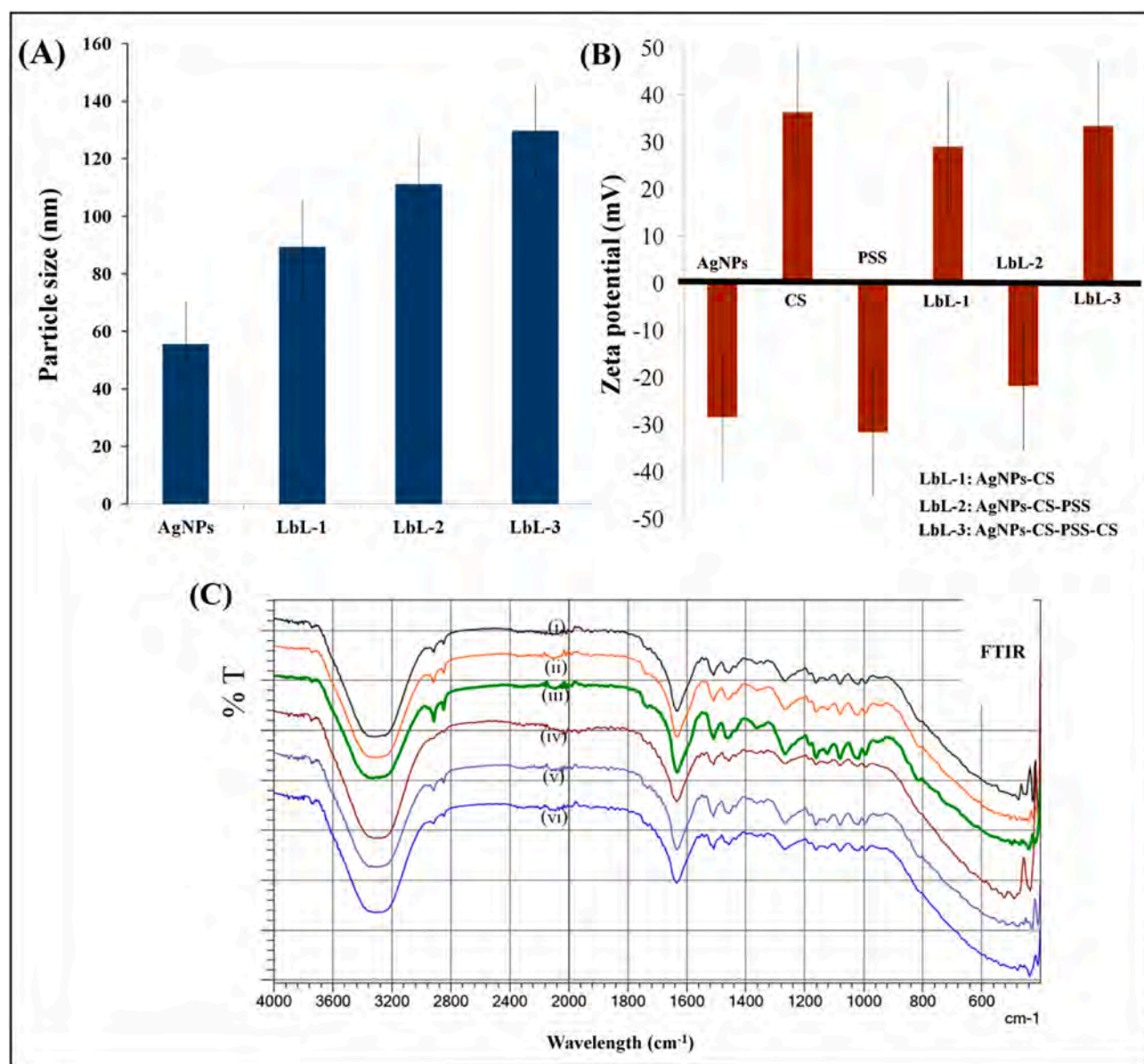


Fig. 6. (A) Particle size of LbL assembly ($n = 3$); (B) Zeta potential of AgNPs-CS-PSS-CS assembly ($n = 3$); (C) FTIR spectra of green synthesized AgNPs (i), CS (ii), PSS (iii), AgNPs-CS (iv), AgNPs-CS-PSS (v), and AgNPs-CS-PSS-CS (vi). (For interpretation of the references to colour in this figure legend, the reader is referred to the web version of this article.)

chemistry using EDC/NHS wherein C-terminal carboxylic functional groups were activated and then condensed with a surface group of the sensor chip. The addition of BSA after immobilization of antibody AgNPs-CS-PSS-CS@anti-A β conjugates offers the blocking of a free surface group on the GO nanosheet. As depicted in Fig. 8A and B, the signal of the SPR biosensor enhanced as the concentration of A β_{1-42} peptide raised from 2 fg/mL to 400 ng/mL. In this, SPR signal response and logarithmic value of 'A β_{1-42} ' peptide concentration exhibited the linear relationship wherein regression equation was found to be $Y = 30.64 \log A\beta \text{ (fg)} + 13.38$ and regression coefficient (R^2) was found to be 0.9833 (Fig. 8C). In the case of the regression equation, 'Y' depicts the response from the SPR biosensor and 'C' indicates the concentration of A β . Moreover, the limit of detection (LOD) was calculated using the equation of $3SD/\text{slope}$ (SD: standard deviation, $n = 3$). As a result, the LOD was found to be 1.21 ± 0.08 fg/mL. Herein, it confirmed that the application of GO and LbL assembly in GO@AgNPs-Anti-A β SPR boosted the sensitivity towards the A β peptide. Furthermore, it provides a wide linear range that may be because of the combined approach of non-

plasmon GO, plasmonic AgNPs, LbL assembly, and affinity bio-receptors in SPR biosensors. Primarily, when GO is used as a carrier for immobilization and it is advantageous to develop maximal antibody conjugation. Surprisingly, the edge of the GO nanosheet is coarse and has a lot of oxygen functionality, thus it has a greater surface area and a better immobilization ability. The assembly of GO nanosheets on the surface-modified 'Au' layer of a sensor chip demonstrated good stability after washing with PBS buffer and other solvents, as evidenced by a small change in the system's resonant angle. The dense AgNPs modified by polyelectrolyte (LbL assembly) offer a fresh platform with plentiful binding sites and oriented anti-A β immobilization. For sense, an exceptional bioconjugate strategy was preferred for sensing of A β peptide wherein AgNPs-CS-PSS-CS@ anti-A β conjugate enlarges the mass transferred on the sensing chip surface. It helps to boost the refractive index of the fabricated sensing chip and consequently, it furnishes an amplified response signals. In addition, 'Au' coating and high mass density AgNPs-CS-PSS-CS@ anti-A β conjugate resulted in electromagnetic coupling. It offers to boost final SPR response signals that are

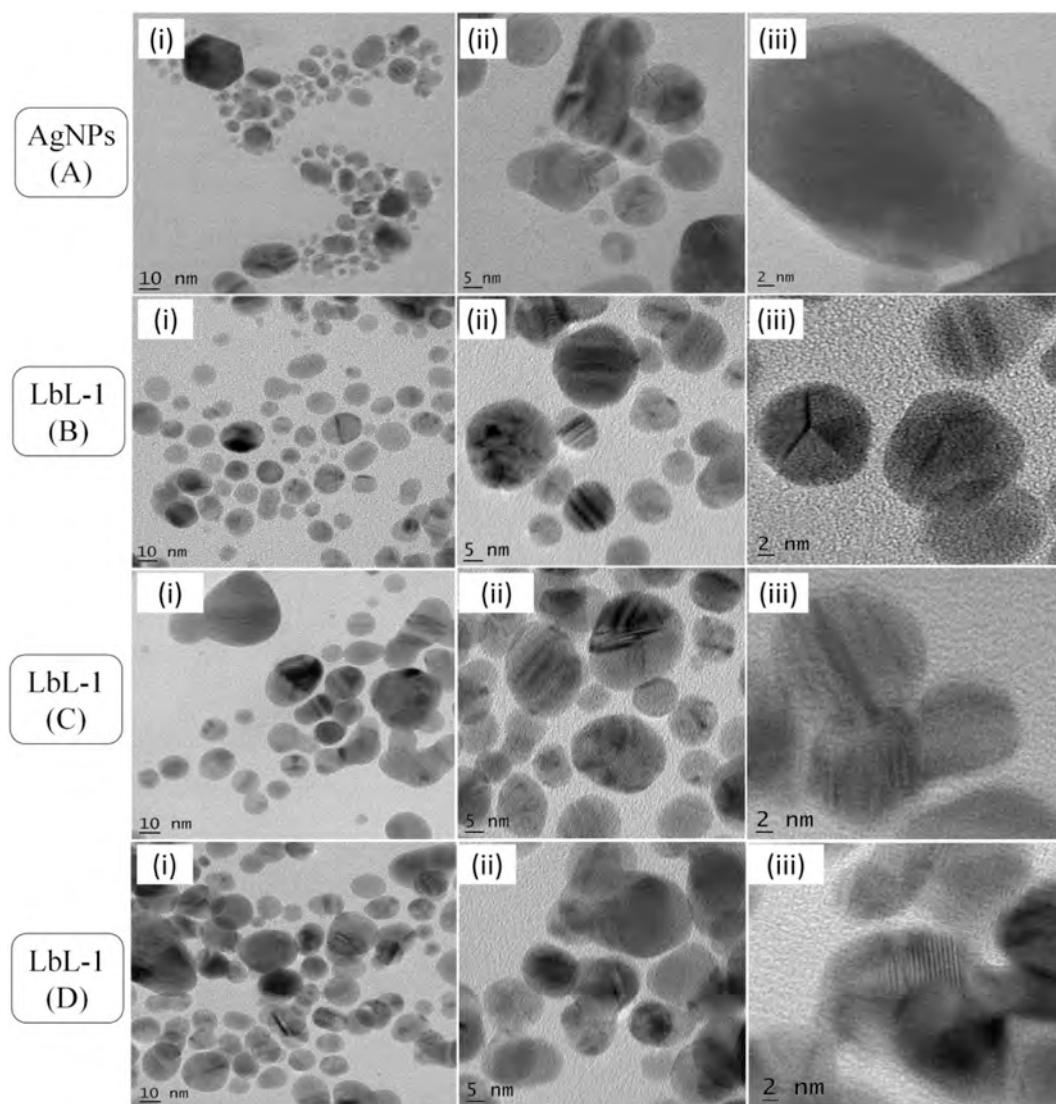


Fig. 7. HRTEM images of green synthesized AgNPs (A: i, ii, and iii); AgNPs-CS (B: i, ii, and iii), AgNPs-CS-PSS (C: i, ii, and iii), and AgNPs-CS-PSS-CS (D: i, ii, and iii). (For interpretation of the references to colour in this figure legend, the reader is referred to the web version of this article.)

generated from the dielectric alteration of the metal carrier after the formation of A β peptide-anti A β conjugate. Therefore, the concentration of AgNPs-CS-PSS-CS@ anti-A β conjugate is playing an imperative role in sensitivity enhancement. The concentration of LbL assembly was tuned in this study, wherein raising the concentration of AgNPs-CS-PSS-CS@ anti-A conjugate to 25 $\mu\text{g/mL}$ yields rising redshifts that are proven by resonant angle. As concentration increased, there was a substantial deposition of bioconjugate, resulting in a change in resonant angle (blue shift). Therefore, 25 $\mu\text{g/mL}$ (saturation concentration) of a developed bioconjugate was preferred as a signal enhanced in biosensing of A β peptide. Overall, the synergistic performance of sensor components improves the sensitivity of the SPR biosensor. To assured superior performance, the different SPR-based biosensor for the identification of A β antigen is depicted in Table 1. Finally, the analysis of A β peptide in AD-induced animal blood, saliva, and CSF was accomplished using the GO@AgNPs-Anti-A β SPR biosensor. At 0 days, there was no SPR signal response for samples of healthy animals' blood and saliva samples. At 18 days after injection of STZ, the collected blood, saliva, and CSF samples were showed 27.75 pg/mL, 8.20 fg/mL, and 89.44 pg/mL of the presence of 'A β ' peptide, respectively. For 21 days, blood, saliva, and CSF samples were examined using the completion of the GO@AgNPs-Anti-A β SPR biosensor that demonstrated the significant enhancement in the SPR

response unit. Herein, the CSF of AD-induced animals displayed the maximum concentration of A β peptide (130.02 pg/mL) as compared to the blood (56.17 pg/mL) and saliva (69.80 fg/mL). Hence, the A β peptide identification in AD-induced animal body fluids using the GO@AgNPs-Anti-A β SPR biosensor confirmed the real-time applicability of the SPR biosensor for the diagnosis of AD. Table 1 demonstrates the comparison of the presentation of GO@AgNPs-Anti-A β SPR biosensor and different sensor performances for detection of A β_{1-42} antigen.

3.5. Anti-interference study and other analysis parameters

The selectivity of the GO@AgNPs-Anti-A β SPR biosensors towards A β_{1-42} peptide was measured by injecting 40 ng/mL of each interfering molecule such as proteins, enzymes metal ions, etc. The relative responses of A β_{1-42} peptide and other molecules over the GO@AgNPs-Anti-A β SPR biosensors surface were measured as a response unit. As a result, the analysis confirmed that the responses assessed for A β at 40 ng/mL concentrations were obtained larger as compared to the responses obtained for selected interfering substances (Fig. 8D). Interestingly, owing to affinity biotransducer (Anti-A β antibody), the GO@AgNPs-Anti-A β SPR biosensors furnishes the high selectivity

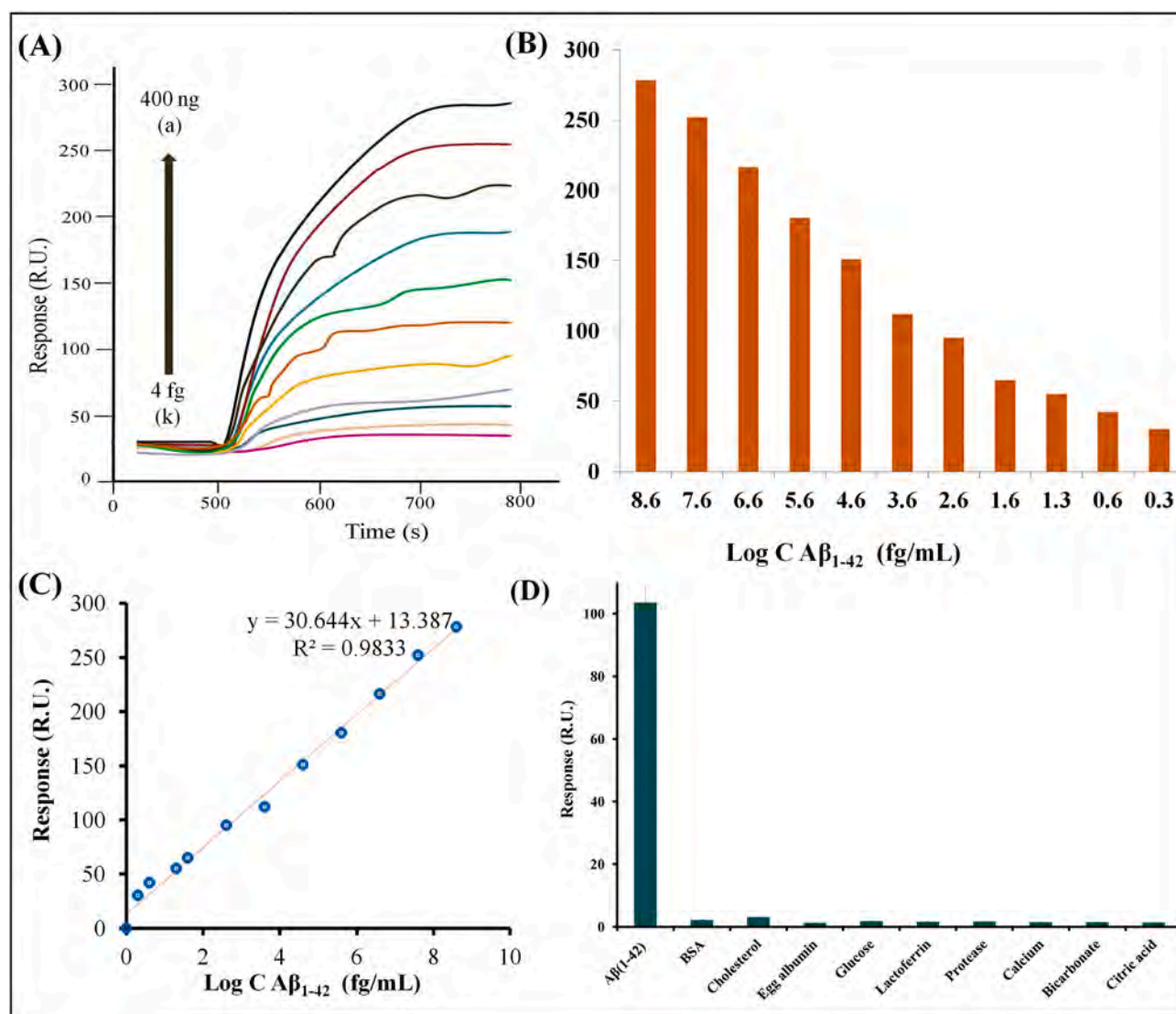


Fig. 8. (A) Overlay of SPR sensograms and bar chart (B) responses showing interaction of different concentrations of Aβ₁₋₄₂ such as 400 ng/mL, 40 ng/mL, 4 ng/mL, 400 pg/mL, 40 pg/mL, 4 pg/mL, 400 fg/mL, 40 fg/mL, 20 fg/mL, 4 fg/mL, 2 fg/mL (a to k) with immobilized with (C) Linear relationship between SPR biosensor signal (Response) to logarithmic Aβ₁₋₄₂ concentration.(D) Selective detection of Aβ₁₋₄₂ in presence of BSA, cholesterol, egg albumin, glucose, lactoferrin, protease, calcium, biocarbonate, and citric acid.

Table 1

Comparison of the performance of GO@AgNPs-Anti-Aβ SPR biosensor for detection of Aβ₁₋₄₂.

Sr. No.	Biosensor	Aβ peptide	Linear range	LOD	Ref
1.	Affinity- Au coated BK7 SPR	Aβ ₁₋₄₂	0.02 nM to 1 nM	0.31 nM	[45]
2.	Affinity- carboxymethylated CM5 chips SPR	Aβ ₄₀ fibrils	33 nM to 200 nM	1.5 nM	[19]
3.	Affinity-waveguide-coupled bimetallic SPR	Aβ ₄₂	100 pg/mL – 1000 pg/mL	500 pg/mL	[46]
4.	Affinity based bimetallic (Au:Ag) SPR	Aβ ₁₋₄₂	250 pg/mL to 1000 pg/mL	54.569 pg/mL	[12]
5.	GO@AgNPs-Anti-Aβ	Aβ ₁₋₄₂	2 fg/mL to 400 ng/mL	1.21 fg/mL	This work

Table 2

Results for Aβ₁₋₄₂ measurement in collected saliva and blood samples by GO@AgNPs-Anti-Aβ SPR biosensor.

Sr. No.	Real-time sample	The spiked concentration of Aβ ₁₋₄₂ (ng/mL)	The measured concentration of Aβ ₁₋₄₂ (ng/mL)	Percent recovery of Aβ ₁₋₄₂	Percent relative standard deviation (% RSD)
1.	Saliva	40	37.18 ± 0.56	92.95	5.78
2.	Blood	40	39.40 ± 0.43	98.50	1.69

towards the Aβ₁₋₄₂ in the presence of other interfering agents. The real-time analysis of Aβ₁₋₄₂ in saliva and blood samples shows negligible interference by saliva and blood compositions. The percentage recovery of Aβ₁₋₄₂ shows 92.95% and 98.50% recovery in saliva and blood samples, respectively. The % RSD was found to be 5.78 and 1.69 for spiked Aβ₁₋₄₂ in saliva and blood samples, respectively (Table 2). Therefore, it confirmed that the GO@AgNPs-Anti-Aβ SPR biosensor can be preferred to recognize Aβ₁₋₄₂ from real-time samples. Other important features mainly stability and reproducibility of the proposed

GO@AgNPs-Anti-A β SPR biosensor were measured. As a result, the percent RSD was 1.85% (<5%) showing that the GO@AgNPs-Anti-A SPR biosensor has good reproducibility. In case of stability of GO@AgNPs-Anti-A SPR biosensor, % RSD was found to be 2.32%. It indicates the acceptable stability of the GO@AgNPs-Anti-A β SPR biosensor. In conclusion, the fabricated GO@AgNPs-Anti-A β SPR biosensor exhibited good stability, reproducibility, high selectivity and real-time applicability.

(n = 3)

4. Conclusion

To date, the modification of the 'Au' layer with an amine group, GO nanosheet, and AgNPs-CS-PSS-CS for 'A β _{1–42}' peptide detection utilizing GO@AgNPs-Anti-A β SPR biosensor still has not been implemented. Therefore, this work demonstrates the surface decorated AgNPs-CS-PSS-CS assembly-based affinity SPR biosensor for highly sensitive recognition of AD biomarker A β _{1–42} using GO nanosheet as an advanced non-plasmonic nanomaterial. Interestingly, the utilization of AgNPs-CS-PSS-CS assembly furnishes the high selectivity and sensitivity assured by sensorgram. The utilization of CS as an external layer of LbL assembly furnishes the amino groups that offer the plentiful sites for immobilization of anti-A β antibodies with specific directions. The application of GO nanosheet forms the bonding with NH₂ group on 'Au' coated sensor chip via carbodiimide chemistry. Mainly, it offers a high surface area for immobilization of Anti-A β antibodies on the surface of the GO nanosheet. Moreover, owing to their optical properties, they help to heighten the overall presentation of GO@AgNPs-Anti-A β SPR biosensors in terms of sensitivity and selectivity. It is worthy to divulge that the combined approach of AgNPs, GO, and LbL assembly resulted in the lowest detection limit of about 1.21 fg/mL and a good linear range from 2 fg/mL to 400 ng/mL. Moreover, it provides the speedy identification of A β _{1–42} peptides without any influence on detection ability, and also it requires a small volume of samples. The anti-interference study and real-time analysis in AD-induced animals confirmed the applicability of the sensor as well as selectivity towards the A β _{1–42} in CSF, blood, and saliva. Moreover, the good stability and reproducibility of GO@AgNPs-Anti-A β SPR biosensors make them an exceptional candidate for practical biosensing applications. Herein, the application of CS as coating materials for plasmon materials coating in SPR biosensors will open a new preference for the recognition of disease biomarkers. In winding up, this high-throughput SPR centered GO@AgNPs-Anti-A β biosensor presents a reliable foundation for the early revealing of the 'A β _{1–42}' AD biomarker. In addition, it can be beneficial for the diagnosis of clinical dementia as well as Parkinson's disease dementia. In the upcoming, the actual utilization of the described SPR-assisted biosensor for the identification of A β _{1–42} in clinical samples is anticipated.

CRedit authorship contribution statement

The manuscript was written through contributions of all authors. All authors have given approval to the final version of the manuscript.

Declaration of competing interest

The authors declare that they have no known competing financial interests or personal relationships that could have appeared to influence the work reported in this paper.

Data availability

Data will be made available on request.

Acknowledgment

The authors are thankful to the Indian Council of Medical Research,

India for Research Funding (No. 5/4–5/159/Neuro/2015-NCD-I). In addition, the authors are grateful to H. R. Patel Institute of Pharmaceutical Education and Research, Shirpur and for the Sophisticated Test & Instrumentation Centre Cochin University of Science and Technology Cochin - 682 022, Kerala, India providing necessary facilities.

References

- [1] K. Hegnerová, M. Bocková, H. Vaisocherová, Z. Krístofiková, J. Říčný, D. Řípová, J. Homola, Surface plasmon resonance biosensors for detection of Alzheimer disease biomarker, *Sensors Actuators B Chem.* 139 (2009) 69–73.
- [2] K. Khachornsakul, A. Tiangtrong, A. Suwannasom, W. Sangkhroek, O. Jamjumrus, W. Dungchai, Distance-based β -amyloid protein detection on PADs for scanning and subsequent follow up of Alzheimer's disease in human urine sample, *Analyst* 147 (2022) 695–703.
- [3] D.S. Knopman, H. Amieva, R.C. Petersen, G. Chételat, D.M. Holtzman, B.T. Hyman, R.A. Nixon, D.T. Jones, Alzheimer disease, *Nat.Rev.Dis.Prim.* 7 (2021) 1–21.
- [4] M. Ameri, Z. Shabaninejad, A. Movahedpour, A. Sahebkar, S. Mohammadi, S. Hosseindost, M.S. Ebrahimi, A. Savardashtaki, M. Karimipour, H. Mirzaei, Biosensors for detection of tau protein as an Alzheimer's disease marker, *Int. J. Biol. Macromol.* 162 (2020) 1100–1108.
- [5] E.S. Musiek, S.E. Schindler, Alzheimer disease: current concepts & future directions, *Mo. Med.* 110 (2013) 395–400.
- [6] S. Nangare, P. Patil, Nanoarchitected bioconjugates and bioreceptors mediated surface plasmon resonance biosensor for in vitro diagnosis of Alzheimer's disease: development and future prospects, *Crit. Rev. Anal. Chem.* (2020) 1–31.
- [7] S.N. Nangare, P. Patil, Prevalence, distribution, treatment, and modern methods for in vitro diagnosis of Alzheimer's disease in India: challenges and future perspectives, *Thai J.Pharm.Sci.* 46 (2) (2022) 149–160. <http://www.tjps.pharm.chula.ac.th/ojs/index.php/tjps/article/view/542>.
- [8] C. Humpel, Identifying and validating biomarkers for Alzheimer's disease, *Trends Biotechnol.* 29 (2011) 26–32.
- [9] K.V. Ballman, Biomarker: predictive or prognostic? *J. Clin. Oncology: official journal of the American Society of Clinical Oncology* 33 (2015) 3968–3971.
- [10] P. Rani, S. Krishnan, C. Rani Cathrine, Study on analysis of peripheral biomarkers for Alzheimer's disease diagnosis, *Front. Neurol.* 8 (2017) 328.
- [11] R. He, X. Yan, J. Guo, Q. Xu, B. Tang, Q. Sun, Recent advances in biomarkers for Parkinson's disease, *Front. Aging Neurosci.* 305 (2018).
- [12] H.J. Kim, Y.-S. Sohn, C.-D. Kim, D.-H. Jang, Surface plasmon resonance sensing of a biomarker of Alzheimer disease in an intensity measurement mode with a bimetallic chip, *J. Korean Phys. Soc.* 69 (2016) 793–797.
- [13] J. Qin, D.G. Jo, M. Cho, Y. Lee, Monitoring of early diagnosis of Alzheimer's disease using the cellular prion protein and poly (pyrrole-2-carboxylic acid) modified electrode, *Biosens. Bioelectron.* 113 (2018) 82–87.
- [14] A. Rezabakhsh, R. Rahbarghazi, F. Fathi, Surface plasmon resonance biosensors for detection of Alzheimer's biomarkers: an effective step in early and accurate diagnosis, *Biosens. Bioelectron.* 112511 (2020).
- [15] S. Nangare, P. Patil, Black phosphorus nanostructure based highly sensitive and selective surface plasmon resonance sensor for biological and chemical sensing: a review, *Crit. Rev. Anal. Chem.* (2021) 1–26.
- [16] A.C. Murphy, M.E. Wechsler, N.A. Peppas, Recent advancements in biosensing approaches for screening and diagnostic applications, *Curr.Opin.Biomed.Eng.* 19 (2021), 100318.
- [17] S.N. Nangare, P.O. Patil, Affinity-based nanoarchitected biotransducer for sensitivity enhancement of surface plasmon resonance sensors for in vitro diagnosis: a review, *ACS Biomater.Sci.Eng.* 7 (2020) 2–30.
- [18] P.O. Patil, G.R. Pandey, A.G. Patil, V.B. Borse, P.K. Deshmukh, D.R. Patil, R. S. Tade, S.N. Nangare, Z.G. Khan, A.M. Patil, Graphene-based nanocomposites for sensitivity enhancement of surface plasmon resonance sensor for biological and chemical sensing: a review, *Biosens. Bioelectron.* 139 (2019), 111324.
- [19] M. Ramakrishnan, K.K. Kandimalla, T.M. Wengenack, K.G. Howell, J.F. Poduslo, Surface plasmon resonance binding kinetics of Alzheimer's disease amyloid β peptide-capturing and plaque-binding monoclonal antibodies, *Biochemistry* 48 (2009) 10405–10415.
- [20] H. Duan, D. Wang, Y. Li, Green chemistry for nanoparticle synthesis, *Chem. Soc. Rev.* 44 (2015) 5778–5792.
- [21] D. Sharma, S. Kanchi, K. Bisetty, Biogenic synthesis of nanoparticles: a review, *Arab. J. Chem.* 12 (2019) 3576–3600.
- [22] W. Wu, X. Yu, J. Wu, T. Wu, Y. Fan, W. Chen, M. Zhao, H. Wu, X. Li, S. Ding, Surface plasmon resonance imaging-based biosensor for multiplex and ultrasensitive detection of NSCLC-associated exosomal miRNAs using DNA programmed heterostructure of Au-on-Ag, *Biosens. Bioelectron.* 175 (2021), 112835.
- [23] R. Antiochia, P. Bollella, G. Favero, F. Mazzei, Nanotechnology-based surface plasmon resonance affinity biosensors for in vitro diagnostics, *Int.J.Anal.Chem.* 2016 (2016), <https://doi.org/10.1155/2016/2981931>.
- [24] K.S. Phillips, J.-H. Han, M. Martinez, Z. Wang, D. Carter, Q. Cheng, Nanoscale glassification of gold substrates for surface plasmon resonance analysis of protein toxins with supported lipid membranes, *Anal. Chem.* 78 (2006) 596–603.
- [25] C.M. Miyazaki, F.M. Shimizu, J. Mejia-Salazar, O.N. Oliveira Jr., M. Ferreira, Surface plasmon resonance biosensor for enzymatic detection of small analytes, *Nanotechnology* 28 (2017), 145501.

- [26] Z.A. Khan, R. Kumar, J. Dutta, Multilayer thin films of colloidal gold and silica nanoparticles: effect of polyelectrolyte coating, *Can. J. Chem. Eng.* 90 (2012) 919–924.
- [27] B.-Y. Wu, S.-H. Hou, M. Yu, X. Qin, S. Li, Q. Chen, Layer-by-layer assemblies of chitosan/multi-wall carbon nanotubes and glucose oxidase for amperometric glucose biosensor applications, *Mater. Sci. Eng. C* 29 (2009) 346–349.
- [28] S. Yan, J. Zhu, Z. Wang, J. Yin, Y. Zheng, X. Chen, Layer-by-layer assembly of poly (L-glutamic acid)/chitosan microcapsules for high loading and sustained release of 5-fluorouracil, *Eur. J. Pharm. Biopharm.* 78 (2011) 336–345.
- [29] S. Nangare, S. Landge, A. Patil, R. Tade, P. Deshmukh, P. Patil, Green synthesis of Fe-doped Ag-loaded reduced graphene oxide ternary nanocomposite for efficient photocatalytic degradation of toxic dyes, *Adv. Nat. Sci. Nanosci. Nanotechnol.* 12 (2021), 035004.
- [30] R.S. Tade, S.N. Nangare, P.O. Patil, Agro-industrial waste-mediated green synthesis of silver nanoparticles and evaluation of its antibacterial activity, *NanoBiomed. Eng.* 12 (2020) 57–66.
- [31] Y. Wang, Y. Wang, F. Wang, H. Chi, G. Zhao, Y. Zhang, T. Li, Q. Wei, Electrochemical aptasensor based on gold modified thiol graphene as sensing platform and gold-palladium modified zirconium metal-organic frameworks nanozyme as signal enhancer for ultrasensitive detection of mercury ions, *J. Colloid Interface Sci.* 606 (2022) 510–517.
- [32] N. Zhang, Y. Wang, G. Zhao, C. Wang, Y. Li, Y. Zhang, H. Wang, Q. Wei, A photoelectrochemical immunosensor based on CdS/CdTe-cosensitized SnO₂ as a platform for the ultrasensitive detection of amyloid β -protein, *Analyst* 145 (2020) 619–625.
- [33] Y. Wang, G. Zhao, G. Zhang, Y. Zhang, H. Wang, W. Cao, T. Li, Q. Wei, An electrochemical aptasensor based on gold-modified MoS₂/rGO nanocomposite and gold-palladium-modified Fe-MOFs for sensitive detection of lead ions, *Sensors Actuators B Chem.* 319 (2020), 128313.
- [34] M. Kaur, H. Kaur, D. Kukkar, Synthesis and characterization of graphene oxide using modified Hummer's method, in: *AIP Conference Proceedings* 1953, AIP Publishing LLC, 2018, p. 030180.
- [35] P.O. Patil, S.N. Nangare, P.P. Patil, A.G. Patil, D.R. Patil, R.S. Tade, A.M. Patil, P. K. Deshmukh, S.B. Bari, Fabrication of N-doped graphene@ TiO₂ nanocomposites for its adsorption and absorbing performance with facile recycling, *NanoBiomed. Eng.* 13 (2021) 179–190.
- [36] R. Chuah, S.C. Gopinath, P. Anbu, M. Salimi, A.R.W. Yaakub, T. LakshmiPriya, Synthesis and characterization of reduced graphene oxide using the aqueous extract of *Eclipta prostrata*, *3Biotech* 10 (2020) 1–10.
- [37] A. Patil, Facile one pot microbe-mediated in situ synthesis and antibacterial activity of reduced graphene oxide-silver nanocomposite, *Nanotechnology* 33 (2021), 135603.
- [38] L. Stobinski, B. Lesiak, A. Malolepszy, M. Mazurkiewicz, B. Mierzwa, J. Zemek, P. Jiricek, I. Bieloshapka, Graphene oxide and reduced graphene oxide studied by the XRD, TEM and electron spectroscopy methods, *J. Electron Spectrosc. Relat. Phenom.* 195 (2014) 145–154.
- [39] F.T. Johra, J.-W. Lee, W.-G. Jung, Facile and safe graphene preparation on solution based platform, *J. Ind. Eng. Chem.* 20 (2014) 2883–2887.
- [40] S.N. Nangare, P.O. Patil, Green synthesis of silver nanoparticles: an eco-friendly approach, *Nano Biomed. Eng.* 12 (2020) 281–296.
- [41] B. Ajitha, Y.A.K. Reddy, P.S. Reddy, Green synthesis and characterization of silver nanoparticles using *Lantana camara* leaf extract, *Mater. Sci. Eng. C* 49 (2015) 373–381.
- [42] R. Kannan, W. Stirk, J. Van Staden, Synthesis of silver nanoparticles using the seaweed *Codium capitatum* PC Silva (Chlorophyceae), *S. Afr. J. Bot.* 86 (2013) 1–4.
- [43] K.K. Bharadwaj, B. Rabha, S. Pati, B.K. Choudhury, T. Sarkar, S.K. Gogoi, N. Kakati, D. Baishya, Z.A. Kari, H.A. Edinur, Green synthesis of silver nanoparticles using *Diospyros malabarica* fruit extract and assessments of their antimicrobial, anticancer and catalytic reduction of 4-nitrophenol (4-NP), *Nanomaterials* 11 (2021) 1999.
- [44] X. Wang, R. Tang, Y. Zhang, Z. Yu, C. Qi, Preparation of a novel chitosan based biopolymer dye and application in wood dyeing, *Polymers* 8 (2016) 338.
- [45] N. Xia, L. Liu, M.G. Harrington, J. Wang, F. Zhou, Regenerable and simultaneous surface plasmon resonance detection of A β (1–40) and A β (1–42) peptides in cerebrospinal fluids with signal amplification by streptavidin conjugated to an n-terminus-specific antibody, *Anal. Chem.* 82 (2010) 10151–10157.
- [46] Y.K. Lee, K.-S. Lee, W.M. Kim, Y.-S. Sohn, Detection of amyloid- β 42 using a waveguide-coupled bimetallic surface plasmon resonance sensor chip in the intensity measurement mode, *PLoS One* 9 (2014), e98992.



Poly(allylamine) coated layer-by-layer assembly decorated 2D carbon backbone for highly sensitive and selective detection of Tau-441 using surface plasmon resonance biosensor

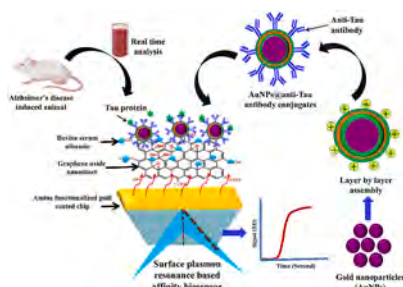
Sopan Nangare, Pravin Patil^{*}

Department of Pharmaceutical Chemistry, H. R. Patel Institute of Pharmaceutical Education and Research, Shirpur, 425405, Dhule, MS, India

HIGHLIGHTS

- The first-time layer-by-layer (LbL) approach was preferred for selective and sensitive recognition of Tau-441 antigen.
- Antibody immobilization on poly(allylamine) coated gold nanoparticles (AuNPs) LbL assembly gives affinity biotransducer.
- Graphene oxide (GO) layered surface plasmon resonance (SPR) biosensor provides detection limit up to femto-gram level.
- Spiked sample and preclinical studies assured the feasibility of GO@LbL-Au NPs-Anti-Tau SPR biosensor for Tau-441 sensing.
- Report on label-free, highly sensitive, and selective detection of Tau-441 using GO@LbL-AuNPs-Anti-Tau SPR biosensor.

GRAPHICAL ABSTRACT



ARTICLE INFO

Handling Editor: Dr. J.P. Landers

Keywords:

Tau protein
Alzheimer's disease
2D carbon backbone
Surface plasmon resonance
LbL assembly
Gold nanoparticles

ABSTRACT

The determination of clinically significant amounts of tau protein in bodily fluids is a major problem in Alzheimer's disease (AD) diagnosis. As a result, the present work aims to develop a simple, label-free, fast, highly sensitive, and selective 2D carbon backbone graphene oxide (GO) patterned surface plasmon resonance (SPR) mediated affinity biosensor for Tau-441 monitoring. Initially, non-plasmonic nanosized GO was made using a modified Hummers' method, whereas green synthesized gold nanoparticles (AuNPs) were subjected to a layer-by-layer (LbL) design employing anionic and cationic polyelectrolytes. Several spectroscopical evaluations were carried out to ensure the synthesis of GO, AuNPs, and LbL assembly. Following that, the Anti-Tau rabbit antibody was immobilized on the designed LbL assembly using carbodiimide chemistry, and various studies such as sensitivity, selectivity, stability, repeatability, spiked sample analysis, etc., were conducted using the constructed affinity GO@LbL-AuNPs-Anti-Tau SPR biosensor. As an output, it shows a broad concentration range and a very low detection limit of 150 ng/mL to 5 fg/mL and 13.25 fg/mL, respectively. The remarkable sensitivity of this SPR biosensor represents the merits of a combination of plasmonic AuNPs and a non-plasmonic GO.

^{*} Corresponding author. Department of Pharmaceutical Chemistry, H. R. Patel Institute of Pharmaceutical Education and Research, Shirpur, 425405, Dhule, MS, India.

E-mail address: rxpatilpravin@yahoo.co.in (P. Patil).

<https://doi.org/10.1016/j.aca.2023.341474>

Received 15 May 2023; Accepted 2 June 2023

Available online 3 June 2023

0003-2670/© 2023 Elsevier B.V. All rights reserved.

It also exhibits great selectivity for Tau-441 in the presence of interfering molecules, which may be because of the immobilization of the Anti-Tau rabbit on the surface of the LbL assembly. Furthermore, it ensured high stability and repeatability, while spiked sample analysis and AD-induced animal samples analysis confirmed the practicability of GO@LbL-AuNPs-Anti-Tau SPR biosensor for Tau-441 detection. In conclusion, fabricated sensitive, selective, stable, label-free, quick, simple, and minimally invasive GO@LbL-AuNPs-Anti-Tau SPR biosensor will provide an alternative for AD diagnosis in the future.

1. Introduction

Alzheimer's disease (AD) is the foremost irreversible neurological disorder on the globe [1]. In the situation of AD, neuronal destruction is continuous and irreparable [2,3], leading to a lowered conversation, high confusion, and finally, behavioral disorders that arise sequentially [3,4]. In addition, individuals ultimately lose the ability to talk, ingest, and move [2,5]. Every year, thousands of people die as a consequence of the disease's failure to be cured and the nonexistence of effective detection measures [6]. According to the studies, AD is the seventh biggest trigger of mortality in 2019 [4,7]. In 2021, a projected 6.2 million Americans aged over 65 were diagnosed with ADs, and this figure is anticipated to rise to 13.85 million in upcoming years (up to 2060) [3,4]. Moreover, ADs have gained substantial decisive highlighting from the scientific community owing to their severe influence on humans with hefty societal costs [4].

Literature assessment assured that there is currently neither a screening assay nor a technique for AD. As an effect, the diagnosis of AD rests in the jurisdiction of healthcare professionals, which could merely offer possible AD or dementia of the Alzheimer's category [8]. As an upshot, there is a desire to invent a modern tool for reliably diagnosing AD [2]. In the last couple of decades, *in vitro* disease and disorder diagnosis has garnered a great deal of interest in the biomedical area [9]. In the context of *in vitro* diagnosis, it is focused on the sensitive and selective recognition of a biomarker, which has lately been increasingly preferred for the diagnosis of critical health concerns [10,11]. Presently, a precise diagnosis of AD is extensively imperative for that rationale number of techniques have been designed [2,12]. In this, it has been stated that AD is associated with protein deposits and aggregation in the brain. Crucially, tau protein and beta-amyloid (A β) are high-flying biomarkers that have been described as hopeful molecular analytes for the prompt detection of AD [12]. As per literature, enzyme-linked immunosorbent assay (ELISA) [8], electrochemical impedance spectroscopy [13], surface-enhanced Raman spectroscopy [14], etc. have been extensively accounted for the recognition of tau protein. Based on this, a diagnosis of AD has been reported. Despite copiousness of merits, these methods are suffering from abundant disadvantages that primarily consist of poor sensitivity, low selectivity, time-consuming approach, etc. [2,12]. Regardless of remarkable progress, the impending precisely recognized tau protein in biological fluids at clinically considerable amounts remains a substantial barrier to the invention of AD diagnostic procedures [15].

Recently, the usage of surface plasmon resonance (SPR) for the recognition of tau protein has been frequently cataloged with boosted performance [16]. Despite the indisputable merits of SPR-centered biosensors, the preference for SPR-mediated biosensors suffers from numerous disadvantages that essentially contain low sensitivity and poor selectivity. Moreover, the lowest concentration of an analyte or small molecule detection is challenging via SPR-centered biosensors [17]. As an effect, such demerits of SPR biosensors can be conquered by employing tunable nanocomposites during the fabrication of biosensors [10,17]. In this shade, the employment of gold nanoparticles (AuNPs) in SPR biosensor development has been broadly claimed owing to their unique and utmost optical characteristics [18]. Moreover, the successful application of bare metal nanoparticles for the formation of bio-conjugates has been reported currently that offers a superior presentation of SPR biosensors such as specificity and sensitivity [2,10,18]. The

synthesized nanoparticles were mostly unstable and were transformed into aggregates that needed the stabilizer [19]. Overall, the minimal and heterogeneous surface chemical functional groups and stability of AuNPs influence the loading of required bioreceptors, limiting the biosensor's sensitivity and selectivity. In addition, proper immobilization with specific orientation is a critical challenge that influences biosensor performance that needs to be overcome.

In the case of a bioreceptor, stability, and functioning must be maintained. As well, strong binding between the immobilization surface and the bioreceptors, directed immobilization, a high density of bioreceptors, low nonspecific binding, and other characteristics are also highly desired in biosensor development [20]. To establish bioreceptor immobilization on the surface of metal nanoparticles, identical surface functionality on nanoparticles that can interact with the functionality contained in bioreceptors is necessary. Hence, metal nanoparticles coated with appropriate polyelectrolytes can be an excellent option for this purpose [21]. The literature revealed that antibody immobilization with suitable orientation has been providing great selectivity toward the intended analyte [10]. In this band, Layer-by-Layer (LbL) assembly has been fabricated using polyelectrolyte for a highly specific biosensor that offers immobilization of biomolecules on the surface of metal nanoparticles with proper direction and good stability [22]. In addition, it has a regulated composition, thickness, and specific surface functioning. Interestingly, the LbL assembly can provide the capability of ionic interactions that assist in the immobilization of affinity biomolecules, as well as hydrogen bonding, charge transfer, and coordination chemistry [20]. Majorly, the LbL assembly is preferred because it provides a softer attachment face on the solid's surface for direct immobilization of bioreceptors. It can also help to avoid denaturation and retain the bio-functionality of bioreceptors. Moreover, it improves surface orientation, which may boost binding affinity [23]. As well, the coating of metal nanoparticles with polyelectrolytes led to repealing, which can give higher dispersion stability to AuNPs [22]. Accordingly, the design of LbL assembly can provide the boosted presentation of biosensors in terms of overall sensitivity, selectivity, etc. which are the key factor for prompt analysis of biomarkers [22]. Importantly, because of unique qualities such as biocompatibility and surface modification ability, Poly (allylamine hydrochloride (PAH) is an amino terminated chemical (cationic nature) and Poly (sodium 4 styrene sulphonate (PSS) is an anionic compound that is commonly employed in the creation of LbL assemblies. Furthermore, the usage of PAH and PSS allows for the production of LbL assemblies based only on their electrostatic interaction. As well, the usage of PAH and PSS can provide a softer attachment surface for bioreceptor immobilization on the surface of AuNPs. Therefore, in this work, we aim to coat the exterior layer of the LbL assembly with an amine-terminated polyelectrolyte, which will give a site for the immobilization of a carboxylic terminal having antibodies in a specified direction [19,22,24].

For the last few years, it has been extensively clarified that the demand for 2D carbon notably graphene oxide (GO), has been pretty well documented for the establishment of GO-centered SPR biosensors [25]. Therefore, GO has been employed to sense several interesting biomarkers of life-threatening diseases/disorders [10]. It is because of the simplified synthesis process, affinity properties, and biocompatibility of GO. Furthermore, the adjustable mechanical, electrochemical, and optical characteristics of GO pique the interest of researchers in the invention of different sorts of biosensors. In addition, the surface

functionality of GO offers plenty of binding sites for the immobilization of antibodies [25,26]. Besides, the literature reported that the combination of GO as non-plasmonic materials with plasmonic nanoparticles (AuNPs) can boost the overall execution of the SPR biosensor [10].

To the best of our expertise, no LbL assembly-mediated GO nanocomposite decorated extremely sensitive and selective SPR biosensor for Tau-441 protein recognition has been established. As a result, we fabricated a polyelectrolyte LbL assembly-mediated GO surface decorating SPR biosensor that is extremely sensitive and selective for Tau-441. Briefly, green-produced AuNPs were implemented to assemble LbL assemblies with cationic and anionic polyelectrolyte's before being subjected to bioconjugate processing. Then, to strengthen the entire performance of the SPR biosensor, AuNPs as a plasmonic system were integrated with GO as a non-plasmonic system. In this study, the application of GO as a 2D carbon backbone was used to augment the biological specificity and sensitivity of a fabricated SPR-centered affinity biosensor. The wrapping AuNPs with polyelectrolyte primarily anionic Poly(sodium 4-styrene sulfonate) (PSS) and cationic poly(allylamine hydrochloride) (PAH) was used to promote adequate orientation for an anti-Tau rabbit monoclonal antibody that assists high selectivity. Finally, the proposed unique LbL assembly-guided GO surface-adorned SPR biosensor proved competence to recognize Tau-441 antigen with expanded entire functionality such as excellent sensitivity, admirable selectivity, quick recognition, uncomplicated and label free tracking, and so on. In the future, these customized biosensors will propose new opportunities for realistic and preliminary stage prognosis of AD using clinical samples.

2. Materials and methods

2.1. Materials

In this study, Tau-441 human (>95% SDS-PAGE, recombinant lyophilized powder, expressed in HEK 293 cells), N-hydroxysuccinimide (NHS), anti-Tau rabbit monoclonal antibody, 1-[3-(di-methylamino)-propyl]-3-ethyl carbodiimide hydrochloride (EDC), bovine serum albumin (>98%, BSA), gold (III) chloride hydrate (HAuCl_4 -aqueous, 99.995%), cationic Poly(allylamine hydrochloride) (PAH, Avg. MW: 50,000), and anionic Poly (sodium 4 styrene sulphonate) [PSS, MW: ~70,000] was procured from Sigma Aldrich, CO., St., Louis, USA. Amine-functionalized SPR biosensor chip was provided by Nicoya Life Sciences, Canada. *Colocasia esculenta* stem was collected from the Shirpur area. Graphite flakes (>99%) were provided by Asbury Carbons, New Jersey (NJ), USA as a complimentary sample for the synthesis of GO. Glycine hydrochloride (99%) was procured from Sigma-Aldrich Chemicals Pvt., Ltd. Bangalore. Streptozotocin (STZ, MW: 265.2) was obtained from EMD Millipore Corp., Billerica MA, USA. Potassium permanganate (99%, KMnO_4) was procured from Research Lab Fine Chem Industries, Mumbai, India. Nuclease-free water was provided by Invitrogen Bioservices India Private Limited Karnataka India. Sigma-Aldrich Chemicals Pvt., Ltd. Bangalore was provided isopropyl alcohol (IPA, 80 %v/v), sulfuric acid (H_2SO_4 , 95.5%), phosphoric acid (H_3PO_4 , 99.99%), hydrochloric acid (HCl), and hydrogen peroxide (H_2O_2 , 30% w/v). Double distilled water (DDW, HPLC grade) was procured from Avantor Performance Materials Pvt. Ltd., Thane West (MS), India. All chemicals were incorporated in ultrasensitive SPR biosensors for manufacturing as they were ordered from the provider.

2.2. Methods

2.2.1. Synthesis of GO nanosheets

Synthesis of GO from graphite powder was accomplished utilizing the previously described modified Hummers technique [27] supplemented by slight alterations. Initially, 54 mL: 6 mL of H_2SO_4 and H_3PO_4 were mixed slowly and then it was subjected to continuous stirring at 250 rpm using a laboratory magnetic stirrer for 15 min. After this, 450

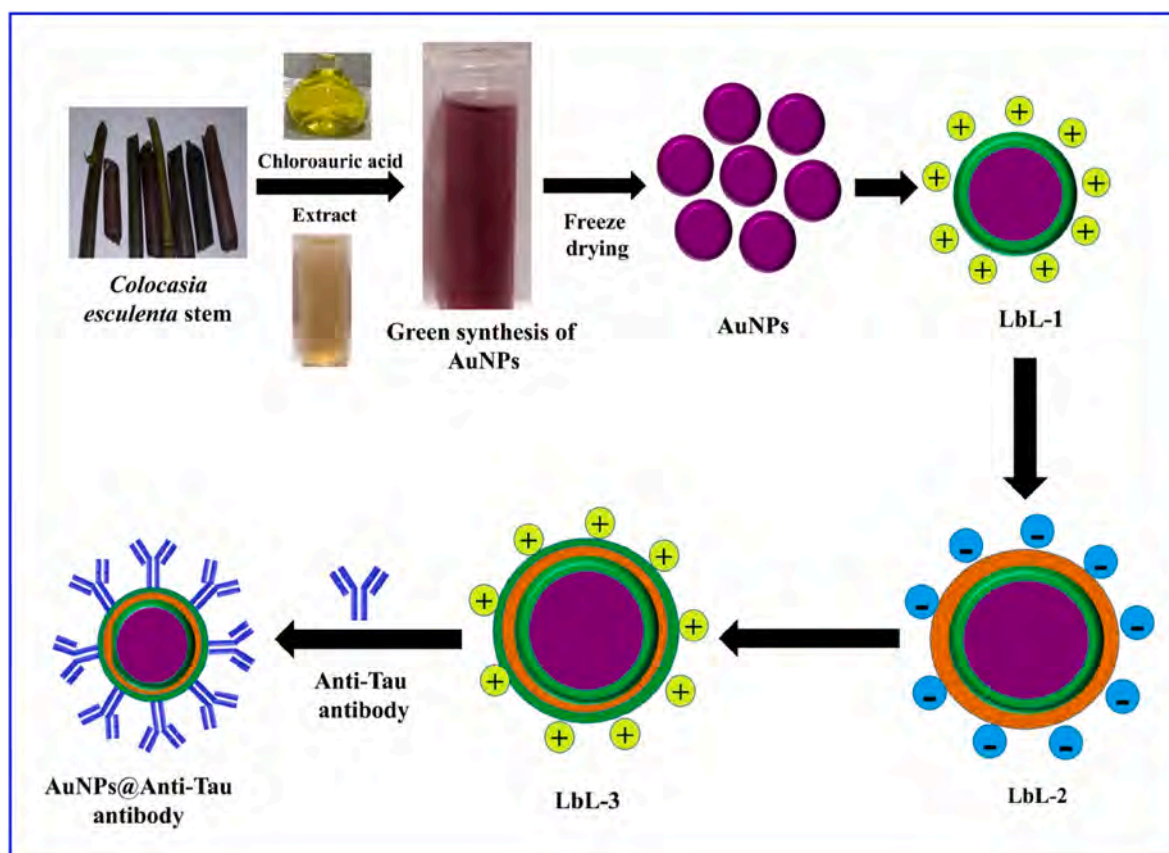
mg of nanosized graphite was mixed gradually under continuous stirring at 200 rpm. After a uniform mixture of nanosized graphite powder with acids, 2.62 g of KMnO_4 was incorporated step by step with constant stirring and then the final mixture was kept aside for 6 h for the achievement of the entire reaction. Finally, 1.35 mL of H_2O_2 was added gradually in a dark green abovementioned mixture that assists in removing the remaining KMnO_4 with homogeneous stirring for the next 10 min at room temperature to reduce the reaction temperature. The end dispersion of GO was then moved to washing using a 2:6 ratio of HCl and DDW mixture using a cold centrifugation process at 12000 rpm at 30 °C for 30 min. The same process was performed in triplicates and then the residue of GO was transferred to drying via a laboratory vacuum oven at 50 °C to the obtained complete dry product.

2.2.2. Green synthesis of AuNPs

Firstly, 100 g of *Colocasia esculenta* stem waste was collected from the shirpur local market. After that, collected stem waste was subjected to cleaning using DDW, and then it was converted into small pieces. The drying of stem pieces (0.2 mm–0.5 mm) was achieved using a laboratory hot air oven wherein the drying temperature was fixed initially at 60 °C while the temperature condition was decreased to 40 °C with 0.14 °C/min for the next 12 h. The powder of dry stems was obtained using a laboratory grinder and then the final power was sifted using a #20 sieve. For extraction, *Colocasia esculenta* stem powder (5 g) was mixed using DDW 100 mL. Then, the mixture was heated at 70 °C for 30 min to separate phytoconstituents that exist in the *Colocasia esculenta* stem. The ending extract was centrifuged (10000 rpm for 15 min) at 25 °C. Then, the clear supernatant of the extract was filtered using laboratory 0.22 μm sized membrane filters. The final filtrate was transferred to a refrigerator at 20 °C until further utilization for the synthesis of AuNPs. As a final point, one pot and facile green synthesis of AuNPs was accomplished using 7 mL of *Colocasia esculenta* and 100 mL of 5 mM of HAuCl_4 . Then, this prepared mixture was transferred to constant stirring at 500 rpm at 50 °C. In this, the reaction was monitored using Ultra-Violet (UV)-Visible (Vis) spectroscopy (Shimadzu, Japan) for up to 12 h for completion of the formation of AuNPs. The final obtained dispersion AuNPs were kept at 4 °C and then it was used for further spectroscopical characterizations. The lyophilization of green synthesized AuNPs was performed using a freeze-dryer (Freezone12, Labconco, MO, USA). Herein, the dispersion of AuNPs was transferred to pre-freezing at –30 °C for 12 h. After complete freezing, it was processed to initial primary stage drying at controlled pressure (0.016 mbar) and temperature (–53 °C) for the next 24 h. After that, the second stage of drying was accomplished at a controlled temperature (10 °C) for the next 8 h. Then, it was changed to 25 °C for 4 h along with a constant augment in programmed temperature at 1 °C/min. To end, the cold trap temperature was monitored at –53 °C, which assist to attain the freeze-drying process. The lyophilized AuNPs powder was then utilized for subsequent characterizations and fabrication of LbL assembly.

2.2.3. Characterization of GO and AuNPs

The synthesized GO and green synthesized AuNPs were characterized using a variety of spectroscopic techniques. Initially, the Ultra-violet-Visible (UV-Vis) Spectrum of obtained GO and AuNPs was recorded between 800 nm and 200 nm by laboratory UV 1800 Spectrophotometer (Shimadzu, Japan) using a quartz cuvette (1 cm). The surface functionality present in GO and AuNPs was assured using Fourier Transform Infrared Spectroscopy (FT-IR), Thermo Nicolet, Avatar 370). The resolution of 4 cm^{-1} with frequencies ranging from 400 to 4000 cm^{-1} was maintained for all FT-IR analyses. The particle size, polydispersity index (PDI), and zeta potential analysis of obtained GO and AuNPs were calculated using Nanoplus 3 (Micromeritics, USA). Following that, scanning electron microscopy (SEM, JEOL Model JSM - 6390LV) was employed to characterize the morphology of the GO and AuNPs. The elemental composition of GO and AuNPs was accomplished using energy dispersive spectroscopy on a FESEM/EDAX (OXFORD XMX



Scheme 1. Design of PAH and PSS polyelectrolyte-based nanosize LbL assembly on the surface of AuNPs followed by fabrication of AuNPs-PAH-PSS-PAH@-Anti-Tau conjugate.

N, Accelerating voltage: 15 kV). As well, HR-TEM (Jeol/JEM 2100, Source: LaB6) with a 200 kV accelerating voltage was used to study morphology, size, and selected area electron diffraction pattern (SAED) of the GO and AuNPs. The surface binding energies were then analyzed using X-ray photoelectron spectroscopy (XPS) using a high-performance 0–5 keV Ar^+ ion cannon (physical electronics, IIT Roorkee, India). A diffractogram of synthesized GO and AuNPs was recorded using Powder X-ray diffraction (PXRD) spectroscopy on a Bruker D8 development (STIC Cochin, India). Raman spectrum GO was performed with a Horiba (HR800-UV) confocal micro-Raman spectrometer at 532 nm laser power of 50 mW at room temperature.

2.3. Design of GO@AuNPs-Anti-Tau SPR biosensor

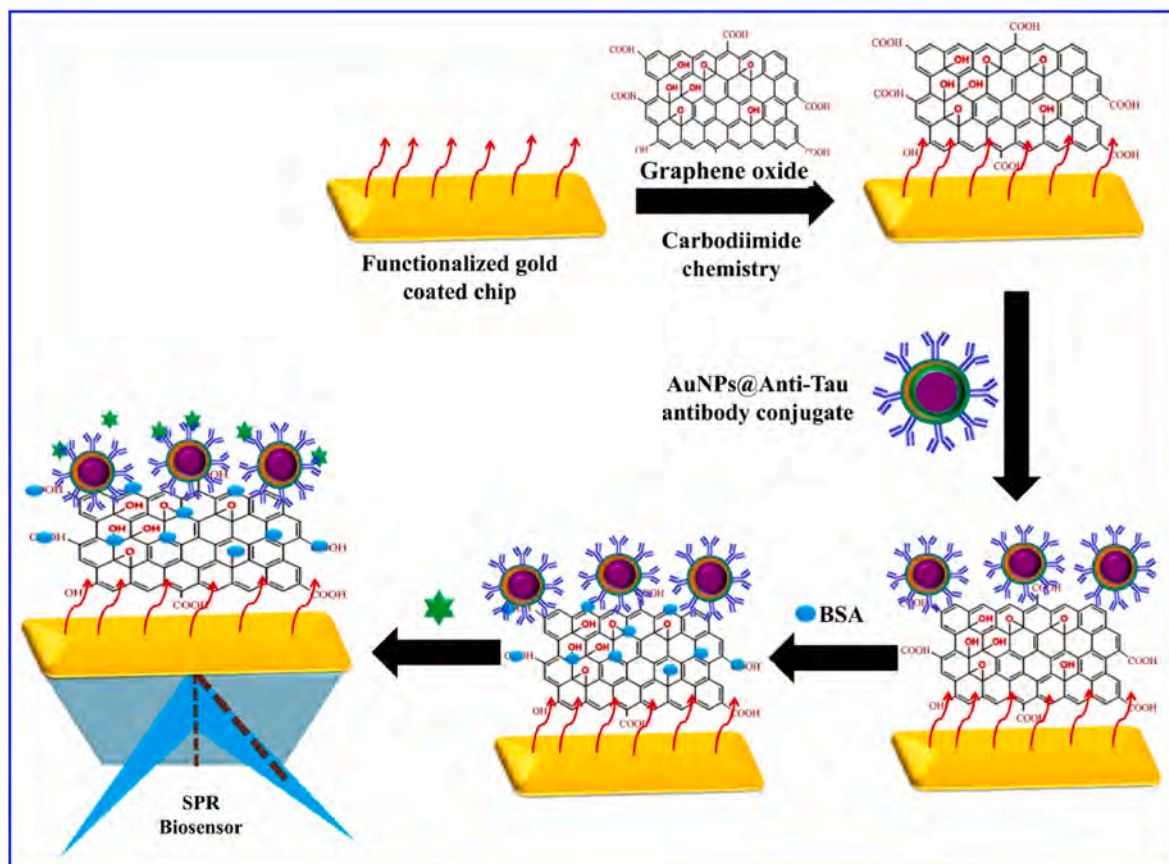
2.3.1. Design of polyelectrolyte-based LbL assembly

Despite the numerous benefits of AuNPs, their aggregation has a negative influence on the performance of SPR-based biosensors. It can be overcome by utilizing an LbL assembly, in which the charge on the exterior layer can help to repel the AuNPs and retain the stability in the solvent system [19]. In this work, we intend to develop the LbL assembly using PAH (cationic) and PSS (anionic) polyelectrolytes on the face of AuNPs, wherein the external layer of PAH in LbL presents the homogeneous huge amine functionality. Importantly, it can provide the particular orientation, strong bonding, and maximum site for immobilization of carboxylic terminal containing Anti-Tau rabbit monoclonal antibody. As a result, it can contribute to the high sensitivity and selectivity towards analyte. Furthermore, the employment of PAH and PSS allows for the production of LbL assemblies based on electrostatic forces with no major modifications. In this step, accurately 200 mg of lyophilized AuNPs was incorporated into 50 mL of deionized (DI) water. Next, 5 mL of 1% (w/v) cationic PAH polyelectrolyte was added into

AuNPs dispersion for initial coating (AuNPs-PAH) and then transferred to sonication for 30 min. Then, obtained AuNPs-PAH assembly was separated at 25000 rpm for 30 min at 25 °C and then it was washed with deionized water to eliminate the free form of PAH. The final obtained residue of AuNPs-PAH assembly was then processed for freeze-drying by preferring the abovementioned procedure. For the second anionic layer, 1% PSS was prepared in a 10 mL volumetric flask using deionized water. Next, 150 mg of AuNPs-PAH was mixed with 10 mL of PSS solution with 10 min sonication at 25 °C and then ultra-cold centrifugation at 25000 rpm for 30 min at 20 °C. The separated supernatant was then discarded and remained a residue of AuNPs-PAH-PSS was washed twice using deionized water to remove unbounded PSS from the LbL assembly. Herein, the drying of the second AuNPs-PAH-PSS assembly was performed using a laboratory freeze dryer. Finally, the third layer of cationic PAH on the exterior of dried AuNPs-PAH-PSS-PAH assembly was prepared using 1% (w/v) PAH on the surface of AuNPs-PAH-PSS followed by the same procedure of initial PAH coating. At last, the final AuNPs-PAH-PSS-PAH assembly was dried using a freeze dryer and further used for characterizations. After each layer of AuNPs-PAH-PSS-PAH assembly, zeta potential, particle size, FTIR, etc., were performed to assure the fabrication of LbL assembly on the exterior of obtained AuNPs by PAH and PSS. Scheme 1 represents a synthesis of LbL assembly using polyelectrolyte and green synthesized AuNPs.

2.3.2. Design of AuNPs-PAH-PSS-PAH@-Anti-Tau nanoconjugate

The preference of LbL assembly to design bioconjugate can provide a softer attachment surface for Anti-Tau rabbit monoclonal antibody immobilization on the face AuNPs. Therefore, it can aid in avoiding the denaturation of bioreceptors and other biomolecules such as BSA, Tau-441, lactoferrin, etc. As a result, the LbL assembly assists in preserving the functionality of the bioreceptors, which can result in superior SPR



Scheme 2. Presentation of fabrication of affinity-based highly sensitive and selective GO@LbL-AuNPs-Anti-Tau SPR biosensor and their application for biosensing of Tau-441 antigen.

biosensor operation in terms of responsiveness and selectivity. In brief, the design of AuNPs-PAH-PSS-PAH@-Anti-Tau conjugate was engineered using AuNPs-PAH-PSS-PAH and Anti-Tau rabbit monoclonal antibody (Scheme 1). Briefly, 10 mg of AuNPs-PAH-PSS-PAH was added into 100 mL of nuclease-free water at 20 °C followed by bath sonication for 3 min to remove air bubbles from dispersion. Then, 25 μ L of anti-Tau rabbit monoclonal antibody (50 μ g/mL) in pH 7.4 phosphate buffer saline (PBS) was incorporated to immobilize on the surface of fabricated LbL assembly at 15 °C through active loading owing to interaction among the amine group of PAH and carboxylic functionality of antibody (carbodiimide chemistry). Herein, the carboxylic functionality of the Anti-Tau rabbit monoclonal antibody was activated by 100 μ L of 0.4 mM EDC/0.1 mM NHS (1:1) and then attached to the amine (NH_2) exterior moiety of PAH that was outside the cationic layer of AuNPs-PAH-PSS-PAH LbL assembly. For immobilization of activated Anti-Tau rabbit monoclonal antibody on the surface of AuNPs-PAH-PSS-PAH LbL, the obtained mixture was incubated 30 min at 15 °C. At this, the surface potential plus particle size of AuNPs-PAH-PSS-PAH@-Anti-Tau conjugate was verified using a particle size analyzer. Finally, prepared AuNPs-PAH-PSS-PAH@-Anti-Tau conjugate was further utilized for sensing of Tau 441 antigen.

2.4. Experimental setup

An experimental setup of GO@LbL-AuNPs-Anti-Tau SPR biosensor (LbL-AuNPs: AuNPs-PAH-PSS-PAH@-Anti-Tau conjugate) was prepared using amine-functionalized gold (Au)-coated glass slide (Au: 50 nm thickness), GO nanosheets, and AuNPs-PAH-PSS-PAH@-Anti-Tau conjugate. At first, the amine (NH_2)-modified gold-coated sensor chip was incorporated into laboratory semiautomated OpenSPR (Nicoya Life-sciences, Canada). After this, the outside of the NH_2 functionalized

surface of the sensor chip was cleaned with 150 μ L of pH 7.4 PBS and DI nuclease-free water in triplicates. In addition, the sample channel of OpenSPR was cleaned by injecting 200 μ L of IPA via the sample port for the removal of air bubbles from the channel. Simultaneously, GO nanosheets (100, 200, 300, 400, and 600 μ g/mL) were dispersed in nuclease-free water. Here, a 1:1 ratio of 0.4 mM EDC/0.1 mM NHS (100 μ L) was used to activate GO-containing carboxylic functionality. The activated 150 μ L of GO dispersion was then injected through a sample port (flow rate: 15 μ L/min). After 600 s, the biosensor surface was washed twice with 150 μ L of PBS to remove any leftover EDC/NHS and GO sheets from the channel port and biosensor surface. After optimization of GO concentration, this procedure was repeated to ensure that the GO nanosheets were completely immobilized on the amine-functionalized sites present on the chip surface of the SPR sensor. Here, carbodiimide chemistry was used to adhere the nanosheets to an amine-modified biosensor surface. After next, dispersion of AuNPs-PAH-PSS-PAH@-Anti-Tau conjugate (10, 15, 20, 25, and 30 μ g/mL) was injected (Flow rate: 10 μ L/min). It was immobilized on the surface of activated GO-containing activated surface that offers the covalent association among antibody-containing amine functional groups and nanosized GO-containing carboxyl groups. After 400 s, the biosensor surface was washed twice with 150 μ L of PBS to remove any leftover AuNPs-PAH-PSS-PAH@-Anti-Tau conjugate from the activated GO nanosheet surface and channel port. After this optimization, masking of a free surface group of activated GO was accomplished through masking agent BSA (flow rate: 10 μ L/min, concentrations: 50, 100, 150, 200, and 250 μ g/mL in nuclease-free water). After that washing was performed using 150 μ L of PBS twice to remove any leftover BSA from the activated GO nanosheet surface and channel port. Finally, a similar process was repeated using optimized BSA concentration to confirm the complete masking of the activated free surface group of immobilized GO

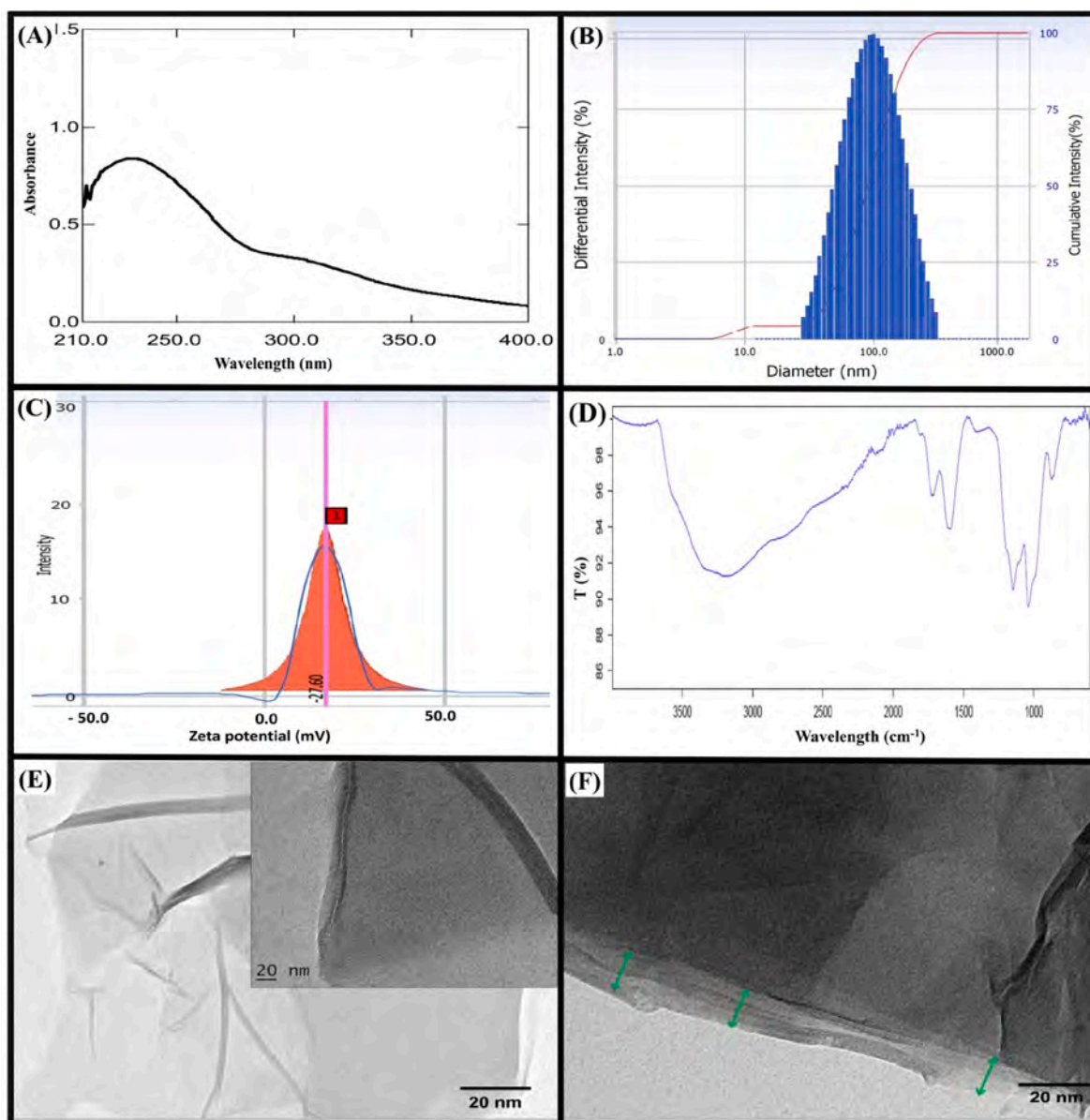


Fig. 1. (A) UV Vis spectrum of prepared GO dispersion from graphite flakes; (B) Particle size analysis of GO; (C) Zeta potential of GO; (D) FTIR spectrum of GO; (E and F) HR-TEM images of GO.

nanosheets on the surface of the SPR biosensor. As a result, the masking using BSA prohibits the interaction with different interfering substances that existed in analytical samples.

2.5. Biosensing of Tau-441 antigen

Biosensing of Tau-441 antigen was achieved using the anticipated GO@LbL-AuNPs-Anti-Tau SPR biosensor (Scheme 2). In brief, the stock concentration of Tau-441 antigen (0.5 $\mu\text{g/mL}$) was prepared using pH 7.4 PBS at 20 $^{\circ}\text{C}$, and then a diverse range of concentrations was prepared from 150 ng/mL to 5 fg/mL (Final volume: 5000 μL) using freshly prepared PBS (pH 7.4). Biosensing of Tau-441 antigen was achieved by injecting 50 μL of lower concentration using a syringe via sample port (flow rate: 10 $\mu\text{L/min}$) and waiting for 120 s to complete the binding of Tau-441 and Anti-Tau rabbit monoclonal antibody. Then, pH 1.2-glycine hydrochloride was preferred as a cleaning agent (or regenerating agent) to remove bound Tau-441 antigen from the surface of the Anti-Tau rabbit monoclonal antibody. Similarly, the remaining concentrations of Tau-441 antigen were injected to validate the wide linear

concentration range using the anticipated affinity GO@LbL-AuNPs-Anti-Tau SPR biosensor. Finally, the limit of detection (LOD: $3.3 \times \text{standard deviation (SD) / Slope}$) was assessed using an obtained slope from the calibration curve of Tau-441 antigens and the SD of their SPR responses. Overall, the designed GO@LbL-AuNPs-Anti-Tau SPR biosensor was validated for the capability to sense a low concentration of Tau-441 antigen as an AD biomarker through a shift of the SPR reflectance curve.

2.6. Selectivity, stability, and reproducibility analysis

Selectivity analysis is an essential element in biosensor development since it influences practical applications. In brief, the selectivity analysis of a developed GO@LbL-AuNPs-Anti-Tau SPR biosensor for the detection of Tau-441 antigen in the presence of numerous co-existing interfering agents was performed. For this analysis, BSA, cholesterol, egg albumin, glucose, lactoferrin, protease, calcium, and bicarbonate were chosen as interfering agents based on the composition of AD patient and health person blood, saliva, and cerebrospinal fluid (CSF). Furthermore, in the selectivity analysis of the produced GO@LbL-AuNPs-Anti-Tau SPR

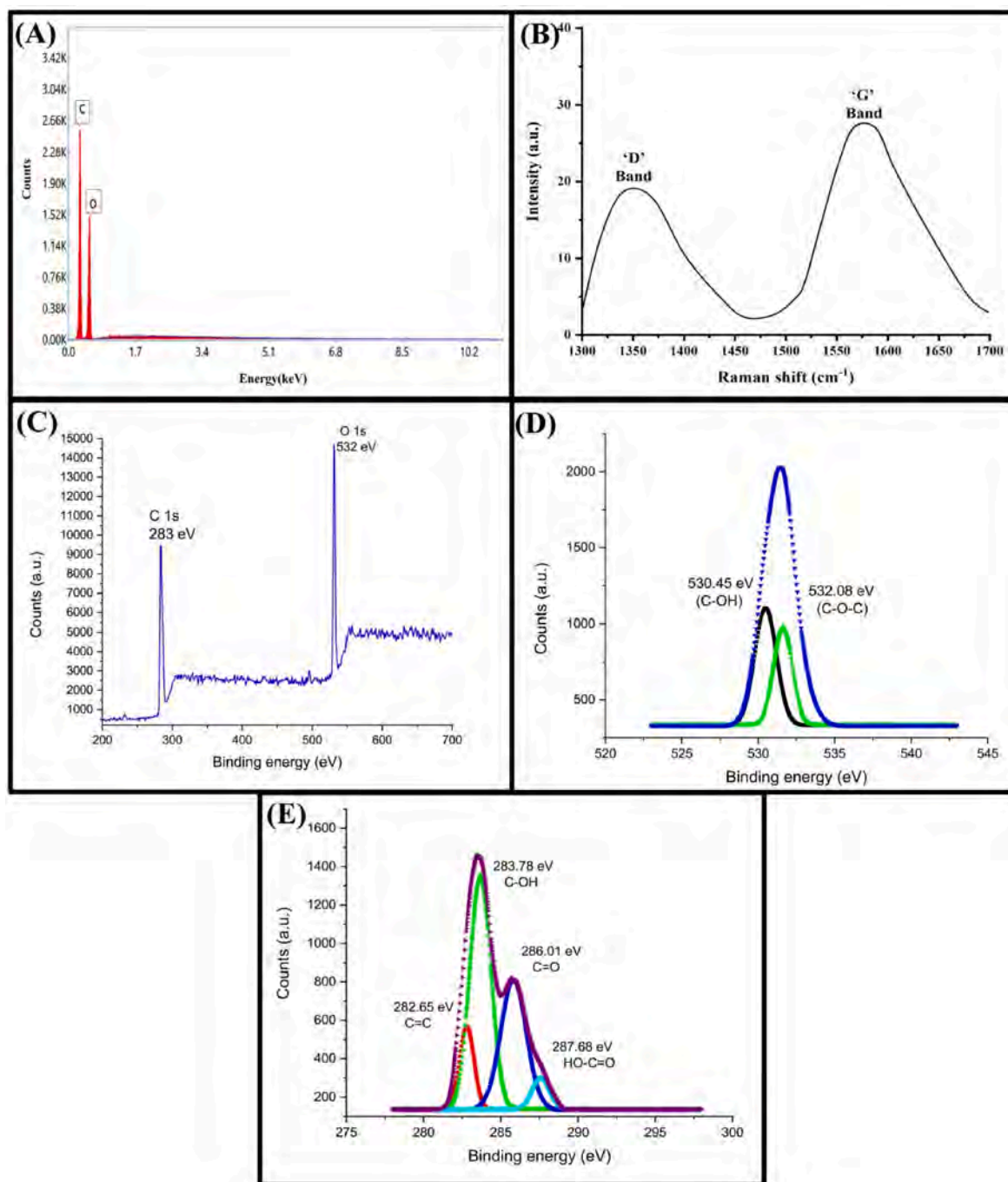


Fig. 2. (A) EDAX spectrum of GO; (D) Raman analysis of GO; (C) Survey scan spectra of GO. XPS core level spectrum of (D) C1s and (E) O1s.

biosensor for Tau-441 antigen, the most typically acquired AD biomarker namely beta-amyloid (1–42), was used as an interfering agent that helps to confirm the impact of other AD biomarkers in Tau protein analysis. Concisely, preferred interfering agents and Tau-441 antigen were added into a tube with PBS (pH 7.4, 0.1 mol/L) to make the known amount of concentration (100 fg/mL). For estimation, a single interfering substance concentration was injected with a flow rate of 10 μ L/min at 25 $^{\circ}$ C. Then, a response from GO@LbL-AuNPs-Anti-Tau SPR biosensor was noticed for a separate concentration of interfering agents and Tau-441 antigen. Here, it was intended to assure the selectivity aptitude of the fabricated ultrasensitive biosensor. The stability analysis and reproducibility analysis of projected GO@LbL-AuNPs-Anti-Tau SPR biosensors were also explored. In short, the stability of constructed GO@LbL-AuNPs-Anti-Tau SPR biosensor was investigated in triplicate

for up to 24 h utilizing 50 fg/mL of Tau-441 antigen at different time intervals ($N = 8$). In addition, manufactured GO@LbL-AuNPs-Anti-Tau SPR biosensors ($N = 6$) were assessed for reproducibility using Tau-441 antigen at 50 fg/mL. Finally, the percent relative standard deviation (% RSD: $SD/Mean \times 100$) was calculated for both stability and reproducibility analysis.

2.7. Spiked sample analysis of Tau-441 antigen

The real-time analysis of Tau-441 antigen in a spiked sample of blood and saliva was performed to ensure the practical applicability of the GO@LbL-AuNPs-Anti-Tau SPR. To avoid sensing loop clogging, a blood and saliva sample was taken from male wistar rats (body weight: 300–350 g) and then diluted with PBS buffer pH 7.4 (1:2). After this, the

samples were evaluated for the presence of Tau-441 antigen. Then, 50 fg/mL of Tau-441 antigen was spiked in collected blood and saliva samples of an animal ($N = 3$). Here, a spiked sample was evaluated for percent (%) recovery and % RSD of Tau-441 antigen in the occurrence of several interfering molecules in saliva and blood. At last, these rats were further subjected to AD induction to assure real pre-clinical applicability of fabricated GO@LbL-AuNPs-Anti-Tau SPR biosensors.

3. Tau-441 antigen biosensing in AD-induced animals using GO@LbL-AuNPs-Anti-Tau SPR biosensor

In this study, the GO@LbL-AuNPs-Anti-Tau SPR biosensor was used to assess Tau-441 antigen in saliva, blood, and CSF samples obtained from AD-induced rats (Ref. No: IAEC/RCPIPER/2016-17/37). At first, the male Wistar rats ($n = 9$, wt: 300–350 g) were chosen for this investigation. In brief, the selected male Wistar rats ($n = 9$) were tested for the presence of Tau 441 antigen in saliva, blood, and CSF samples at 0 days. Following this confirmation, the healthy rats were subjected to AD induction. The rats ($n = 6$) were given a day-one dose of STZ (3 mg/kg) through the intracerebroventricular (icv) route using a micro syringe. A similar method was also favored on the third day for the rats. Following that, the treated rats' memory and learning behavior were monitored. On day 14, saliva, blood, and CSF samples were taken and diluted with PBS buffer 7.4 (1:2). The samples were then analyzed for Tau 441 antigen detection, which aids in the development of AD. After 21 days, blood and saliva samples were collected and tested for Tau-441 antigen levels using a custom-built SPR biosensor. In addition, the rats were slaughtered under anesthesia using chloral hydrate (240 mg/kg) intraperitoneally (i.p.) in a 4% solution. The CSF sample was obtained here and treated to the next procedure. All CSF, blood, and saliva samples were examined for the existence of Tau-441 antigen using a constructed GO@LbL-AuNPs-Anti-Tau SPR affinity biosensor under the optimized conditions described above.

4. Results and discussion

In this study, the GO nanosheets were produced by adopting an earlier documented process and then it was analyzed through numerous *in vitro* spectroscopical characterizations. After this, *Colocasia esculenta* stem extract was chosen as the reducing agent for the formation of green-made AuNPs. Having followed that, the AuNPs = PAH-PSS-PAH as an LbL polyelectrolyte assembly was formed and then preferred to affinity bioreceptor localization using carbodiimide chemistry. Furthermore, GO@LbL-AuNPs-Anti-Tau SPR biosensor was adopted for Tau-441 sensing as an exceptionally responsive and specific affinity biosensing probe. Then, the anti-interference possibility and real-time analysis were achieved by adopting a produced GO@LbL-AuNPs-Anti-Tau SPR-based affinity biosensor.

4.1. Characterization of GO

In this study, the UV-Vis spectrum of formed GO dispersion from graphite flakes revealed two absorption peak points at 230.5 nm and 304 nm, accordingly (Fig. 1A). In brief, the peak at 230.5 nm was revealed for the C=C bonds comprising π - π^* transition of the amorphous carbon system. Furthermore, the aromatic C=O bonds with n - π^* transitions exhibited a large shoulder peak at 304 nm. Because of the existence of carbon and oxygen-regulated functionality, allows the synthesis of GO [27,28]. According to the literature, particle size determination may offer the distribution and average diameter of nanomaterials, while stability analysis employing zeta potential insured the stability of nanomaterials in the solvent [27]. Briefly, the particle size and PDI of GO were determined to be 90.9 nm and 0.24, respectively (Fig. 1B), indicating a homogeneous distribution of nanosized flakes of GO in formed water-containing dispersion. Fig. 1C depicted GO-nanomaterial zeta potential. Herein, the zeta potential of GO was obtained to be

−27.60 mV ensuring its good stability in an aquatic environment. Principally, the negative potential of GO is attributable to the high carboxylic functionality of the GO planar nanosheet [29].

Fig. 1D exhibits FTIR spectra of GO nanomaterial. It displays the broad angle peak at 3300 cm^{-1} , which is connected with the OH and/or COOH functionality seen in GO frameworks. The C=O stretching vibrations and the oxidized graphitic domain containing C=C stretching vibrations are represented by the high-intensity peaks at 1730 cm^{-1} and 1605 cm^{-1} , respectively. The high-intensity peaks at 1078 cm^{-1} and 1027 cm^{-1} are attributed to the C-O stretching vibrations of the epoxy and alkoxy functional groups, respectively. Overall, it ensured the presence of oxygen-based functional groups such as carboxyl, epoxy, hydroxyl, and carbonyl in the produced GO structure. The HR-TEM pattern of GO flakes is shown in Fig. 1E and F. Herein, the flake structural consistency of produced GO nanosheets was verified by HR-TEM images. In summary, it reveals no structural flaws, such as holes or rips, on the surface of GO nanosheets. Overall, it ensured that graphite flakes were oxidized into multilayer GO nanosheets with a coarse texture [28,30].

Figs. S1–A and B shows the SEM images of synthesized GO nanosheets. It depicts a 2D, large, layered, randomly aggregated, somewhat wrinkled structure of GO nanosheets [31]. It also illustrates the folding on the plane of the resulting GO nanosheets. Altogether, the addition of oxygen atoms into carbon-based graphite flakes permits the separation of sheets into nanosized scales. As an outcome, it supports the exfoliation of graphite flakes and the formation of nanosized GO [32]. Fig. 2A depicts the EDAX spectrum of synthesized GO nanomaterial from graphite flakes. In brief, the EDAX spectrum reveals that GO contains 65.43 wt% carbon (C) and 34.57 wt% oxygen (O). As a result, it is evident that the produced GO is devoid of other elemental contaminants. As an outcome, it was proven that oxygen-based functionalities such as epoxy, hydroxyl, and carboxyl are available on basal planes for covalent connections in formed GO nanosheets [33].

The Raman spectrum of the derived GO nanomaterial is illustrated in Fig. 2B. In essence, it exhibits the 'D' band at 1348.15 cm^{-1} and the 'G' band at 1584.20 cm^{-1} [34], which verified the occurrence of a κ -point phonon (A_{1g} symmetry) centered breathing mode and first-order scattering (vibration) of sp^2 hybridized carbon (E_{2g} phonon), respectively. The intensity ratio (I_D/I_G) of the 'D' and 'G' was observed to be 0.69, which assists in the assurance of imperfections in graphite-based nanomaterials. Concisely, the resulting intensity ratio was less than one, confirming the synthesis of hydrophilic GO nanosheets. As per the literature, if the intensity changes from less than one to more than one, it indicates a reduction of GO (hydrophobic nature). Overall, it ensured the production of hydrophilic sp^2 hybridized carbon-based GO from graphite flakes [35]. Figs. S1–C and D depicts the diffractograms of graphite flakes and synthesized GO, respectively. In summary, Figs. S1–C reveals significant diffraction peaks at 2θ : 23.95° and 26.50° , respectively, while the intercellular spacing was determined to be 3.71 \AA and 3.35 \AA , confirming the high crystalline structure of graphite flakes. The diffractogram of GO (Figs. S1–D) after oxidation reveals a decrease in peak intensity when compared to the pristine graphite flakes. It demonstrates a new low strong peak at $2\theta = 8.63^\circ$, confirming the entire development of GO nanomaterial from pristine graphite flakes. A low-intensity diffraction peak was also found at $2\theta = 25.32^\circ$ and 26.66° , indicating that the GO nanomaterials is practically associated with oxygen atoms. The intercellular spacing (d) for GO was estimated to be 10.22 \AA , ensuring an increase in distance between fields in the GO above pure graphite flakes. Therefore, it demonstrated the coexistence of water (H_2O) molecules and the functionality of oxygen in the carbon structure [30,36].

Fig. 2C depicts the XPS spectra of GO nanosheets. In summary, it demonstrates the XPS survey scan spectra of GO nanosheets. In this, the 'C1s' and 'O1s' core level high resolutions were found at binding energies of 283 eV and 532 eV, respectively. The core-level high-resolution XPS spectrum of 'O1s' is shown in Fig. 2D. It essentially displays the two 'O'-

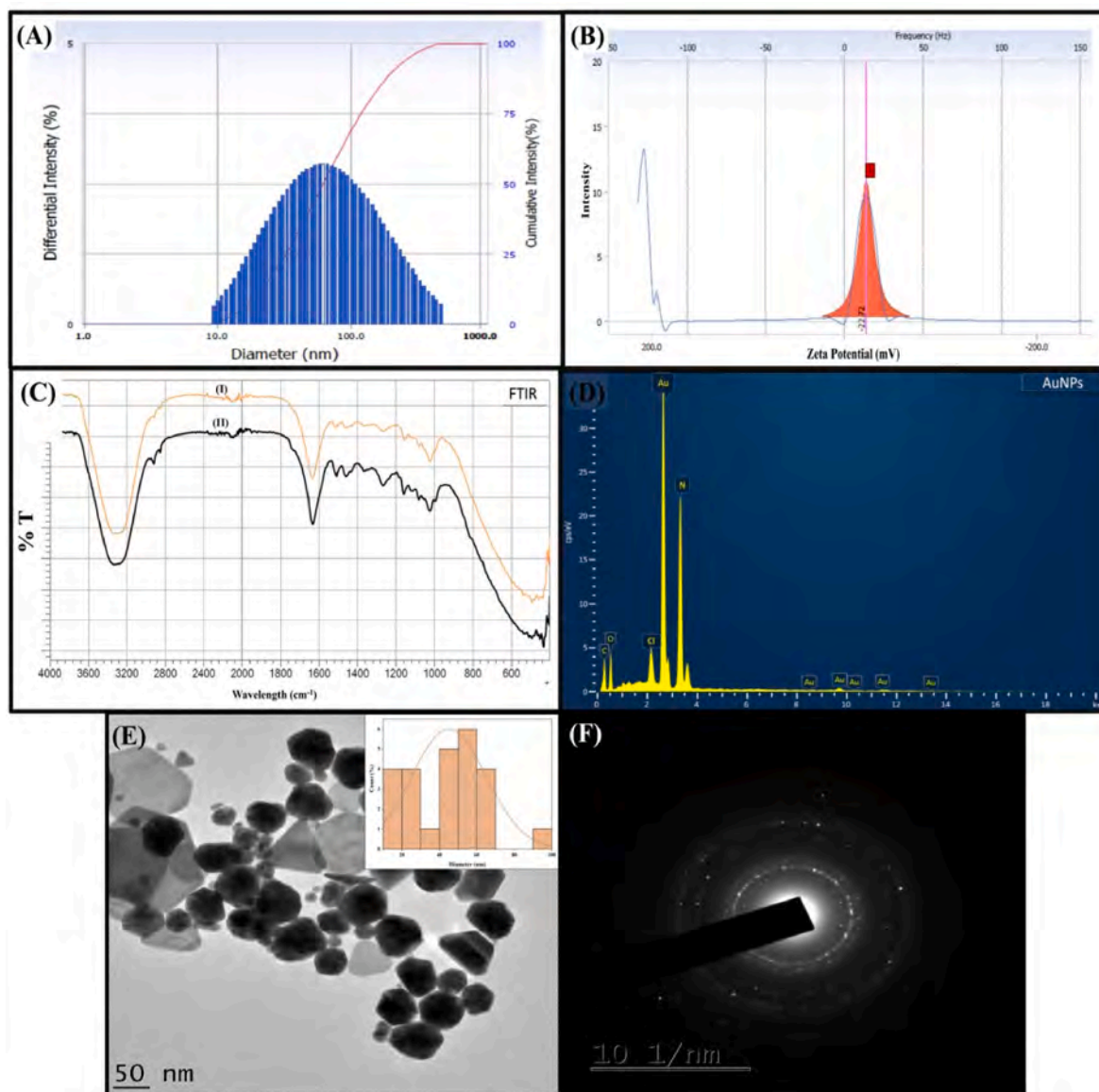


Fig. 3. (A) Particle size and (B) Zeta potential analysis of green synthesized AuNPs. (C) FTIR spectra of stem extract of *Colocasia esculenta* (I) and green synthesized AuNPs (II). (D) EDAX spectrum of obtained AuNPs. (E) HR-TEM images of AuNPs. (F) SAED pattern of green-made AuNPs. (For interpretation of the references to color in this figure legend, the reader is referred to the Web version of this article.)

based constituents including 'C–OH' and 'C–O–C', at 530.45 eV and 532.08 eV, accordingly. Fig. 2E displays the high-resolution core-level 'Cl's' spectra. It comprises the 'C'-based components with various functional groups. Mainly, it has oxygenated components such as 'C–OH', 'C=O', and 'OH–C=O' at 283.78 eV, 286.01 eV, and 287.68 eV, respectively. As well, it has non-oxygenated components such as 'C=C' at 282.65 eV [37]. Overall, it ensured that sp^2 carbon, carboxylic functional groups, and epoxide were incorporated into the production of GO nanosheets. Furthermore, it ensured that GO nanomaterials included only 'C' and 'O' with no contaminants [38].

4.2. Characterization of green synthesized AuNPs

In this study, adequate characterizations of green synthesized AuNPs were performed to confirm the creation of a stable and pure form of nano-dimension-based AuNPs. Primarily, the formation of AuNPs was studied relying on the variations in the color of the reaction mixture. In brief, Figs. S2–A shows the images of *Colocasia esculenta* stem extract (I), chloroauric acid solution (II), and green synthesized AuNPs (III). The

inclusion of purified *Colocasia esculenta* stem extract to chloroauric acid leads to a color shift from pale yellow to ruby red [39] during 4 h of reaction time that was an absence in extract and chloroauric acid. According to the literature, interacting electromagnetic fields resulted in a cumulative oscillation of free conduction electrons that provide intense color. These are acknowledged as surface plasmon resonances [40]. After this confirmation, the AuNPs were subjected to additional characterization such as UV Vis spectroscopy, FTIR spectroscopy, HR-TEM analysis, XPS analysis, SEM-EDAX analysis, and so on. Figs. S2–B shows the UV–Vis spectra of concentrated *Colocasia esculenta* stem extract (I), chloroauric acid solution (5 mM) (II), and green synthesized AuNPs (III). In the case of extract, it exhibited absorption peaks at 271.5 nm and 343.5 nm, which may be because of existence of different phytochemicals (Fig. S2-B-I). UV Vis spectra of prepared 5 mM chloroauric acid were found at 263 nm and 364.5 nm (Fig. S2-B-II) confirming the presence of a pure form of chloroauric acid. Finally, the formation of AuNPs using stem extract and chloroauric acid was confirmed using UV Vis spectra. Here, synthesized AuNPs displayed an absorption (surface plasmon resonance) band at 539 nm (Fig. S2-B-III).

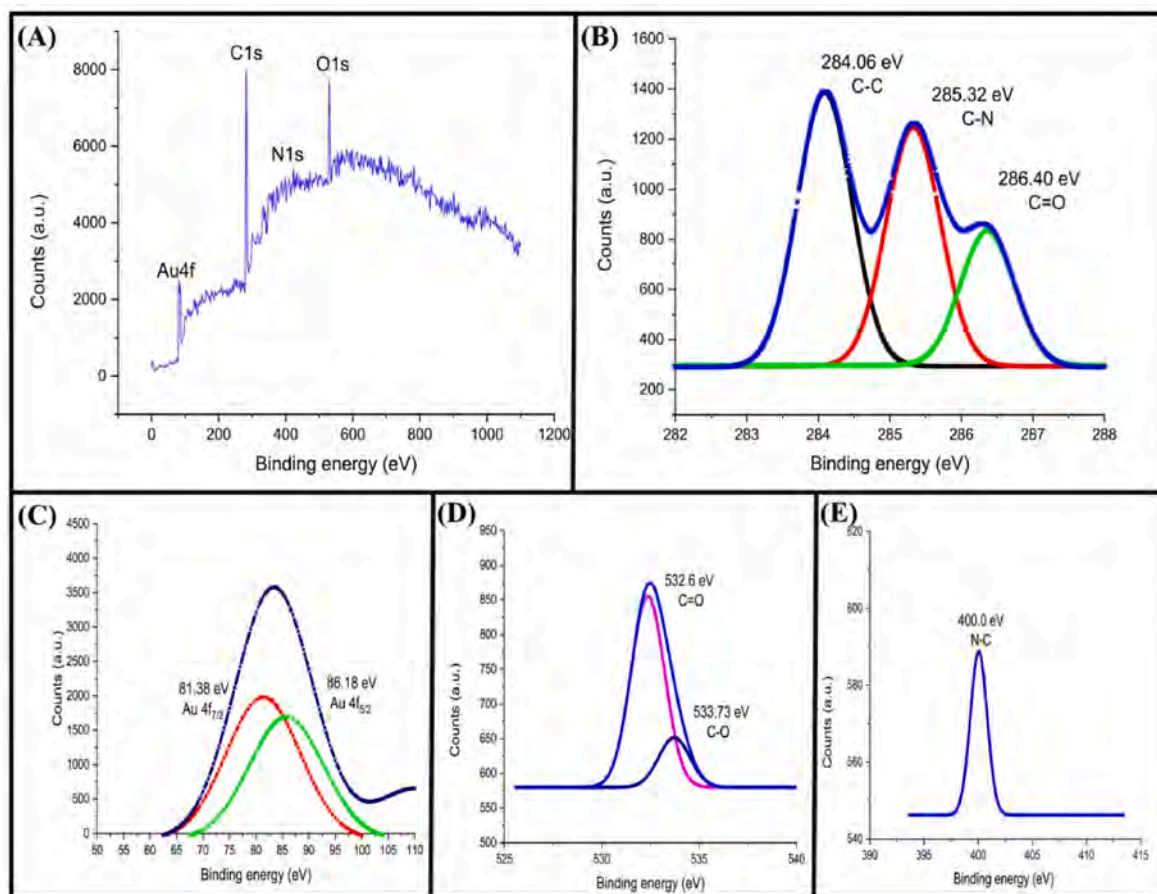


Fig. 4. (A) Survey scan spectrum of green obtained AuNPs. XPS core level spectrum of (B) C1s, (C) Au4f, (D) O1s, (E) N1s. (For interpretation of the references to color in this figure legend, the reader is referred to the Web version of this article.)

In this, AuNPs exhibited wide plasmon bands, preceded by an absorption tail approaching the longer wavelength zone [41]. As a result, it demonstrated the effective green synthesis of AuNPs utilizing *Colocasia esculenta* stem extract as a reducing agent, stabilizing agent, and capping agent for gold ions.

The mean particle size, as well as PDI of the eco-friendly produced AuNPs, were determined to be 52.12 nm and 0.29, respectively (Fig. 3A). Finally, the PDI and particle size of AuNPs validated their uniform dispersion in water. The zeta potential of AuNPs produced using the extract was -22.72 mV (Fig. 3B), indicating colloidal stability. Overall, the *Colocasia esculenta* stem extract containing biomolecules acts as a stabilizing agent for AuNPs [42]. The possible functional groups of biomolecules involved in the capping and reduction of AuNPs were identified using FTIR spectroscopy. Fig. 3C–(I) depicts the FTIR spectra of the stem extract of *Colocasia Esculenta*. In brief, the major stretching vibrations appeared at 3000 cm^{-1} to 3600 cm^{-1} , which denotes the existence of the 'O–H' stretching vibrations, which denotes the occurrence of functional groups comprising the 'O–H' stretch. The intense peak stretching at 1300 cm^{-1} and 1700 cm^{-1} specify the occurrence of 'C–O' and 'C=O' in the prepared stem extract. Furthermore, peaks at 1600 cm^{-1} and 1550 cm^{-1} assured the occurrence of amide linkages of the proteins present in the stem extract of *Colocasia Esculenta*. As well, the peak at 1050 cm^{-1} assured the presence of 'C–OH' and 'C–O–C' stretching vibrations. The 'C–N' stretching was obtained at 1380 cm^{-1} , which validates the existence of amine functionality in the *Colocasia Esculenta* stem extract. Fig. 3C–(II) shows the FTIR spectrum of green synthesized AuNPs. In brief, a peak at 1720 cm^{-1} was obtained due to the carboxylic (C=O) stretching vibrations mode because of the 'COOH' functionality in the extract bound to the AuNPs. The peak at 1315 cm^{-1}

validates the existence of 'C–O' in AuNPs. The occurrence of amide bonds I and II were obtained at 1610 cm^{-1} and 1570 cm^{-1} , which shows the shifting towards the higher frequency as compared to the plain stem extract. Notably, it may be because of the capping and reduction of AuNPs in the presence of biomolecules in the stem extract of *Colocasia Esculenta* [41]. In addition, the 'C–H' bond stretching is observed in the region of 2932 cm^{-1} as well as 2914 cm^{-1} in stem extract. Interestingly, the 'C–H' bond from the stem extract is divided into two vibrations namely 2912 cm^{-1} and 2822 cm^{-1} in FTIR of AuNPs confirming the change in transmittance which may be the formation of AuNPs [43].

The surface morphology of developed AuNPs is seen in Figs. S2–C. It depicts the smooth surface morphology with various forms of AuNPs such as spherical, rod, polygonal, etc [44]. Furthermore, there is no aggregation of green-made AuNPs in SEM images, implying high stability due to the presence of stabilizing and capping agents in the extract. As a result, the produced AuNPs were submitted to HR-TEM analysis to ensure particle size and form. The EDAX confirms the presence of % element composition in produced AuNPs [45]. The EDAX spectrum of green-produced AuNPs is shown in Fig. 3D. In summary, it demonstrates a significant signal for 'Au', 'O', 'C', and 'N' wherein percent weight (% wt) was found to be 22.97 %wt, 18.14 %wt, 30.64 %wt, and 21.9 %wt, respectively. In addition, it shows the existence of chlorine (Cl) with 6.35 %wt because of AuCl_4^- a small fraction. Concisely, it proved the existence of 'Au', 'O', 'N', and 'C' in green-produced AuNPs. The HR-TEM was used to analyze the size, particle distribution, and structure/shape of the green-produced AuNPs [46], as shown in Fig. 3E. In summary, the mean diameter of the AuNPs was determined to be within nanometer size, with a spherical particle form and some hexagonal and triangular patterns [44]. Furthermore, the uniform dispersion of

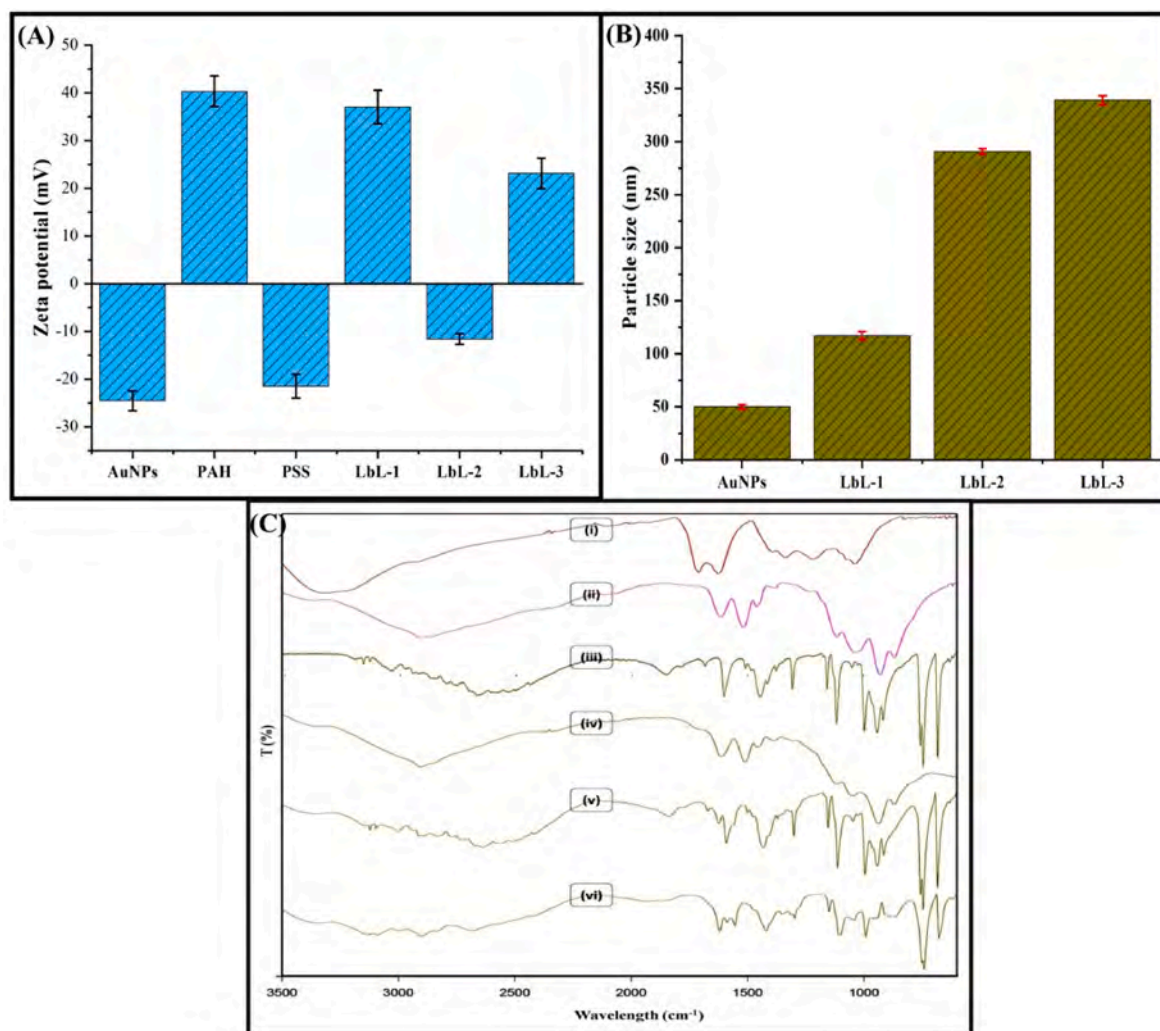


Fig. 5. Zeta potential analysis of obtained AuNPs, PAH, PSS, AuNPs-PAH (LbL-1), AuNPs-PAH-PSS (LbL-2), and AuNPs-PAH-PSS-PAH (LbL-3). (B) Particle size analysis green obtained AuNPs, AuNPs-PAH (LbL-1), AuNPs-PAH-PSS (LbL-1), and AuNPs-PAH-PSS-PAH (LbL-1). (C) FTIR spectra of green synthesized (i) AuNPs, (ii) PAH, (iii) PSS, (iv) AuNPs-PAH, (v) AuNPs-PAH-PSS, and (vi) AuNPs-PAH-PSS-PAH. (For interpretation of the references to color in this figure legend, the reader is referred to the Web version of this article.)

produced AuNPs in a medium is substantiated by the HR-TEM, which revealed no aggregation due to the capping of AuNPs by biomolecules contained in the extract. The average particle size of AuNPs was found to be 45.08 nm (N:25; Software name: ImageJ). As a result, it ensured that the green method successfully produced randomly oriented nanosized, stable, and monodispersed AuNPs. The SAED pattern proved the crystalline architecture of AuNPs [46]. The SAED pattern of produced AuNPs is shown in Fig. 3F. It exhibits the round luminous rings in the SAED model of AuNPs, revealing the crystalline characteristic of AuNPs [41]. The diffractogram of eco-friendly formed AuNPs is displayed in Figs. S2–D. It demonstrates the high-intensity diffraction peak from the range of ($2\theta = 30^\circ\text{--}80^\circ$) [43]. It shows the four high peak intensities at 38.33° , 40.66° , 44.55° , 50.26° , 58.70° , 64.77° , 66.60° , 73.90° , and 77.8° , which proved the crystalline structure of green made AuNPs. As well, there is no extra high-intensity peak in the diffractogram of AuNPs, indicating the excellent purity of AuNPs produced using a greener method [47].

A review of the literature indicated that the XPS spectrum offers facts on the surface of the substrate comprising elements such as metal ions, carbon, nitrogen, oxygen, and so on. Here, the XPS spectrum of green-produced AuNPs is shown in Fig. 4. In summary, it gives precise insights into the chemical composition and structure of gold (Au), carbon (C), nitrogen (N), and oxygen (O) in the produced nanosized material

AuNPs using the green method. Fig. 4A depicts the survey scan pattern of green synthesized AuNPs for elements primarily 'Au $4f_{7/2}$ ', 'C1s', 'N1s', and 'O1s' with binding energies of 82 eV, 283 eV, 423 eV, and 530 eV, respectively. Fig. 4B represents the deconvoluted spectra of 'C1s'. It exhibits three binding energy levels for 'C–C', 'C–N', and 'C=O' at 284.06 eV, 285.32 eV, and 286.40 eV, accordingly. Fig. 4C illustrates the high core-level spectra of 'Au $4f$ '. Here, it indicates peaks with binding energies of 81.38 eV and 86.18 eV for 'Au $4f_{7/2}$ ' and 'Au $4f_{5/2}$ ', respectively, which verify the appearance of AuNPs in formed nanoparticles. In the instance of the 'O1s' high core level spectra (Fig. 4D), it reveals two peaks at 532.6 eV and 533.73 eV as binding energy, which is attributable to the existence of 'C=O' and 'C–O', individually. Fig. 4E illustrates the XPS core level spectrum of 'N1s'. It yields one peak with a binding energy of 400 eV, which is allocated to the 'N–C' bonding. As a result, it signifies that no more impurities are present in the produced AuNPs. In a sense, it ensures that 'Au', 'N', 'C', and 'O' are abundant in eco-friendly formed AuNPs [48].

4.3. Characterizations of LbL assembly

The zeta potentials of freeze-dried AuNPs, PAH, PSS, AuNPs-PAH (LbL-1), AuNPs-PAH-PSS (LbL-2), and AuNPs-PAH-PSS-PAH (LbL-3) are depicted in Fig. 5A. In summary, zeta potential testing of

polyelectrolyte (PAH/PSS)-coated AuNPs revealed the occurrence of cationic polyelectrolyte (PAH) or cationic polyelectrolyte (PSS) outer layer in the proposed LbL assembly. Herein, the zeta potential of AuNPs, PAH, and PSS was found to be -24.55 ± 0.20 mV, $+40.33 \pm 0.07$ mV, and -21.48 ± 0.15 mV, respectively. In the case of LbL assembly, the zeta potential of AuNPs-PAH, AuNPs-PAH-PSS, and AuNPs-PAH-PSS-PAH was obtained to be $+37.02 \pm 0.06$ mV, -11.61 ± 0.49 mV, and $+23.14 \pm 0.11$ mV, respectively. It implies that the zeta potential changes in response to changes in the outer layer of the LbL arrangement. In summary, the positive zeta potential of PAH as an out layer of LbL assembly is revealed in the presence of amine functionality, whereas the negative zeta potential of PSS as an exterior coating of LbL assembly is noted due to the presence of SO_3^- [49]. Overall, it demonstrated the effective deposition of polyelectrolytes (specifically PAH and PSS) on the surface of AuNPs as part of an LbL assembly. It also ensured the creation of a stable form of LbL assembly in a solvent system. Moreover, it is advantageous for subsequent antibody binding on the surface of the LbL assembly.

The particle size assessment of freeze-dried AuNPs, AuNPs-PAH, AuNPs-PAH-PSS, and AuNPs-PAH-PSS-PAH is presented in Fig. 5B. In general, the particle size and PDI of lyophilized AuNPs were 50 nm and 0.30, accordingly. It verified that nanosized AuNPs were distributed throughout the solvent system. In the case of LbL assembly, the particle size and PDI of AuNPs-PAH were revealed to be 117.10 nm and 0.29, respectively, which represents the rise in the mean particle size of AuNPs following the deposition of the PAH layer. Likewise, AuNPs-PAH-PSS and AuNPs-PAH-PSS-PAH had average particle sizes of 291 nm and 339.2 nm with PDI values of 0.27 and 0.20, respectively. The enhanced mean diameter of polyelectrolyte-coated AuNPs ensured the formation of PSS and PAH layers. Ultimately, particle size analysis ensured the formation of LbL assemblies and the homogeneous dispersion of constructed nanosized LbL assemblies in a solvent system without aggregating. After this confirmation, the freeze-dried AuNPs-PAH-PSS-PAH were validated using SEM-EDAX analysis to ensure the exact average diameter of each LbL assembly. The chemical compositions of the constructed LbL framework on the outside of green-produced AuNPs were confirmed using FTIR spectroscopy.

Figs. S3–A depicts the SEM image of AuNPs-PAH-PSS-PAH. Here, the deposition of PAH and PSS on the surface of AuNPs resulted in the alteration in surface morphology that because of the coating of irregular and pointed corners of AuNPs. In addition, it evidenced that the wrinkled morphology that because of the drying process. The size of developed AuNPs-PAH, AuNPs-PAH-PSS, and AuNPs-PAH-PSS-PAH assemblies was confirmed using HR-TEM analysis. Figs. S3–B demonstrates the EDAX spectrum of AuNPs-PAH-PSS-PAH. In summary, it demonstrates a significant signal for 'Au', 'O', 'C', 'S', and 'N' wherein percent weight (% wt) was found to be 17.76 %wt, 10.55 %wt, 41.16 %wt, 11.43 %wt, and 11.48 %wt, respectively. In addition, it shows the existence of 'Cl' and sodium (Na) with 6.32 %wt and 1.3 wt% because of AuCl_4^- a small fraction and PSS, respectively. Concisely, it proved the existence of 'Au', 'O', 'N', 'S', and 'C' in AuNPs-PAH-PSS-PAH assembly. Fig. 5C shows the FTIR spectrums of AuNPs, PAH, PSS, AuNPs-PAH, AuNPs-PAH-PSS, and AuNPs-PAH-PSS-PAH overlay. In summary, the FTIR spectra of AuNPs displayed the peak for 'C=O' stretching vibrations at 1720 cm^{-1} , with the existence of 'C–O' verified by the peak intensity at 1315 cm^{-1} . The occurrence of NH_2 functionality (amide bond I and amide bond II) was verified by the peaks at 1590^{-1} , while 'C–H' bond stretching was confirmed by the peaks at 2832 cm^{-1} and 2914 cm^{-1} [41]. The existence of 'N–H' group vibrations is indicated by the appearance of peaks in the FTIR spectra of PAH between 3440 and 3415 cm^{-1} . Peaks at 1615 – 1519 cm^{-1} were related to 'NH' asymmetric vibrations (protonated $-\text{NH}_3^+$), whereas the peak at 2905 cm^{-1} was ascribed to asymmetric 'C–CH₂' vibrations [24]. FTIR spectrum of PSS indicates 'C–H' stretching vibrations at 2930 cm^{-1} , whereas benzene ring vibrations (in-plane skeleton and in-plane bending vibrations) are found at 1153 cm^{-1} and 1113.12 cm^{-1} , respectively. The existence of

' SO_3^- ' (sulphonate group) in PSS was confirmed by the peak at 993.14 cm^{-1} . Overall, it ensured the presence of sulphonate functional groups in a PSS [23]. The FTIR spectra of AuNPs-PAH reveal peaks at 1619 – 1514 cm^{-1} that corresponds to the 'NH' asymmetry of PAH. In the instance of the AuNPs-PAH-PSS FTIR spectrum, a peak at 992.45 cm^{-1} verified the presence of ' SO_3^- ' (sulphonate group) of PSS, whilst peaks at 1620 – 1593 cm^{-1} were associated with the 'NH' asymmetry of PAH. Similarly, the peaks at 993.50 cm^{-1} and 1625 – 1520 cm^{-1} verified the emergence of AuNPs-PAH-PSS-PAH. Overall, the peak related to PAH and PSS ensured the development of LbL assembly [24].

4.4. Biosensing of Tau-441 antigen

In this work, the GO@LbL-AuNPs-Anti-Tau SPR biosensor was developed employing GO, AuNPs-PAH-PSS-PAH@Anti-Tau conjugate, and amine-functionalized Au-coated glass chip. Initially, GO nanosheets adhered to the surface of an amine-functionalized Au-coated glass chip using EDC/NHS chemistry. In this study, the increase of GO dispersion concentration from $100\text{ }\mu\text{g/mL}$ to $500\text{ }\mu\text{g/mL}$ demonstrates a linear relationship with SPR response units. However, more increases in the concentration of GO proved the lack of SPR response. As a result, for the design of the predicted SPR biosensor, $500\text{ }\mu\text{g/mL}$ of GO dispersion was considered as an optimized concentration. In this shadow, repeat injections of optimized GO resulted in saturation, with no SPR response seen in the sensorgram. In a nutshell, it ensured that amine-functionalized sensor surface sites were completely engaged with GO nanosheets (Figs. S4–A). Here, a strong connection between the activated carboxylic functionality of GO and the sensor chip's amine functional groups was established via carbodiimide chemistry. Importantly, the purpose of GO nanosheet applications in SPR biosensor was to provide a greater surface area and precise affinity that is beneficial for enhanced SPR biosensing. Moreover, the GO nanocomposite-stacking interactions, hydrogen bonding, electrostatic interaction, and especially hydrophilic affinity enhanced biomolecule sorption possibilities in SPR biosensors. Furthermore, the carboxylic functions of GO allow for the modification of the real interface features of the biosensor layer for bioreceptor adsorption via covalent banding. As a result, it aids in controlling the band gap. It also has strong biocompatibility with biomolecules [50].

Then, the AuNPs-PAH-PSS-PAH@Anti-Tau conjugate was created by combining AuNPs-PAH-PSS-PAH and an Anti-Tau rabbit monoclonal antibody. In this step, the carbodiimide chemistry was used to capture Anti-Tau rabbit monoclonal antibodies on the surface of AuNPs-PAH-PSS-PAH assemblies. Activated carboxylic functional groups of antibodies establish a bond with the amine functionality of AuNPs-PAH-PSS-PAH assembly. As a response, the antibody and LbL assembly create a strong covalent interaction. As a corollary, it provides directed immobilization of the antibody, which aids in providing great selectivity toward the specific antigen. Furthermore, LbL assembly supplies the chemical functionality of interfacial captors, as well as regulated composition and stability. After immobilization of activated GO on the surface of the SPR sensor chip, the produced AuNPs-PAH-PSS-PAH@Anti-Tau conjugates then adhered to the outside of the activated GO nanosheet. Herein, SPR response is linearly related to the addition of $10\text{ }\mu\text{g/mL}$ to $25\text{ }\mu\text{g/mL}$ of AuNPs-PAH-PSS-PAH@Anti-Tau conjugates (Figs. S4–B). Following this validation, the optimized concentration of AuNPs-PAH-PSS-PAH@Anti-Tau conjugates ($25\text{ }\mu\text{g/mL}$) was used for the final biosensing of Tau-441 antigen. Here, it was injected in duplicates that exhibited no SPR response for the second incorporation of AuNPs-PAH-PSS-PAH@Anti-Tau conjugate. Hence, it validated the saturation of AuNPs-PAH-PSS-PAH@Anti-Tau conjugates on the face of activated GO nanosheets attached to the sensor chip surface. Interestingly, the immobilization of bioconjugates is feasible owing to the abundance of functional groups in GO, which results in rough surfaces and greater surface area. Both of these GO properties enable the immobilization of AuNPs-PAH-PSS-PAH@Anti-Tau

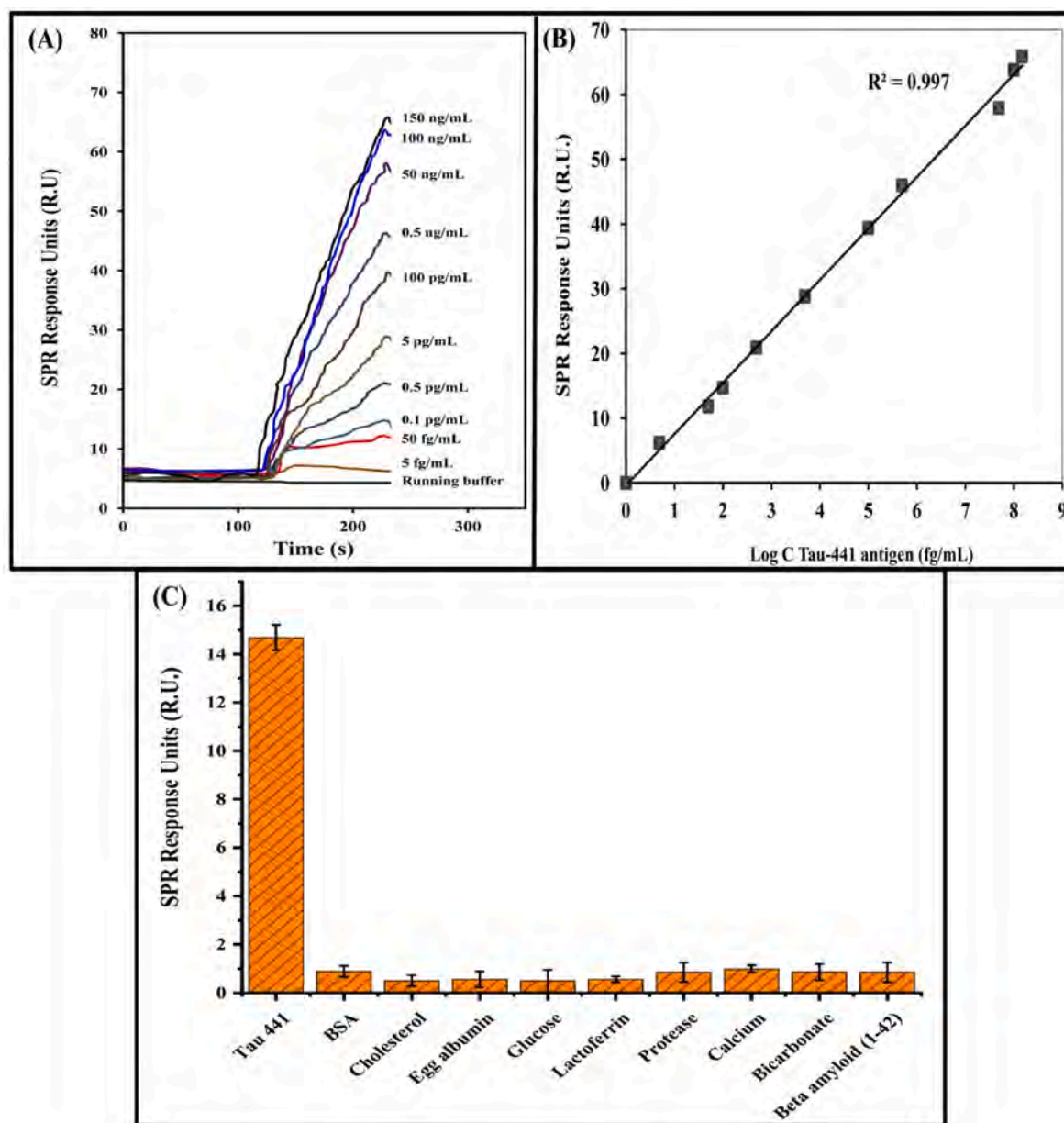


Fig. 6. (A) SPR sensorgram recording of concentration of Tau-441 antigen (5 fg/mL to 150 ng/mL) vs response (RU) using fabricated GO@LbL-AuNPs-Anti-Tau SPR biosensor. (B) The linear relationship between Tau-441 antigen concentrations and SPR response units. (C) The anti-interference potential of GO@LbL-AuNPs-Anti-Tau SPR biosensor for Tau-441 antigen in the presence of several interfering agents.

conjugates in SPR biosensors. Following this step, the free group on the surface of GO was masked using BSA. In this step, the injection BSA (50 $\mu\text{g/mL}$ to 200 $\mu\text{g/mL}$) shows a slight SPR response, possibly due to the almost complete saturation of sites present in GO nanosheets by AuNPs-PAH-PSS-PAH@Anti-Tau conjugates (Figs. S4–C). Further addition of BSA results in a no SPR response in the sensorgram. As a result, the optimized concentration of BSA (200 $\mu\text{g/mL}$) was suggested for the biosensing of the Tau-441 antigen. Repeat inclusion of BSA (200 $\mu\text{g/mL}$) from the sample port in openSPR results in no SPR response, ensuring full masking of active carboxylic functionality. Following this validation, the detection was carried out with varied concentrations of Tau-441 antigen from fg/mL to ng/mL. Fig. 6A depicts the SPR sensorgram recording of Tau-441 antigen concentration (fg/mL) vs SPR response units (RU) using a constructed GO@LbL-AuNPs-Anti-Tau SPR biosensor. Fig. 6B shows the linear correlation wherein the SPR signal enhanced when the log concentration of Tau-441 antigen was raised from 5 fg/mL to 150 ng/mL ($R^2 = 0.997$). In this case, the SPR signal response is 'y',

whereas 'x' reflects the concentration of Tau-441 antigen. Furthermore, the LOD detection was achieved to be 13.25 fg/mL based on '3.3 σ /slope', where standard deviation ($n = 7$) is represented by ' σ ' [$Y = 0.0726x + 0.0567$; $R^2 = 0.996$]. Hence, it assured the boost of the total sensitivity of SPR biosensors. Taken as a whole, it might be because AuNPs, LbL assembly, Au-modified glass chip, GO nanosheets, and affinity bioreceptors were used.

In summary, AuNPs comprise the high collective oscillations of their conduction electrons, which led to localized SPR. As well, AuNPs are more sensitive to changes in a system environment. In this case, linking AuNPs with L-SPR to Au films with propagating plasmons can result in a significant change in SPR reflectivity. As a result, the resonant wavelength shift rises. Furthermore, the utilization of a 2D-based GO nanosheet provides a wider surface area with high surface functionality for AuNPs-PAH-PSS-PAH@Anti-Tau immobilization. In addition, the GO promotes 'RI' by modulating surface plasmon polariton propagation. Besides, the usage of LbL assembly provides specific directions to affinity

Table 1

Comparison of reported biosensor and GO@LbL-AuNPs-Anti-Tau SPR biosensor for detection of Tau protein.

Sr. No.	Types of biosensor	LOD	Linearity range	Ref.
1.	Multichannel SPR	10 fM	2 pM–80 pM	[15]
2.	Localized SPR	10 pg/mL	0–100 ng/mL	[8]
3.	Localized SPR	23.6 fM	10 fM to 100 nM	[51]
4.	MWCNT-SPR	125 pM	–	[52]
5.	SPR fiber sensor	2.4 pg/mL	10 pg/mL to 2360 pg/mL	[53]
6.	GO@LbL-AuNPs-Anti-Tau SPR biosensor	13.25 fg/mL	5 fg/mL to 150 ng/mL	Present work

MWCNTs: Multi-walled carbon nanotubes; pM: Picomolar; fM: Femtogram; pM: Femtomolar; pg: Picogram.

receptors whereas it increases the mass transfer on the 'Au' coated sensing exterior. As a response, it resulted in the 'RI' improvement of the Au-coated sensing chip. Additionally, the conjugation of an 'Au' coated sensor chip with AuNPs-PAH-PSS-PAH@Anti-Tau conjugates may outcome in electromagnetic coupling. Here, the Tau-441 antigen and AuNPs-PAH-PSS-PAH@Anti-Tau conjugate resulted in the dielectric alteration of the selected metal carrier. Overall, it offers an increase in the signal of SPR response. Therefore, the integration of GO nanosheets, AuNPs-PAH-PSS-PAH@Anti-Tau conjugate, and amine-functionalized Au-coated glass chip culminated in expanded SPR biosensor sensitivity when compared to previously published literature. Table 1 compares reported biosensors to GO@LbL-AuNPs-Anti-Tau SPR biosensors in terms of LOD and linearity range for Tau-441 detection.

4.5. Selectivity, stability, and reproducibility analysis

Selectivity is one of the critical variables in biosensor technology that ensures the functioning of biosensors in the presence of numerous interfering components. In this case, the selectivity analysis for Tau-441 antigen was worked out utilizing a GO@LbL-AuNPs-Anti-Tau SPR biosensor in the existence of diverse interfering agents such as BSA, cholesterol, egg albumin, glucose, lactoferrin, protease, calcium, bicarbonate and beta-amyloid (1–42). The selectivity aptitude of the GO@LbL-AuNPs-Anti-Tau SPR biosensor for Tau-441 antigen in the presence of other interfering molecules is demonstrated in Fig. 6C. In essence, the absence of Tau-441 antigen in samples suggests no SPR response, whereas the occurrence of Tau-441 antigen signifies an SPR response. In the case of interfering agents, there is no/minimal response for interfering samples BSA, cholesterol, egg albumin, glucose, lactoferrin, protease, calcium, and bicarbonate. As well, the intended SPR biosensor resulted in no SPR response after the incorporation of beta-amyloid (1–42) from the samples port. As a result, it ensured that the suggested affinity GO@LbL-AuNPs-Anti-Tau SPR biosensor can differentiate Tau-441 antigen from other interfering agents owing to their high selectivity. Other analytical characteristics measured were the stability ($N = 8$) and reproducibility ($N = 6$) of the affinity AuNPs-PAH-PSS-PAH@Anti-Tau biosensor (Table 2). In summary, the GO@LbL-AuNPs-Anti-Tau SPR biosensors showed a % RSD of 2.61% (SD: 2.62) and 2.52% (SD: 2.49) for stability (Fig. 7A) and reproducibility (Fig. 7B), respectively. Here, the % RSD was found to be less than 5% which confirmed the good stability and reproducibility in an analysis of Tau-441 antigen using affinity AuNPs-PAH-PSS-PAH@Anti-Tau biosensor.

Table 2

Summary of stability and reproducibility analysis of GO@LbL-AuNPs-Anti-Tau SPR biosensor.

Sr. No.	Name of the analytical parameter	Concentration of Tau-441 added	Average Tau-441 concentration found	Average % recovery Tau-441	SD	% RSD
1.	Stability	50 fg/mL	49.89 fg/mL	99.78%	2.61	2.62
2.	Reproducibility	50 fg/mL	49.40 fg/mL	98.80%	2.49	2.52

N: No. of samples, SD: Standard deviation (\pm); % RSD: % relative standard deviation.

4.6. Spiked sample analysis

Table 3 depicts the results of a Tau-441 antigen-spiking sample test in blood and saliva. In brief, it shows a % recovery of 95.40% and % RSD of 1.50% for the spiked levels of Tau-441 antigen (50 fg/mL) in saliva. Similarly, blood samples showed 97.60% and % RSD for 1.47% of Tau-441 antigen concentration (50 fg/mL). Here, % RSD was found to be less than 5% for both spiked sample analyses. Therefore, the % recovery of Tau-441 antigen in spiked samples demonstrates the potential reliability of the GO@LbL-AuNPs-Anti-Tau SPR biosensor in detecting Tau-441 antigen in clinical samples. Overall, it demonstrated the GO@LbL-AuNPs-Anti-Tau SPR biosensor's high specificity for Tau-441 antigen in complex samples.

4.7. Tau-441 antigen biosensing in AD-induced animals using GO@LbL-AuNPs-Anti-Tau SPR biosensor

To ensure the practicability of the GO@LbL-AuNPs-Anti-Tau SPR biosensor, the antigen Tau-441 was detected in AD-induced rats. In short, there was no SPR response found for the Tau-441 antigen on 0 days, indicating the lack of tau protein in CSF, blood, and saliva. It confirmed the healthy condition of selected animals. After 18 days of analysis, the concentration of tau protein in the blood, CSF, and saliva was determined to be 206.24 fg/mL, 590.44 fg/mL, and 147.61 fg/mL, respectively. Here, the SPR response for tau protein assured the progression of AD disease in rats. Finally, SPR response was found to be high after 21 days when compared to the initial and 18-day studies. In concisely, the tau protein concentration in blood and saliva was 338.47 fg/mL and 264.69 fg/mL, respectively. As well, tau protein was obtained to be 1.141 pg/mL in CSF samples. Overall, the examination of clinical samples for the detection of tau protein in AD-induced rats confirmed the practical application of GO@LbL-AuNPs-Anti-Tau SPR biosensor.

5. Conclusion

For perhaps the first time, a PAH and PSS -based AuNPs-PAH-PSS-PAH LbL assembly with GO nanocomposite adorned SPR-based astonishingly sensitive and specific affinity biosensor was designed for Tau-441 antigen detection. Briefly, plasmonic AuNPs were obtained adopting an environmentally pleasant green method and then treated to the construction of a polyelectrolyte-based AuNPs-PAH-PSS-PAH LbL arrangement. In this circumstance, opting for a greener strategy for AuNPs synthesis might enable the elimination of harmful interactions with biomolecules, consequently improving the holistic appearance of an SPR biosensor. Surprisingly, AuNPs-PAH-PSS-PAH assembly including cationic PAH presents an excess of immobilization positions for anti-Tau monoclonal antibodies. Because of the abundance of amino binding sites, a precise direction in the immobilization of affinity receptors serves to improve the overall efficiency of the SPR biosensor. The adoption of GO as a 2D carbon spine has assorted advantages, notably large surface area, biocompatibility, and the greatest number of binding sites for the deposition of constructed AuNPs-PAH-PSS-PAH facilitated AuNPs-PAH-PSS-PAH@Anti-Tau conjugates. The hydrogen-bonding, π - π stacking interactions, electrostatic interaction, and specifically hydrophilic affinity of GO strengthened biomolecule sorption possibilities. The projected GO@LbL-AuNPs-Anti-Tau SPR biosensor's sensitivity assessment delivers a broad concentration range from 5 fg/mL to 150 ng/mL and an exceedingly low detection limit of up to 13.25

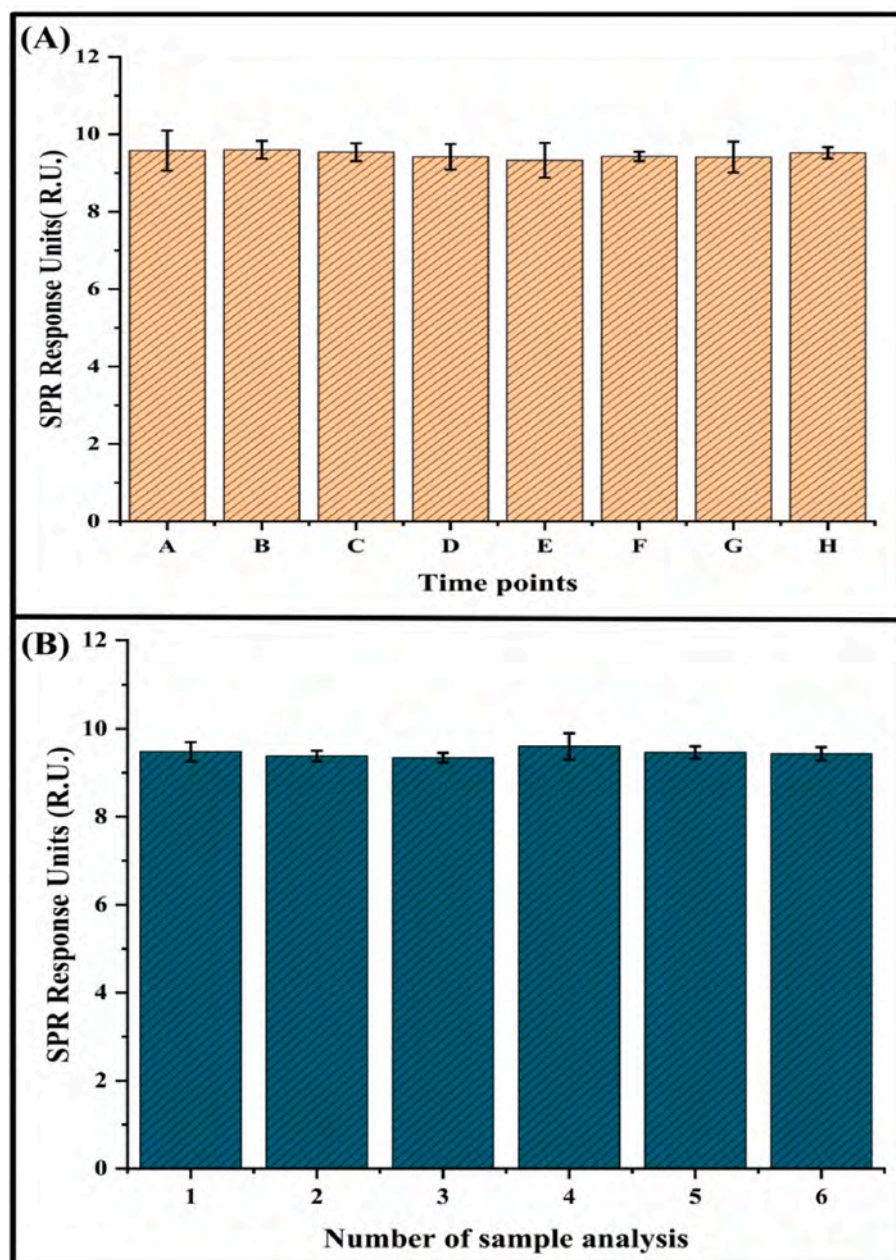


Fig. 7. (A) Stability of the GO@LbL-AuNPs-Anti-Tau SPR biosensor for Tau-441 antigen at different time points such as 1,4,8,12,18,24,36, and 48 h. (B) Reproducibility of the GO@LbL-AuNPs-Anti-Tau SPR biosensor for Tau-441 antigen (Number of sample analysis: 6).

Table 3

Spiked sample analysis of Tau-441 antigen in collected blood and saliva samples using GO@LbL-AuNPs-Anti-Tau SPR biosensor.

Sr. No.	Real-time sample	Spiked concentration	Measured concentration	% Recovery	% RSD
1.	Saliva	50 fg/mL	47.7 ± 0.44	95.4%	1.50%
2.	Blood	50 fg/mL	48.8 ± 0.89	97.6%	1.47%

N = 3, SD: Standard deviation (±).

fg/mL for the Tau-441 antigen. As well, the anti-interference performance and practical applicability of GO@LbL-AuNPs-Anti-Tau SPR biosensor were demonstrated by the selectivity and real-time analysis. Furthermore, the coupling of plasmonic AuNPs-PAH-PSS-PAH@Anti-Tau bioconjugates and GO nanocomposites culminated in complementary improvements for sensitivity and selectivity of GO@LbL-AuNPs-

Anti-Tau SPR biosensor than formerly published SPR biosensors. Finally, the constructed AuNPs-PAH-PSS-PAH@Anti-Tau bioconjugates LbL assembly facilitated GO nanocomposite has numerous advantages such as quick sensing, streamlined method, sustainable strategy, high sensibility, high specificity, reproducibility, and so on. As a result, in the coming days, the hypothesized GO@LbL-AuNPs-Anti-Tau SPR biosensor would bring up a revolutionary viewpoint for *in-vitro* diagnosis of AD as well as other severe health ailments.

Declaration of competing interest

The authors declare that they have no known competing financial interests or personal relationships that could have appeared to influence the work reported in this paper.

Data availability

Data will be made available on request.

Acknowledgment

The authors gratefully acknowledge research funding from the Indian Council of Medical Research (No.5/4-5/159/Neuro/2015-NCD-I). The authors would wish to acknowledge the H. R. Patel Institute of Pharmaceutical Education and Research, Shirpur, the Sophisticated Test & Instrumentation Centre Cochin University of Science and Technology Cochin, Kerala, and the Indian Institute of Technology (IIT)–Roorkee, India for supplying essential facilities. The authors would like to express their gratitude to the Institutional Animal Ethical Committee (Ref. No: IAEC/RCPIPER/2016-17/37) for granting permission to perform the animal study for the aforementioned research works.

Appendix A. Supplementary data

Supplementary data to this article can be found online at <https://doi.org/10.1016/j.aca.2023.341474>.

References

- [1] V. Pons, S. Rivest, Targeting systemic innate immune cells as a therapeutic avenue for Alzheimer disease, *Pharmacol. Rev.* 74 (2022) 1–17.
- [2] S. Nangare, P. Patil, Nanoarchitected bioconjugates and bioreceptors mediated surface plasmon resonance biosensor for *in vitro* diagnosis of Alzheimer's disease: development and future prospects, *Crit. Rev. Anal. Chem.* 52 (2022) 1139–1169.
- [3] J. Wiley, Alzheimer's disease facts and figures, *Alzheimers Dement* 17 (2021) 327–406.
- [4] G. Jungbauer, A. Stähli, X. Zhu, L. Auber Alberi, A. Sculean, S. Eick, Periodontal microorganisms and Alzheimer disease—A causative relationship? *Periodontol* 89 (2022) 59–82.
- [5] S.N. Nangare, P. Patil, Prevalence, distribution, treatment, and modern methods for *in vitro* diagnosis of Alzheimer's disease in India: challenges and future perspectives, *Thai J. Pharm. Sci.* 46 (2022) 149–160.
- [6] T.M. Ghazal, S. Abbas, S. Munir, M. Khan, M. Ahmad, G.F. Issa, S.B. Zahra, M. A. Khan, M.K. Hasan, Alzheimer disease detection empowered with transfer learning, *Comput. Mater. Continuum (CMC)* 70 (2022) 5005–5019.
- [7] K. Abbaya, N.Y. Puthanakar, S. Naduwinmani, Y. Chidambar, Association between periodontitis and Alzheimer's disease, *N. Am. J. Med. Sci.* 7 (2015) 241–246.
- [8] M.d. Vestergaard, K. Kerman, D.-K. Kim, H.M. Hiep, E. Tamiya, Detection of Alzheimer's tau protein using localised surface plasmon resonance-based immunochip, *Talanta* 74 (2008) 1038–1042.
- [9] X. Chi, D. Huang, Z. Zhao, Z. Zhou, Z. Yin, J. Gao, Nanoprobes for *in vitro* diagnostics of cancer and infectious diseases, *Biomaterials* 33 (2012) 189–206.
- [10] S.N. Nangare, P.O. Patil, Affinity-based nanoarchitected biotransducer for sensitivity enhancement of surface plasmon resonance sensors for *in vitro* diagnosis: a review, *ACS Biomater. Sci. Eng.* 7 (2021) 2–30.
- [11] S.N. Nangare, P.M. Sangale, A.G. Patil, S.H. Boddu, P.K. Deshmukh, N.R. Jadhav, R.S. Tade, D.R. Patil, A. Pandey, S. Mutalik, Surface architected metal organic frameworks-based biosensor for ultrasensitive detection of uric acid: recent advancement and future perspectives, *Microchem. J.* 169 (2021), 106567.
- [12] J. Zamanian, Z. Khoshbin, K. Abnous, S.M. Taghdisi, H. Hosseinzadeh, N. M. Danesh, Current progress in aptamer-based sensing tools for ultra-low level monitoring of Alzheimer's disease biomarkers, *Biosens. Bioelectron.* 197 (2022), 113789.
- [13] J.O. Esteves-Villanueva, H. Trzeciakiewicz, S. Martic, A protein-based electrochemical biosensor for detection of tau protein, a neurodegenerative disease biomarker, *Analyst* 139 (2014) 2823–2831.
- [14] C. Chen, W. Liu, S. Tian, T. Hong, Novel surface-enhanced Raman spectroscopy techniques for DNA, protein and drug detection, *Sensors* 19 (2019) 1712.
- [15] S. Kim, A.W. Wark, H.J. Lee, Femtomolar detection of tau proteins in undiluted plasma using surface plasmon resonance, *Anal. Chem.* 88 (2016) 7793–7799.
- [16] M. Ameri, Z. Shabaninejad, A. Movahedpour, A. Sahebkar, S. Mohammadi, S. Hosseindoust, M.S. Ebrahimi, A. Savardashtaki, M. Karimipour, H. Mirzaei, Biosensors for detection of Tau protein as an Alzheimer's disease marker, *Int. J. Biol. Macromol.* 162 (2020) 1100–1108.
- [17] P.O. Patil, G.R. Pandey, A.G. Patil, V.B. Borse, P.K. Deshmukh, D.R. Patil, R. S. Tade, S.N. Nangare, Z.G. Khan, A.M. Patil, Graphene-based nanocomposites for sensitivity enhancement of surface plasmon resonance sensor for biological and chemical sensing: a review, *Biosens. Bioelectron.* 139 (2019), 111324.
- [18] S. Zeng, K.-T. Yong, I. Roy, X.-Q. Dinh, X. Yu, F. Luan, A review on functionalized gold nanoparticles for biosensing applications, *Plasmonics* 6 (2011) 491–506.
- [19] M.M. Barsan, C.M. Brett, Recent advances in layer-by-layer strategies for biosensors incorporating metal nanoparticles, *TrAC, Trends Anal. Chem.* 79 (2016) 286–296.
- [20] B. Snopok, Y.G. Goltsov, E. Kostyukovich, L. Matkovskaja, Y.M. Shirshov, E. Venger, Self-assembled multilayer superstructures as immobilization support for bioreceptors, *Sensor. Actuator. B Chem.* 95 (2003) 336–343.
- [21] B. Masereel, M. Dinguizli, C. Bouzin, N. Moniotte, O. Feron, B. Gallez, T. Vander Borgh, C. Michiels, S. Lucas, Antibody immobilization on gold nanoparticles coated layer-by-layer with polyelectrolytes, *J. Nanoparticle Res.* 13 (2011) 1573–1580.
- [22] B. Masereel, M. Dinguizli, C. Bouzin, N. Moniotte, O. Feron, B. Gallez, T. Vander Borgh, C. Michiels, S. Lucas, Antibody immobilization on gold nanoparticles coated layer-by-layer with polyelectrolytes, *J. Nanoparticle Res.* 13 (2011) 1573–1580.
- [23] L.H. Chen, X.M. Ang, C.C. Chan, M. Shailender, B. Neu, W.C. Wong, P. Zu, K. C. Leong, Layer-by-layer (chitosan/polystyrene sulfonate) membrane-based Fabry–Perot interferometric fiber optic biosensor, *IEEE J. Sel. Top. Quant. Electron.* 18 (2012) 1457–1464.
- [24] Z. Zhao, Q. Li, J. Gong, Z. Li, J. Zhang, A poly (allylamine hydrochloride)/poly (styrene sulfonate) microcapsule-coated cotton fabric for stimulus-responsive textiles, *RSC Adv.* 10 (2020) 17731–17738.
- [25] N.-F. Chiu, T.-L. Lin, C.-T. Kuo, Highly sensitive carboxyl-graphene oxide-based surface plasmon resonance immunosensor for the detection of lung cancer for cytokeratin 19 biomarker in human plasma, *Sensor. Actuator. B Chem.* 265 (2018) 264–272.
- [26] N.-F. Chiu, M.-J. Tai, H.-P. Wu, T.-L. Lin, C.-Y. Chen, Development of a bioaffinity SPR immunosensor based on functionalized graphene oxide for the detection of pregnancy-associated plasma protein A2 in human plasma, *Int. J. Nanomed.* 14 (2019) 6735.
- [27] S. Nangare, S. Landge, A. Patil, R. Tade, P. Deshmukh, P. Patil, Green synthesis of Fe-doped Ag-loaded reduced graphene oxide ternary nanocomposite for efficient photocatalytic degradation of toxic dyes, *Adv. Nat. Sci. Nanosci. Nanotechnol.* 12 (2021), 035004.
- [28] M.K. Rabchinskii, V.V. Shnitov, A.T. Dideikin, A.E. Aleksenskii, S.P. Vul', M. V. Baidakova, I.I. Pronin, D.A. Kirilenko, P.N. Brunkov, J. Weise, Nanoscale perforation of graphene oxide during photoreduction process in the argon atmosphere, *J. Phys. Chem. C* 120 (2016) 28261–28269.
- [29] S. Karimi, H. Namazi, Fe₃O₄@ PEG-coated dendrimer modified graphene oxide nanocomposite as a pH-sensitive drug carrier for targeted delivery of doxorubicin, *J. Alloys Compd.* 879 (2021), 160426.
- [30] S. Nangare, P. Patil, Chitosan mediated layer-by-layer assembly based graphene oxide decorated surface plasmon resonance biosensor for highly sensitive detection of β -amyloid, *Int. J. Biol. Macromol.* 214 (2022) 568–582.
- [31] N. Sharma, M. Arif, S. Monga, M. Shkir, Y.K. Mishra, A. Singh, Investigation of bandgap alteration in graphene oxide with different reduction routes, *Appl. Surf. Sci.* 513 (2020), 145396.
- [32] P.O. Patil, S.N. Nangare, P.P. Patil, A.G. Patil, D.R. Patil, R.S. Tade, A.M. Patil, P. K. Deshmukh, S.B. Bari, Fabrication of N-doped graphene@ TiO₂ nanocomposites for its adsorption and absorbing performance with facile recycling, *Nano Biomed. Eng.* 13 (2021) 179–190.
- [33] E. Nagaraj, P. Shanmugam, K. Karuppannan, T. Chinnasamy, S. Venugopal, The biosynthesis of a graphene oxide-based zinc oxide nanocomposite using *Dalbergia latifolia* leaf extract and its biological applications, *New J. Chem.* 44 (2020) 2166–2179.
- [34] H. Qiu, X. Wu, R. Hong, G. Wu, S. Chen, Microfluidic-oriented synthesis of graphene oxide nanosheets toward high energy density supercapacitors, *Energy Fuels* 34 (2020) 11519–11526.
- [35] A.G. Patil, Facile one pot microbe-mediated *in situ* synthesis and antibacterial activity of reduced graphene oxide-silver nanocomposite, *Nanotechnology* 33 (2022), 135603.
- [36] R. Siburian, C. Simanjuntak, M. Supeno, S. Lumbanraja, H. Sihotang, New route to synthesize of graphene nano sheets, *Orient. J. Chem.* 34 (2018) 182–187.
- [37] S. Muralikrishna, K. Sureshkumar, T.S. Varley, D.H. Nagaraju, T. Ramakrishnappa, *In situ* reduction and functionalization of graphene oxide with L-cysteine for simultaneous electrochemical determination of cadmium (II), lead (II), copper (II), and mercury (II) ions, *Anal. Methods* 6 (2014) 8698–8705.
- [38] F.T. Johra, J.-W. Lee, W.-G. Jung, Facile and safe graphene preparation on solution based platform, *J. Ind. Eng. Chem.* 20 (2014) 2883–2887.
- [39] M. Singh, R. Kalaivani, S. Manikandan, N. Sangeetha, A. Kumaraguru, Facile green synthesis of variable metallic gold nanoparticle using *Padina gymnospora*, a brown marine macroalgae, *Appl. Nanosci.* 3 (2013) 145–151.
- [40] S. Smitha, D. Philip, K. Gopchandran, Green synthesis of gold nanoparticles using *Cinnamomum zeylanicum* leaf broth, *Spectrochim. Acta: Mol. Biomol. Spectrosc.* 74 (2009) 735–739.
- [41] D. Philip, Green synthesis of gold and silver nanoparticles using *Hibiscus rosa sinensis*, *Phys. E: Low-Dimens. Syst. Nanostructures.* 42 (2010) 1417–1424.
- [42] S. Vijayakumar, R. Vinayagam, M.A.V. Anand, K. Venkatachalam, K. Saravanakumar, M.-H. Wang, K. Gothandam, E. David, Green synthesis of gold nanoparticle using *Eclipta alba* and its antidiabetic activities through regulation of Bcl-2 expression in pancreatic cell line, *J. Drug Deliv. Sci. Technol.* 58 (2020), 101786.
- [43] K. Xin Lee, K. Shameli, M. Miyake, N. Kuwano, N.B. Bt Ahmad Khairudin, S.E. Bt Mohamad, Y.P. Yew, Green synthesis of gold nanoparticles using aqueous extract of *Garcinia mangostana* fruit peels, *J. Nanomater.* 2016 (2016) 1–7.
- [44] S. Satpathy, A. Patra, B. Ahirwar, M.D. Hussain, Process optimization for green synthesis of gold nanoparticles mediated by extract of *Hygrophila spinosa* T. Anders and their biological applications, *Phys. E: Low-Dimens. Syst. Nanostructures.* 121 (2020), 113830.

- [45] M. Guo, W. Li, F. Yang, H. Liu, Controllable biosynthesis of gold nanoparticles from a *Eucommia ulmoides* bark aqueous extract, *Spectrochim. Acta: Mol. Biomol. Spectrosc.* 142 (2015) 73–79.
- [46] G. Suriyakala, S. Sathiyaraj, R. Babujanarthanam, K.M. Alarjani, D.S. Hussein, R. A. Rasheed, K. Kanimozhi, Green synthesis of gold nanoparticles using *Jatropha integerrima* Jacq. flower extract and their antibacterial activity, *J. King Saud Univ. Sci.* 34 (2022), 101830.
- [47] M. Noruzi, D. Zare, K. Khoshnevisan, D. Davoodi, Rapid green synthesis of gold nanoparticles using *Rosa hybrida* petal extract at room temperature, *Spectrochim. Acta: Mol. Biomol. Spectrosc.* 79 (2011) 1461–1465.
- [48] Q. Ding, Z. Kang, X. He, M. Wang, M. Lin, H. Lin, D.-P. Yang, Eggshell membrane-templated gold nanoparticles as a flexible SERS substrate for detection of thiabendazole, *Mikrochim. Acta* 186 (2019) 1–9.
- [49] A.-N.D. Egueh, B. Lakard, P. Fievet, S. Lakard, C. Buron, Charge properties of membranes modified by multilayer polyelectrolyte adsorption, *J. Colloid Interface Sci.* 344 (2010) 221–227.
- [50] N.-F. Chiu, C.-T. Kuo, T.-L. Lin, C.-C. Chang, C.-Y. Chen, Ultra-high sensitivity of the non-immunological affinity of graphene oxide-peptide-based surface plasmon resonance biosensors to detect human chorionic gonadotropin, *Biosens. Bioelectron.* 94 (2017) 351–357.
- [51] H. Kim, J.U. Lee, S. Song, S. Kim, S.J. Sim, A shape-code nanoplasmonic biosensor for multiplex detection of Alzheimer's disease biomarkers, *Biosens. Bioelectron.* 101 (2018) 96–102.
- [52] S. Lisi, S. Scarano, S. Fedeli, E. Pascale, S. Cicchi, C. Ravelet, E. Peyrin, M. Minunni, Toward sensitive immuno-based detection of tau protein by surface plasmon resonance coupled to carbon nanostructures as signal amplifiers, *Biosens. Bioelectron.* 93 (2017) 289–292.
- [53] T.T.V. Nu, N.H.T. Tran, E. Nam, T.T. Nguyen, W.J. Yoon, S. Cho, J. Kim, K.-A. Chang, H. Ju, Blood-based immunoassay of tau proteins for early diagnosis of Alzheimer's disease using surface plasmon resonance fiber sensors, *RSC Adv.* 8 (2018) 7855–7862.